Flares on active M-type stars observed with *XMM-Newton* and *Chandra*

Urmila Mitra Kraev

Mullard Space Science Laboratory
Department of Space and Climate Physics
University College London

A thesis submitted to the University of London
for the degree of Doctor of Philosophy

ProQuest LLC
789 East Eisenhower Parkway
P.O. Box 1346
Ann Arbor, MI 48106-1346

I, Urmila Mitra Kraev, confirm that the work presented in this thesis is my own. Where information has been derived from other sources, I confirm that this has been indicated in the thesis.

Abstract

M-type red dwarfs are among the most active stars. Their light curves display random variability of rapid increase and gradual decrease in emission. It is believed that these large energy events, or flares, are the manifestation of the permanently reforming magnetic field of the stellar atmosphere. Stellar coronal flares are observed in the radio, optical, ultraviolet and X-rays. With the new generation of X-ray telescopes, *XMM-Newton* and *Chandra* , it has become possible to study these flares in much greater detail than ever before. This thesis focuses on three core issues about flares: (i) how their X-ray emission is correlated with the ultraviolet, (ii) using an oscillation to determine the loop length and the magnetic field strength of a particular flare, and (iii) investigating the change of density sensitive lines during flares using high-resolution X-ray spectra.

(i) It is known that flare emission in different wavebands often correlate in time. However, here is the first time where data is presented which shows a correlation between emission from two different wavebands (soft X-rays and ultraviolet) over various sized flares and from five stars, which supports that the flare process is governed by common physical parameters scaling over a large range.

(ii) As it is impossible to spatially resolve any but a very few giant stars, the only information on spatial dimensions as well as the magnetic field strength of stellar coronae has to come from indirect measurements. Using wavelet analysis, I isolated the first stellar X-ray flare oscillation. Interpreting it as a standing coronal flare loop oscillation, I derived a flare loop length as well as the magnetic field strength for this X-ray flare.

(iii) The high-resolution soft X-ray spectra of *Chandra* and *XMM-Newton* allow us to determine temperatures, densities and abundances of the stellar coronae. Despite a low signal-to-noise ratio because of the relatively short duration of a flare, we find that, if adding up the photons of several flares, certain density sensitive spectral lines change significantly between quiescent and flaring states. This project led on to investigate the flaring spectrum further, and it is found that the plasma is no longer in collisional ionisation equilibrium, but that it is dominated by recombinations.

Acknowledgments

First and foremost, I would like to thank my supervisor Louise Harra for her enduring support and guiding me on my way to become an independent researcher. My grateful thanks also go to my co-supervisors Graziella Branduardi-Raymont and Keith Mason for giving me the opportunity to work with *XMM-Newton* data and for their valuable contributions, in particularly regarding instrumentation and data analysis. My thanks also go to all my collaborators and colleagues at MSSL: Hilary Kay, for sharing her knowledge on stars and the Sun in general and *XMM-Newton* data analysis in particular; David Williams, for passing on his knowledge on coronal waves and IDL programming; Lidia van Driel-Gesztelyi, for her everlasting enthusiasm for solar and stellar physics; Alex Blustin, for introducing me to *XMM-Newton* data analysis and spectral fitting with SPEX, and many other contemporary colleagues at MSSL for answering questions, and discussing solar- and astrophysics. I am also gratefully indebted to my collaborators from other institutions, namely: Manuel Güdel, for introducing me to and passing on his excitement for stellar coronal physics, fruitful collaboration and discussions; Marc Audard and Ton Raassen for much valued contributions; Jan-Uwe Ness, for introducing me to *Chandra* data analysis and enthusiastic discussions about flare spectra; and last but not least my husband Egor Kraev, for his patience, constant support, and sharing his mathematical insight, in particular about wavelet analysis and error statistics. Special thanks also go to my examiners Valery Nakariakov and Mihalis Mathioudakis. And finally I would like to thank everyone who supported me patiently on my journey.

Contents

List of Tables

List of Figures

Chapter 1

Introduction

1.1 M dwarfs

1.1.1 General properties

Solar-like stars, that is cool stars with spectral type F, G, K, and M along the main-sequence of the Hertzsprung-Russell (HR) diagram, show various degrees of activity, flares being among the most energetic. Stellar flares radiate in all wavelengths, from radio to γ-rays, typically lasting from tens of minutes up to several hours, and releasing energies of up to 10^{34} erg (Pettersen, 1989). They are understood to be manifestations of the dynamic magnetic fields dominating the stellar atmospheres.

A list defining the various stellar classes referred to in this work is given in Table 1.1. The dMe stars which are analysed in this thesis all fall into the following categories: active dwarfs (more loosely, I sometimes also refer to them as active stars), flare stars, red dwarfs, solar-like stars, late-type stars, and cool stars.

The detection by Grotrian and Edlén of a million degree hot corona surrounding the Sun was made more than 60 years ago measuring optical lines of highly ionised elements. First solar X-ray photons were recorded during a rocket flight around 10 years later in 1949 by Burnight, while the *Skylab* mission in the early 1970s was crucial for our understanding of the X-ray corona of the Sun. The first stellar coronal

Table 1.1: Terminology

Cool stars	:	all stars cooler than type A, i.e., F, G, K and M
Hot stars	:	O and B stars
Late-type stars	:	stars which are or were type F, G, K or M during their main-sequence phase
Early-type stars	:	stars which are or were type O or B during their main-sequence phase
Solar-type stars	:	stars close to G2 during their main-sequence phase (like the Sun); can also be young (pre-main sequence) or evolved
Solar-like stars	:	stars with an outer convection zone, which are F, G, K or M, on or close to the main-sequence phase
Dwarf	:	here: solar-like star
Red dwarf	:	M star on or close to the main sequence
Active dwarf	:	dMe (or dKe) stars which show lot of coronal activity and flare frequently
Active star	:	here: active dwarf
Flare star	:	active dwarf

observation was made of Capella during a rocket flight (Catura et al., 1975), and soon after the first stellar X-ray flares were recorded with *ANS* on YZ CMi and UV Cet (Heise et al., 1975).

Late-type stars all have convective envelopes, which support dynamic magnetic fields. These fields rise from the interior to the outside, trapping ionised particles and sustaining the stellar atmosphere. While in the dense stellar interior the gas pressure is larger than the magnetic pressure, the opposite is true for the stellar atmosphere. There the dilute ionised plasma particles are tied to the magnetic field lines and can only move along them.

While the average solar corona is around 1–2 MK, compared with the solar surface temperature of around 6000 K, the average temperature of coronae from active stars can be several times higher, i.e., 7–8 MK, which is closer to the average temperature of the solar corona above an active region. As many of these stars are of type M, with surface temperatures of around 3500 K, the temperature gradient from their surface to the corona is steeper than on the Sun.

The thermal emission of the hot coronae is best studied in the soft X-ray (1–50 Å) and extreme ultraviolet (EUV) regime (50–1000 Å), as many atomic transitions at hot temperatures ($>$ 1 MK) fall into this range. However, X-ray and EUV observations need to be made in space because these regimes are not transparent to the Earth's atmosphere. Classical activity indicators therefore are hot lines in the optical (4000–7000 Å) and near UV range (2000–4000 Å) visible from the ground, like the hydrogen Balmer series Hα (λ6563Å), Hβ (λ4861Å), Hγ (λ4340Å) etc., as well as Ca II H (λ3968Å) and K (λ3934Å) and Mg II h (λ2802Å) and k (λ2795Å), which are typically formed in the chromosphere and occur during flares.

Red dwarfs (main-sequence M stars) are the most common stars and make up around 78% of the stellar population (Ledrew, 2001). They lie at the cool end of the HR diagram. With a $B - V$ colour index between 1.35 and 2.1 and effective temperatures below 3500 MK, the peak of their black-body emission lies in the infrared. Because of their low optical luminosity, optical flares can easily be observed

above the stellar black-body background. They can temporarily increase the stellar luminosity by several magnitudes. Comparatively, detecting optical flares on the Sun, which is a G2 main-sequence star with $T_{\rm eff} = 5770\,{\rm K}$ and therefore has its peak black-body emission in the optical, is much more difficult because of the lower contrast.

Of all the stars, flares are most frequently observed on a certain class of M-type stars. These active stars are also known as 'flare stars' or dMe stars, i.e., **d**warf, **M**-type, with the Hα-line (λ6563Å) in **e**mission. During solar flares, the Hα-line is in emission, while for the quiet Sun this line is absorbed. For flare stars, Hα is always in emission, which is explained by their permanent flaring activity. Sometimes, these stars are also referred to as UV Ceti-type stars in honour of their prototype UV Ceti.

M and K stars can be divided into two categories, the ones with the Hα line in emission (dMe/dKe), and the ones with the Hα line in absorption (dM/dK). The emission-line stars are much more active, which is seen in their higher X-ray emission (Mathioudakis & Doyle, 1989; Mullan & Fleming, 1996) and frequent flaring activity. However, non-emission-line stars also show flaring activity, albeit to a much lesser extent. Mullan & Fleming (1996) conclude that the active stars are covered to a much greater extent in active regions (above 50% of the surface), while the active region coverage of the relatively inactive stars must be below 10%. The inactive stars resemble much more the F and G stars, where Hα is also in absorption and their spot coverage is only a few percent of the stellar surface (0.01–1% for the Sun, which is a particularly inactive star).

1.1.2 Magnetic activity

Stellar X-ray emission is connected to the convective envelope. Flares are observed across the HR diagram, but they are concentrated along the main-sequence of late-type stars. Flaring is proportional to the volume of the stellar convection zone $V_{\rm CZ}$

(Pettersen, 1980). V_{CZ} increases from the more massive early F to the less massive mid/late M stars until the star is fully convective at $M \approx 0.3 M_{\odot}$, which is the case for M5V and later stars, or $L_{bol} < 3 \cdot 10^{31}\,\mathrm{erg\,s^{-1}}$. For even lighter objects, the overall activity then starts to decline, although occasional flares are also observed for very late M stars and brown dwarfs (e.g., Stelzer et al., 2006).

The stellar activity is dependent on the spectral type: (i) Later stars are more active because they have a larger convection zone. (ii) Fast rotators are more active. (iii) Younger stars are more active, a possible simple explanation is because they are rotating faster. Ultimately, the magnetic field is responsible for activity.

Stellar magnetic activity is dependent on age, chemical composition, mass and rotation rate of the star. Cool stars with convective envelopes all show soft X-ray emission. Between stars, the X-ray emission varies from 10^{26} to 10^{31} erg s^{-1}, but is not dependent on the stellar type. Lowest levels of X-ray emission from a star can be as low as the X-ray emission from a solar coronal hole, while highest levels are around the level of solar active regions, suggesting the star is entirely covered in active regions (during solar maximum, up to 1% of the solar surface gets covered by active regions). However, the maximum emission a star can produce is dependent on the volume of the convection zone (Pettersen, 1989).

An activity indicator frequently used is the ratio between X-ray and bolometric luminosity, L_X/L_{bol}. While L_{bol} decreases from the earlier, more massive F-type to the later, less massive M-type stars, L_X/L_{bol} increases, which is related to the relative size of the stellar convection zone. While A-type stars have no convection zone at all and show no X-ray emission, late M-type stars are fully convective. Stellar interior models show that not only relative, but also absolute values of the convective envelope volume increases for later-type stars, until a star is fully convective, which is the case for M5V or later stars with masses smaller than $\sim 0.3\ M_{\odot}$ and radii below $\sim 0.4\ R_{\odot}$.

Another correlation is L_X versus rotation rate P_{rot}, the faster a star rotates, the more active it is, until the correlation reaches saturation for very fast rotators. An

indirect measure of magnetic activity is the ratio of X-ray to bolometric (i.e. total) luminosity L_X/L_{bol}. For high magnetic activity, the X-ray luminosity is relatively large. Compared to other stars, the Sun shows only moderate magnetic activity, with $L_X/L_{bol} \approx 10^{-7}$ around solar minimum and increasing to $\approx 10^{-6}$ during solar maximum, while active M stars are with $L_X/L_{bol} \approx 10^{-3}$ at saturation limit.

There is a close correlation between the L_X/L_{bol} ratio (or ultra-violet activity indicators, Mathioudakis et al., 1995) and the Rossby number. The Rossby number is given by $\mathrm{Ro} = P_{rot}/\tau_c$, where τ_c is the convective overturn time. τ_c is an increasing function of $B-V$, with $B-V$ increasing for later-type main-sequence stars (Noyes et al., 1984). The stellar rotation slows down with stellar age. Thus, young, late-type stars with a small rotation period and a large convective overturn time have a small Rossby number and show high magnetic activity, while older and younger stars have a lower magnetic activity.

With age, the stellar activity is declining due to a slow-down of the rotation rate. Observations show that young stars with disks slow down much more than stars without surrounding disks because angular momentum is transferred from the star onto the disk.

Stars below a stellar mass of around $0.35\,M_\odot$ are believed to be fully convective (Chabrier & Baraffe, 1997) and can therefore not support a solar-type $\alpha\Omega$-dynamo, which operates at the tachocline between the convection and the radiation zone (Parker, 1975).

The $\alpha\Omega$-dynamo, which relies on differential rotation and shear forces at the tachocline, which is missing in fully-convective, late M stars, cannot be responsible for the strong magnetic activity of these stars. Instead, the idea of a dynamo which acts in the convection zone only has been brought forward, which could be either a locally acting turbulent dynamo (Drake et al., 1996) or a large-scale α^2-dynamo (Chabrier & Küker, 2006). Apart from the non-existent tachocline, four observational facts support a convective dynamo: (i) the absence of differential rotation, (ii) the absence of magnetic activity cycles similar to the 11-yr solar cycle, (iii) the

increase of activity with the volume of the convection zone, and (iv) the fact that a fully covered solar surface with active regions would not reach the X-ray saturation limit of $L_X/L_{bol} = 10^{-3}$ which is observed for many flare stars; for the Sun, the ratio would only be around 10^{-4} (Vilhu, 1984; Güdel, 2004). The last finding suggests that a convective dynamo is more efficient than the $\alpha\Omega$-dynamo. The rotational dependence of X-ray activity in fully-convective stars suggests further that the stellar rotation rate determines the activity level of the convective dynamo. For stars with a tachocline, both dynamos may be at work, the dominant contribution depending on whether there is fast rotation (convection dominated) or large differential rotation ($\alpha\Omega$ dominated). Both these dynamos produce variable magnetic fields, which lead to reconnection and flaring.

Are there qualitative differences between flares caused by either dynamo, or are they purely quantitative? The 'convective dynamo' flares are certainly more frequent and often more energetic. But what about the flare geometry and radiation processes? Are we allowed to apply the solar analogy to deduce stellar flare properties?

1.1.3 Features of the dMe stars treated in this work

Table 1.2 lists the seven dMe stars studied in this thesis and some of their properties. The spectral type is from the SIMBAD database, which omits the 'e' for some of the stars. Many other sources, however, list these targets as Hα emitters, and all of them are flaring frequently. All stars are in the solar neighbourhood within 10 pc (or just around for AT Mic). At 1.3 pc, Proxima Cen is the closest star to the Sun and a distant companion of α Cen A and B. It is also the X-ray faintest in our sample. UV Cet (GJ 65B) forms a visual binary with BL Cet (GJ 65A), with a separation of 5.06 AU or 2" on the sky, which is unresolved by *XMM-Newton* , but resolved with *Chandra* (Audard et al., 2003). Both components, however, are of similar spectral type. AT Mic is another unresolved binary system with *XMM-Newton* but with

Table 1.2: Targets and their properties

Name	UV Cet	YZ CMi	AD Leo	Prox Cen	AT Mic	AU Mic	EV Lac
GJ	65 B	285	388	551	799 AB	803	873
Sp. Type[a]	M5.5e[b]	M4.5Ve	M3.5V	M5.5Ve	M4.5[c]	M1Ve	M3.5e
Parallax[d] [mas]	381±6	169±3	213±4	772±2	98±5	101±1	198±2
Distance [pc]	2.62 ±0.04	5.9 ±0.1	4.69 ±0.09	1.295 ±0.003	10.2 ±0.5	9.9[e] ±0.1	5.05 ±0.05
$B-V$[a]	1.85	1.61	1.54	1.97	1.58	1.44	1.36
V[a]	12.52	11.12	9.43	11.05	10.25	8.61	10.09
M_V[f]	15.4	12.3	11.1	15.5	11.0[g]	8.63	11.6
$L_{\rm bol} \cdot 10^{30}$ [erg s^{-1}][h]	5.59	47	91.6	6.56	99[g,i]	240	53.5
$T_{\rm eff}$ [K][h]	2950	3150	3450	3050	3380	3515	3300
$R_\star/R_\odot$[h]	.14±.01	.37±.06	.43±.06	.14±.01[j]	.47[i]	.67	.36±.04
$M/M_\odot$[k]	.11±.02	0.26	0.37	0.11	0.38	0.68	0.32
$\log(\frac{L_{\rm X}}{L_{\rm bol}})$[l]	-3.30	-2.94	-3.14	-3.65	-2.85	-3.05	-3.05
$P_{\rm rot}$ [days][m]	27±7	2.78	2.7	42.0	2.04[n]	4.87	4.38
Ro[o]	0.892	0.099	0.099	1.335	0.072	0.184	0.169

[a]From the SIMBAD database

[b]GJ 65 A (BL Cet), with a separation of about 2" (5.06 AU), which is unresolved with *XMM-Newton* but resolved with *Chandra* (Audard et al., 2003), is of the same spectral type as GJ 65 B.

[c]Both components, separated by 2".8 (≈ 29 AU, Masciadri et al., 2005) and unresolved in X-rays, are of the same spectral type.

[d]From HIPPARCOS (Perryman et al., 1997), except for UV Cet (Harrington & Dahn, 1980) and AD Leo (Jenkins, 1952)

[e]Separated from AT Mic by 40 000 AU, or 1.3° on the sky (Gliese & Jahreiss, 1988)

[f]Using $M_V = V + 5\,(\log(\text{Parallax}) + 1)$

[g]Scaled to one component

[h]From Pettersen (1980), except for AT Mic and AU Mic (Lim et al., 1987). $R_\star$ was derived using $L_{\rm bol} = 4\pi R_\star^2 \sigma T_{\rm eff}^4$, where σ is the Stefan-Boltzmann constant and $R_\odot = 6.96\,10^{10}$cm.

[i]Corrected for the newer HIPPARCOS distance (Perryman et al., 1997)

[j]Direct interferometric measurement (Ségransan et al., 2003) yields the same radius.

[k]Calculated from the empirical mass-luminosity relationship for M dwarfs given by Delfosse et al. (2000) using M_V, except for the direct measurement of UV Cet (Lacy, 1977)

[l]With *EXOSAT* X-ray luminosities from Pallavicini et al. (1990)

[m]From Mathioudakis et al. (1995) and references therein, except for the predicted value of UV Cet (Doyle, 1987) and AT Mic (see note *n*)

[n]Using $P_{\rm rot} = 2\pi R_\star (v\sin i)^{-1}$ with $v\sin i = 11.7\,{\rm km\,s^{-1}}$ (Fuhrmeister et al., 2004)

[o]Ro $= P_{\rm rot}/\tau_c$, with the convective turnover time τ_c calculated using $B-V$ (Noyes et al., 1984)

Table 1.2: Targets and their properties – continued

Name	UV Cet	YZ CMi	AD Leo	Prox Cen	AT Mic	AU Mic	EV Lac
$\log(g)^p$ [cm s^{-2}]	5.2[q]	4.7	4.7[q]	5.2[r]	4.7	4.6	4.8
$v \sin i^s$ [km s^{-1}]	0.26	6.8	8.1	0.17	11.7	7.0	4.2
Chapter	3	3	5	5	3, 4	3, 5	3, 5, 6

[p]Using $g = \frac{M_\star}{M_\odot}\left(\frac{R_\star}{R_\odot}\right)^{-2} g_\odot$
[q]Values in agreement with Leggett et al. (1996)
[r]Value in agreement with Ségransan et al. (2003)
[s]Using $v \sin i = \frac{2\pi R_\star}{P_{rot}}$

Table 1.3: Solar parameters

Sp. Type	$B-V$	M_V	$T_{\rm eff}$	$R_\odot$	$M_\odot$
G2V	0.656[a]	4.8	5770 K	$7\,10^{10}$ cm	$2\,10^{33}$ g
$\log(g_\odot$ [cm s^{-2}])	$L_{\rm bol}$	$L_X/L_{\rm bol}$	$v_{\rm eq}$	$P_{\rm rot}$	Ro
4.44	$3.9\,10^{33}$ erg s^{-1}	0.25–$2.5\,10^{-6}$[b]	2 km s^{-1}	25.38 days	2.06[c]

[a]Gray (1992)
[b]Haisch et al. (1990)
[c]Noyes et al. (1984)

both components of the same spectral type. Thus, a flare observed on UV Cet or AT Mic could originate from either of the two components, but flare comparisons with spectral type are still meaningful because of the same spectral type. Both systems are also separated well enough not to share a common magnetic envelope, thus not belonging to the RS CVn variables, where magnetic loops could connect one star with the other and result in huge flares. AU Mic forms a distant proper motion pair with AT Mic, with a separation of 40'000 AU or 1.5deg on the sky, while AD Leo has a very low mass binary companion with a separation of 0.366 AU. The other two stars in the sample, YZ CMi and EV Lac, are single stars.

The stars in the sample are all young objects having just reached or approaching the main sequence, thus placing their age at or younger than 1 Gyr. AT Mic

and AU Mic are possibly the youngest of the sample, both belonging to the β Pic moving group, of which isochrone studies estimate an age of 20±10 Myr (Barrado y Navascués et al., 1999). However, recent findings (talk by E. Jensen at CS14) show that AT Mic is totally Li-depleted and stellar models suggest that it should therefore be at least 40 Myr old.

A disk was detected between 50 and 210 AU around the earliest star in our sample, AU Mic (Kalas et al., 2004). So far, no disks were detected around any of the other stars, which might be because of (i) sensitivity limits, as disks around later stars would be less massive and therefore less luminous, (ii) dusty disks are expected to have completely disappeared by 100 Myr, and only AU Mic is young enough to still have a disk, or (iii) disks are more difficult to form around binary stars (e.g., young AT Mic).

Stellar winds are also observed. For solar-like stars, the mass-loss rate is proportional to the stellar X-ray luminosity, but also to the age of the star (Wood et al., 2002). Younger stars have stronger winds. The mass-loss rate of AT Mic is 450 $\dot{M}_\odot$, the one of AU Mic is 720 $\dot{M}_\odot$, where $\dot{M}_\odot = 3 \cdot 10^{-14}\,M_\odot\,\mathrm{yr}^{-1}$ (Chen et al., 2005). Proxima Cen has a mass-loss rate of less than 0.2 $\dot{M}_\odot$, and EV Lac around 1 $\dot{M}_\odot$, which is uncharacteristically low for active M dwarfs (Wood et al., 2005).

Star spots have been observed on many of these stars, traditionally inferred by periodic light curve variations, which also yield the rotational period. E.g., Pettersen et al. (1983) do this exercise for EV Lac and YZ CMi. Alekseev (2005) finds spots on EV Lac on low latitudes (6–16°), and that they show an anti-solar drift from equator polewards, along with an anti-solar differential rotation (slow at equator, faster closer to the poles), with a cyclic period of 7.5 yr. On EV Lac, very strong (4 kG) magnetic fields have also been measured (Johns-Krull & Valenti, 1996). Recently, Cincunegui et al. (2007) found indications of a stellar activity cycle of 442 days in Proxima Cen.

1.2 Flares

1.2.1 Stellar flare observations

The first stellar flare observations were made in the late 1930s and 1940s in visible light on UV Cet, YZ CMi, AD Leo, WX UMa, Proxima Cen, and DO Cep (see list in Lippincott, 1952), all of which are active M stars. While the magnitude of WX UMa was found to change between observations (van Maanen, 1940), variations in the optical spectrum were observed on UV Ceti (Joy & Humason, 1949) and Proxima Centauri (Thackeray, 1950). The first stellar flare light curve was observed in the optical by Gordon & Kron (1949) on AD Leo.

Flares on M stars have also been observed in radio, optical and UV, and soft and hard X-rays. dMe-type stars, active M-type dwarfs, are among the most active stellar objects. Their frequent flaring allows us to observe flares during almost any observation, which is fortunate, as available satellite observation time is generally limited. However, sometimes it can get difficult to catch a quiescent time interval in order to compare the flaring state to the quiet one.

1.2.2 The standard flare model: Magnetic reconnection and chromospheric evaporation

The "standard" picture of a solar flare is that it is caused by reconnection of the magnetic field, which unleashes non-thermal electron and proton beams at the reconnection site. These beams travel along the magnetic field lines (while emitting gyro-synchrotron radio emission) and impinge on the chromosphere (or even photosphere), where they produce bremsstrahlung seen in hard X-rays (from electrons) and γ-rays (from protons) while heating the material at the foot points of the flare loop. The ionised chromospheric material then evaporates along the magnetic field lines of the (post-) flare loop upwards into the corona.

Ultra-violet (UV) as well as broad-band white-light (WL) radiation is produced

somewhere along this process, as a flare is often also seen in these wavelengths. It is not yet clear how exactly this radiation is produced, but it must be related to the impulsive phase of the flare, as it shows a steep rise concurrent to the hard X-ray light curve. On the Sun, it is difficult to observe WL radiation, as the WL flare emission is much weaker than the photospheric black-body radiation peaking in the same wavelength range. On the other hand, WL flares (WLF) are often seen on dMe stars, their background radiation being much weaker, with a black-body peak in the infrared. Therefore, it is easier to observe and study WL or near-UV flares on M-type stars than on the Sun.

Figure 1.1 visualizes chromospheric evaporation. Magnetic loops form a dense network over most of the Sun's surface into the corona, emerging from the inter-granular spots on the photosphere. The charged particles in the corona are confined to these field lines which define a loop, as seen e.g. in *TRACE* images. If two closed field lines/loops are in such a configuration that rearranging themselves would yield a lower potential energy, they reconnect. During the extremely fast reconnection process, particles are accelerated from the reconnection site and travel downward along the loop (Fig. 1.1). The fast, non-thermal electrons gyrate along the field lines, emitting gyro-synchrotron radio emission. They also collide with the surrounding plasma and emit bremsstrahlung in hard X-rays (> 20 keV); this happens mainly in the chromosphere, where the plasma is denser than in the corona. In this process, the plasma ions get excited and/or higher ionised. The chromospheric plasma in the magnetic loop is now hotter than the one above it, thus it expands and rises along the loop into the lower corona. This process is called chromospheric evaporation. Subsequently, the rising ions in the heated plasma cool down again and emit mostly in soft X-rays and extreme ultraviolet radiation (EUV) from atomic recombination.

If this chromospheric evaporation process is efficient enough it could account for most of the coronal heating; though, rather than heated, the hot coronal material is constantly replaced. Although the frequency of flare occurrence for large flares on the Sun is not high enough to explain a substantial amount of coronal heating,

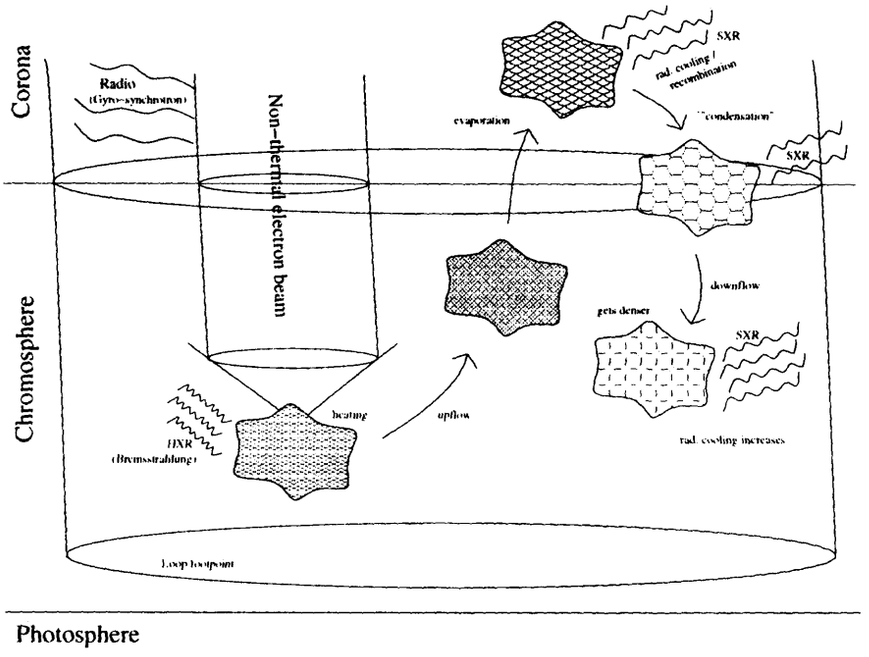

Figure 1.1: Chromospheric evaporation. From the corona, a non-thermal electron beam is accelerated along a magnetic loop down toward the photosphere. The relativistic electrons gyrate along the magnetic field lines and emit gyro-synchrotron radiation in the radio frequency. When they reach the chromosphere, they collide with the dense plasma, exciting the ions and emitting hard X-ray bremsstrahlung. Thus, the plasma gets heated and flows up into the corona. Eventually, the plasma cools again and emits soft X-rays (SXR) from recombination processes. Subsequently, the material sort of condenses, falls downward, gets denser still and thus radiates even more SXR.

there is evidence that the number of small flares increase rapidly with decreasing energy (Krucker & Benz, 1998; Parnell & Jupp, 2000), so that they could account for the bulk of coronal heating (Mitra-Kraev & Benz, 2001). Similar evidence but for larger flares is also seen on stars (Audard et al., 1999; Güdel et al., 2003).

The "Neupert Effect" (Neupert, 1968) describes how the thermal soft X-ray (SXR) emission is proportional to the integrated non-thermal hard X-ray (HXR) emission (and also to the non-thermal radio emission):

$$L_{\mathrm{SXR}}(t) \propto \int_0^t L_{\mathrm{HXR}}(t')\ dt',$$

where L_{SXR} and L_{HXR} are the$L_{\mathrm{SXR}}(t) \propto \int_0^t L_{\mathrm{HXR}}(t')\ dt'$,nosities, respectively, and t the time coordinate. This means that the non-thermal process is directly responsible for the plasma heating.

How does white-light flare emission fit into this picture? During the rise phase of a flare, white light very closely follows steep rise of the the non-thermal emission. Studying WLF on the Sun is not easy because of the large background optical/near UV light from the solar photosphere. But WLF on M stars are easily observed because their white-light emission is low, as their black-body radiation peaks in the infrared. It is therefore desirable to study the relationship between white light and other wavelengths during flares on active M stars. Understanding stellar white-light emission in the overall flare context is of particular importance, as WL is believed to be closely related to non-thermal emission, which is otherwise also seen in hard X-rays or the radio regime. The latter two wavelength ranges are fairly well understood on the Sun, but not often observed on stars; hard X-rays because there are not yet many observations available, while radio observations also depend on the flare geometry and not every soft X-ray flare is accompanied by a radio flare (Smith et al., 2005). However, optical flares are frequently observed.

1.2.3 Flare dimensions

Solar flares can end up in single loop structures (1-loop flare), in arcades of flares (2-ribbon flare), or even more entangled magnetic features with many loops above an active region. X-ray observations of the Sun over a broad range in the soft X-ray band observed with *Yohkoh* revealed large, thick, fuzzy post-flare loops, where the diametrical cross-section can be around one tenth of the loop length. These cylindrical loops are filled with denser and hotter material than the surroundings. The *GOES* satellites, which mainly monitor the solar full-disk X-ray emission, observe in about the same wavelength regime. This X-ray range is also the regime where *XMM-Newton* and *Chandra* observe. Therefore, by analogy and assuming stellar structures are comparable to solar ones, the point-like stellar sources observed by *XMM-Newton* and *Chandra* may have underlying structures similar to the ones which were observed with *Yohkoh* on the Sun.

Solar observations with *TRACE* and *SOHO*, which observe in a narrower coronal temperature band around 1 MK, reveal even more and finer structures, and suggest the thick *Yohkoh* loops are made up from many thin, fine strands of magnetic field lines.

1.3 Magneto-hydrodynamic waves

As coronae are dominated and highly structured by the stellar magnetic fields, the magnetic field lines can act as wave guides for magneto-hydrodynamic (MHD) waves. The waves can be traveling or standing waves. They can be magnetic dominated (Alfvén waves), or pressure dominated, or a combination thereof. And a wave can be fast or slow. In the stellar interior, where the gas pressure is larger than the magnetic pressure, acoustic (pressure) waves travel fast and magnetic waves travel slow. In the stellar atmosphere, where the magnetic field dominates over the gas pressure, the opposite is true: magnetic waves travel fast and acoustic waves travel slow.

As the coronal plasma is highly ionised and dilute, the magnetic field dominates in the corona and the ionised particles must gyrate along the magnetic field lines. Using waves to probe into the structure of the corona has in the past decade matured into a discipline termed "coronal seismology".

A flare loop is an ideal platform for a standing wave, acoustic or magnetic, where the wave period is proportional to the loop length. Additionally, the wave propagation depends on the local magnetic field strength, as well as the plasma density and temperature. Thus, measuring coronal waves enables us to probe into otherwise unobservable coronal properties. In the solar case, where the loop is resolved, the unknowns are usually the magnetic field strength and electron density. For stars, however, where the electron density can be measured from spectroscopy but no spatial resolution is available, an oscillation can be used to find the flare loop length as well as the magnetic field strength.

1.4 X-ray spectroscopy

A wide range of spectral features fall into the soft X-ray regime (1–50Å), which is covered by the high-resolution instruments on-board *XMM-Newton* and *Chandra*. The K-shell transitions of carbon through iron and the L-shell transitions of silicon through iron fall in this region (Kahn et al., 2002). Furthermore, high-temperature astrophysical plasmas, including stellar coronae, emit at these wavelengths. The emission spectrum depends on physical properties of the plasma like element abundances, differential emission measure, temperature, density, opacity, but also on the type of ionisation equilibrium (IE) or non-ionisation equilibrium (NIE). Thus, the soft X-ray range is ideally suited to probe into plasma conditions.

1.4.1 Temperatures and densities from line ratios

Temperature and density diagnostics by spectroscopy is best done by comparing certain sensitive line ratios of the same element, thus avoiding uncertainties in relative element abundance. The simplest temperature determination is achieved by comparing the line ratio of adjacent ionisation states of the same element; for higher temperatures, the higher ionisation state will become more populated. Density determination, on the other hand, is often made by comparing certain density-sensitive line ratios of the same ion.

The He-like triplets of the resonance (r), intercombination (i) and forbidden (f) lines are well suited for both temperature and density diagnostics. The r, i, and f lines are given by the following K-shell transitions:

$$
\begin{aligned}
r &: \ 1s2p\,{}^1P_1 \rightarrow 1s^2\,{}^1S_0 \\
i &: \ 1s2p\,{}^3P_{2,1} \rightarrow 1s^2\,{}^1S_0 \\
f &: \ 1s2s\,{}^3S_1 \rightarrow 1s^2\,{}^1S_0
\end{aligned}
$$

While the $R = f/i$ ratio is sensitive to density, the $G = (f+i)/r$ ratio is sensitive to temperature (Gabriel & Jordan, 1969; Porquet et al., 2001). The temperature sensitivity arises because the collision strength of r increases with increasing temperature, while the ones of f and i drop, thus G decreases with increasing temperature.

The density dependence arises from the fact that the electrons from the $^3S_1$ state can be collisionally excited into the ^3P levels. At high densities this process dominates over the radiative decay of the forbidden line such that the i line becomes stronger at the expense of the f line. Thus, R decreases with increasing density. The presence of a strong UV radiation field can act in a similar way through photoexcitation, and so the density diagnostics capabilities of the R ratio can only be used if the UV radiation field is negligible, which is usually the case in a coronal plasma.

Figure 1.2 shows the calculated density dependence of the R ratio for various ions using the CHIANTI database (Dere et al., 1997; Landi et al., 2006). The

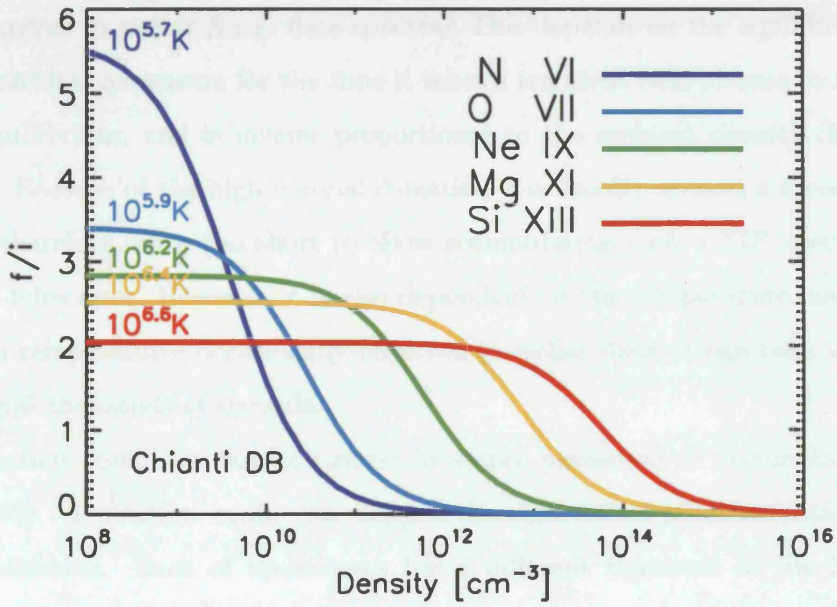

Figure 1.2: The f/i-ratio as a function of density for He-like ions at their respective maximum emission temperature, calculated with CHIANTI.

temperature sensitivity ranges from $10^{6.9}$ K for the hottest ions (Si) to $10^{5.7}$ K for the cooler ones (N). The cooler ions are density-sensitive at lower densities, while the hotter ions probe only higher densities.

1.4.2 Non-ionisation equilibria

Coronal plasma are usually in thermal ionisation equilibrium; in fact, the term "coronal" is often used as synonym for "thermal". However, flares are quintessentially non-equilibrium, transient phenomena. Can therefore non-ionisation equilibria (NIE) be observed in stellar X-ray flare spectra? This depends on the equilibration timescale τ which is a measure for the time it takes a transient NIE plasma to reach ionisation equilibrium, and is inverse proportional to the ambient density (Mewe et al., 1985). Because of the high coronal densities, τ is usually around a second or smaller and therefore much too short to allow accumulating such a NIE spectrum with current telescopes. However, τ is also dependent on the temperature, and for the very high temperatures occasionally observed in stellar flares it can take values of up to several thousands of seconds.

Non-ionisation equilibria can be caused by either ionisation or recombination (Liedahl, 1999). Ionisation again can happen through either photoionisation or collisional ionisation. Each of these cases has a different signature in the X-ray spectrum.

The G ratio of the He-like triplets is a good indicator about the type of plasma. For a collisional ionisation equilibrium plasma (CIE), G is between 0.7 and 1.5, while an ionizing plasma has $G < 0.7$, and a recombining plasma $G > 1.5$ (Pradhan, 1985). For recombinations, a large G ratio arises because electrons mainly recombine (directly and through cascades from higher orbits) into the $^3S_1$ state (from where they can also be excited into the ^3P states if the density is high enough), but to a much lesser degree into the resonant $^1P_1$ level. Ionizing, on the other hand, is more efficient into the $^1P_1$ level because of its larger coefficient rate. In all of the above

cases, the temperature dependency of the G ratio is still valid, but the dependency function is different for the various cases (Bautista & Kallman, 2000). Thus, in order to establish the temperature from the G ratio, the ionisation mechanism must be determined first.

1.5 Open questions

Can our knowledge from the Sun be extended to the case of low-mass stars? What are the physical conditions of M star flares, their structures, loop lengths and magnetic field strengths?

In particular, does the standard flare model with magnetic reconnection, particle acceleration and subsequent chromospheric evaporation hold for M star flares? If the answer is yes, then we may use the solar analogy to deduce stellar flare properties which are unobservable by direct means like spatial dimensions or (coronal) magnetic field strengths.

Active M stars are about 10 times more active than the Sun would be if it were covered entirely in active regions. This might be explained by a different dominant dynamo mechanism acting in these stars. A turbulent (or convective) dynamo which scales with the convective volume and the rotation rate might be more efficient in producing a magnetic field than the solar-like $\alpha\Omega$-dynamo. Are flares caused by such a "turbulent" magnetic field simply more frequent and often more energetic than solar flares but otherwise similar, or are there deeper differences? Does the flare-frequency distribution depend on the type of magnetic dynamo, and could in the turbulent case the coronal heating be fully explained by flares?

The turbulent dynamo and its effect can be studied in isolation on M stars, whereas on the Sun it is overshadowed by the $\alpha\Omega$-dynamo but may still play an important role. Does it? Could for instance a turbulent dynamo on the Sun be responsible for enough small flares to heat the quiet corona?

Apart from the Sun, which is the only place to observe spatially resolved stellar

flares, active M stars are particularly good objects to study flares for the following reasons: the flaring rate is very high, which in turn enhances the chances to observe high-energy flares, where physics in extreme conditions can be studied; and as the black-body emission of M stars peaks in the infrared, all important wavelength regimes to flaring, including optical and UV, have a low background (unlike for the Sun).

1.6 Overview

This thesis concentrates on a few aspects of the general stellar flare picture, in particular aspects of M star flares. The chromospheric evaporation scenario is supported by simultaneous UV and X-ray flare observations, which follow a power-law relationship and show that UV flares peak before the X-ray ones (Chapter 3), as well as by the large density increase observed during flares in the He-like O VII lines (Chapter 5). Under the chromospheric evaporation assumption, an observed flare oscillation is used to determine the flare loop length as well as the ambient coronal magnetic field strength (Chapter 4). And finally, in Chapter 6, a high-resolution flare spectrum is discussed in detail, where it is found that the plasma is no longer in thermal equilibrium, but transient and recombining, which can only be observed under extreme conditions with very high temperatures. It also shows upflows and a possible photoionisation signature in the cooler elements, which may be caused by a strong UV radiation field.

Chapter 2 gives a short introduction to the instruments on *XMM-Newton* and *Chandra* which were used for gathering the data analysed in this thesis, while Chapter 7 ends this work with overall conclusions and a short outlook.

Chapter 2

Instrumentation

Since their launch at the beginning of this millennium, the X-ray satellite observatories *Chandra* and *XMM-Newton* have revealed much information on the composition and physical conditions of stellar coronae (see review by Güdel, 2004), in particular because of their high-resolution X-ray spectral capabilities.

As one of ESA's "cornerstone" missions, *XMM-Newton* [1], launched on 10 December 1999, is the biggest ever scientific satellite built in Europe, while the *Chandra* X-ray Observatory[2], which was launched on 23 July 1999, takes its place among NASA's four "Great Observatories". Both observatories have imaging and spectral capabilities in the 0.1–10 keV energy range. They are both in high-altitude elliptical orbits around the Earth, reaching to around a third of the Moon's orbit, with orbital periods of 48 hrs for *XMM-Newton* and 64 hrs for *Chandra* , and can thus observe for up to 37 and 48 consecutive hours, respectively. Their extended mission lifetime is 10 years each.

[1] http://sci.esa.int/science-e/www/area/index.cfm?fareaid=23

[2] http://chandra.harvard.edu/about/

2.1 *XMM-Newton*

The X-ray Multi-Mirror (XMM) assembly, which honors Sir Isaak Newton in its name, consists of three barrel shaped X-ray telescopes, each consisting of 58 gold-coated, concentric nested mirrors with 0.3 to 0.7 m in diameter and 0.6 m in length. The total collecting area is 4300 cm^2 at 1.5 keV and 1800 cm^2 at 8 keV. The mirror grazing incidence angles range between 17 and 42 arcmin and have a focal length 7.5 m (Jansen et al., 2001).

There are three main scientific instruments on board *XMM-Newton* : (i) the European Photon Imaging Camera (EPIC), (ii) the Reflection Grating Spectrometer (RGS, den Herder et al., 2001), both recording X-rays, and (iii) the Optical/UV Monitor (OM, Mason et al., 2001), which is co-aligned with the X-ray instruments and gives the telescope its multi-wavelength capacity.

Behind two of the three X-ray mirrors is an RGS, RGS1 and RGS2 respectively, while EPIC detectors are at the end of the focal path of each of the three X-ray telescopes. The two EPIC detectors with an RGS in their optical path are equipped with mos-type CCDs (EPIC-mos, Turner et al., 2001), while the EPIC detector which receives the full photon flux operates on pn-CCDs (EPIC-pn, Strüder et al., 2001). All EPIC detectors have a circular field of view of 30', while the resolving power (FWHM) for extended sources is 5".

Table 2.1 lists some of the key instrument features of *XMM-Newton* and *Chandra* in the X-ray range. The X-ray photons are all recorded with their arrival time and position on the detector, which in the case of RGS corresponds to energy and in the case of EPIC to the physical image. EPIC also records the energy, but with a much smaller spectral resolution than RGS. While the EPIC instruments have very high sensitivity, imaging capabilities and a large bandpass, but only limited spectral resolving power, RGS is optimised for a high spectral resolution.

The instrument time resolution is far better than the integration time needed to obtain a stellar light curve with a good signal-to-noise ratio (SNR), which is

Table 2.1: Key instrument spectral X-ray features of *XMM-Newton* and *Chandra*

	XMM-Newton [a]			*Chandra* [b]		
	EPIC		RGS	HETGS[c]		LETGS[d]
	pn	mos		HEG	MEG	
Bandpass E [keV]	0.15–15	0.15–12	0.35–2.5	0.8–10	0.4–5	0.07–10
Bandpass λ [Å]	0.8–82	1–82	5–38	1.2–15	2.5–31	1.2–175
Spectral resolving power $E/\Delta E$ or $\lambda/\Delta\lambda$	20–50	20–50	200–800	65–1070	80–970	25–1000
Spectral resolution $\Delta\lambda$ (FWHM) [Å]	1.0[e]	0.9[e]	0.06[f]	0.012	0.023	0.05
Maximal effective area $A_{\rm eff}$ [cm^2]	1000	400	140	∼50	∼140	25
Time resolution	0.03 ms	1.5 ms	0.6 s	2.85 ms–3.24 s		10 ms

[a] From the *XMM-Newton* Users' Handbook, see
http://xmm.vilspa.esa.es/external/xmm_user_support/documentation/uhb/index.html

[b] From the *Chandra* Proposers' Observatory Guide, see
http://cxc.harvard.edu/proposer/POG/pog_pdf.html

[c] HETG with ACIS-S

[d] LETG with HRC-S

[e] At 1 keV

[f] den Herder et al. (2001)

usually chosen to be 100–200 s for a broadband EPIC-pn light curve. There is a trade-off between high spectral and good time resolution. For a nearby M star, an integration time of 30 ks yields a decent high-resolution X-ray spectrum. However, the SNR is often too low for studying spectral changes during a flare which only lasts for perhaps 5 ks. Good SNR over such short integration times can only be achieved for extremely bright flares with lot of emission. Unfortunately, such huge flares do not occur often and are therefore very rarely observed. Summing up spectra from many flares can somewhat overcome this limitation, although this only allows to study average flare properties.

The Optical Monitor (OM), which is co-aligned with the X-ray instruments and operates simultaneously, monitors the sky in the optical and UV. Its primary mirror has a diameter of 30 cm. The field of view is 17'×17' and the imaging resolution 0.5", 1", or 2" (depending on timing constraints). It has six broad-band filters in the range from 180 to 580 nm, and one for "white-light" which transmits light over the full range. Additionally, it contains two grisms to obtain spectra, one optimised for the UV, the other for the optical range. Finally, a magnifier can provide high spatial resolution in a 380–650 nm band. One of the 10 filters only can be chosen for each exposure. The observations analysed in this thesis (Chapter 3) were made with either the UVW1 (245–320 nm) or the UVW2 (180–225 nm) filter.

The OM can operate in either the 'IMAGE' or the 'TIMING' mode. The IMAGE mode is optimised for spatial resolution, while a single exposure takes between 800 and 5000 s. As an overhead of around 300 s has to be added in, the best cadence achieved in IMAGE mode is around 1100 s. In TIMING (or fast) mode a time resolution of up to 0.5 s can be achieved (with a maximal exposure length of 4400 s). For monitoring active, variable stars (point-sources!) the TIMING mode would generally be desirable. However, the observations presented here were all obtained during the early stages of the *XMM-Newton* mission, where technical problems were encountered with the TIMING mode. Therefore, although the targets were originally proposed to be observed in TIMING mode, this could not be done, and

the IMAGE mode was used instead. The problems have since been resolved.

2.2 *Chandra*

The *Chandra* X-ray observatory, named after the astrophysicist Subrahmanyan Chandrasekhar, has an assembly of four pairs of nested mirrors coated with iridium, with grazing angles ranging from 27 to 51 arcmin and a focal length of 10 m. The effective area at 1 keV is 800 cm^2, the mirror resolution 0.5".

Chandra is equipped with four X-ray instruments[3], two with imaging capabilities, the Advanced CCD Imaging Spectrometer (ACIS) and the High-Resolution Camera (HRC), and two high-resolution spectrometers, the High-Energy Transmission Grating Spectrometer (HETG) and the Low-Energy Transmission Grating Spectrometer (LETG). Unlike the instruments on *XMM-Newton* , the science instruments on *Chandra* do not observe simultaneously.

The ACIS can be for imaging (ACIS-I) or in conjunction with either of the two transmission grating spectrometers (ACIS-S), while HRC can be used for imaging (HRC-I) or as readout for LETG (HRC-S). The right side of Table 2.1 lists some of the key spectral features for the two different transmission grating spectrometer configurations of *Chandra* , HETGS and LETGS.

This work only uses *Chandra* data taken in the HETGS (HETG+ACIS-S) configuration, therefore I will concentrate on its description. The collected X rays first pass through the HETG spectrometer and are then recorded on the ACIS detector chips. The zeroth order photons form an X-ray image on the detector, while the first and higher order spectra are dispersed in a straight line away from the zeroth order image, the position depending on the energy of the recorded photon. Thus, each photon gets recorded with its individual energy and arrival time. The HETG consists of two gratings, the high-energy grating (HEG) and the medium-energy grating (MEG). Their grating arms are offset by an angle of 10° on the detector.

[3]http://cxc.harvard.edu/cdo/about_chandra/overview_cxo.html

Chapter 3

Flares in X-rays and ultraviolet

3.1 Summary

We present simultaneous ultraviolet and X-ray observations of the dMe-type flaring stars AT Mic, AU Mic, EV Lac, UV Cet and YZ CMi obtained with the *XMM-Newton* observatory. During 40 hours of simultaneous observation we identify 13 flares which occurred in both wave bands. For the first time, a correlation between X-ray and ultraviolet flux for stellar flares has been observed. We find power-law relationships between these two wavelength bands for the flare luminosity increase, as well as for flare energies, with power-law exponents between 1 and 2. We also observe a correlation between the ultraviolet flare energy and the X-ray luminosity increase, which is in agreement with the Neupert effect and demonstrates that chromospheric evaporation is taking place. This work was published in Mitra-Kraev et al. (2005a).

3.2 Introduction

XMM-Newton is an ideal platform for observing cosmic sources simultaneously in X-rays and ultraviolet (UV). In particular, flux and energy comparisons between these wavebands are important in understanding the flare mechanisms in stellar

coronae. Late-type stars typically show high coronal activity similar to the Sun, with flux variability through all observed wavelength bands. dMe-type stars are particularly active. They show frequent flaring activity (Pallavicini et al., 1990), as well as strong emission lines (including the Hα Balmer emission line, which is denoted by the 'e' in dMe). Soft X-rays (<12 keV) typically originate in the corona, while UV radiation comes from the chromosphere and transition region. Flares are observed in both wave bands, but what is the physical process that connects X-ray and UV flares?

In the chromospheric evaporation picture (see, e.g., Antonucci et al., 1984), flares are believed to be due to the energy release from the reconnection of magnetic field lines in the lower corona. Electrons are accelerated at the reconnection site. They gyrate downward along the magnetic field lines, emitting gyrosynchrotron radio emission. Their collision with denser material in the chromosphere unleashes bremsstrahlung seen in hard X-rays (>20 keV). Both the gyrosynchrotron radio and hard X-ray flare emissions are impulsive, with a fast increase and a steep decay. At the same time, the electrons impulsively heat the chromosphere, which results in prompt optical/UV emission which closely correlates with the hard X-ray emission (Hudson et al., 1992). During the collisions, the chromospheric ions get further ionised, the material heats up and evaporates, increasing the density and the temperature of the reconnected loops in the corona. The hot material is seen in soft X-ray and extreme ultraviolet emissions, where the light curves are more gradual, with a slower increase than the impulsive emission and a much longer, exponential decay. The impulsive and gradual emissions are often temporally connected through the "Neupert effect" relation (Neupert, 1968; Dennis & Zarro, 1993)

$$L_{\rm grad}(t) = q \cdot \int^{t} L_{\rm impuls}(t')\ dt', \qquad (3.1)$$

$$L_{\rm grad}(t) = q \cdot \int_{0}^{t} L_{\rm impuls}(t')\ dt',$$

indicating that the gradual radiative loss rate is directly proportional to the cumulative impulsive energy input, and suggesting that the energy input from the non-thermal electrons is responsible for the heating of the plasma.

The soft X-rays originating from the hot (>1 MK) coronae of late-type stars are dominated by emission lines (H- and He-like transitions of C, N, O, Ne, Mg, and Si, and Fe K- and L-shell transitions), indicating thermal processes. The UV emission from dMe stars is mainly line emission formed around 10^4 K (Linsky et al., 1982), though during flares continuum emission is also observed in the near-optical UV band (Hawley & Pettersen, 1991). At optical wavelengths, both impulsive continuum and gradual line emission are observed during flares (García-Alvarez et al., 2002). The Neupert effect has been known to exist between impulsive U-band and soft X-ray emission (Güdel et al., 2002; Hawley et al., 1995).

Previous investigations relating UV and soft X-rays in late-type stars were either focused on individual flares or statistical flux-flux relationships for the entire stellar emission with no temporal resolution. The UV data were collected with the International Ultraviolet Explorer (*IUE*), which obtained low dispersion spectra in the 1150–3200 Å band, and compared with data from the X-ray satellites *Einstein* (0.2–4 keV), *EXOSAT* (0.06–2 keV) and *ROSAT* (0.1–2.4 keV), and more recently UV data from the Hubble Space Telescope were compared with X-ray data from the *Chandra* satellite (Ayres et al., 2001). To distinguish flaring from non-flaring conditions, Mathioudakis & Doyle (1989) compared flux-flux relationships of inactive dM/dK to active dMe/dKe stars, using the latter as a proxy for flaring conditions. They find a power-law relationship with an exponent of $\approx$1 between chromospheric Mg II h & k (2795–2803 Å) *IUE* and coronal X-ray (*Einstein* and *EXOSAT*) flux, but only for the active stars. The inactive stars are scattered, with generally lower X-ray luminosity. Thus, the coronal X-ray emission is enhanced for stars with flares compared to stars without. Similar analyses for F–K type stars have been made by Schrijver et al. (1992, including a basal flux subtraction) and Ayres et al. (1995, fluxes scaled to bolometric fluxes), who found power-law exponents between 1.5 and 2.9. The basal flux is the part of the stellar emission not originating from magnetic activity, but caused by acoustic waves. In particular, it forms a component of the emission originating from the chromosphere, but not from the corona, as acoustic

waves are supposed to have dissipated by the time they would reach the corona. The remaining flux after the removal of the basal flux, which is dependent on stellar type or colour, is independent of stellar colour for late F to K stars.

None of the above papers tested the relationship of different fluxes for individual flares. We set out to probe directly the statistical flux-flux relationship between X-ray and UV emission for flares. dMe-type stars are the natural choice, as they flare frequently. The instruments on-board *XMM-Newton* provide an excellent opportunity for carrying out these observations.

This chapter is structured in the following way: Sect. 3.3 describes the observations and the instrumental setup. The results are presented in Sect. 3.4, starting with the X-ray and UV luminosity light curves of EV Lac, UV Cet, YZ CMi, AU Mic and AT Mic. The respective light curves are cross-correlated and flares identified in both wavebands. Then, the power-law relationships between luminosity increase per flare and flare energy are presented. We discuss the results in Sect. 3.5 and conclude with Sect. 3.6.

3.3 Observations

We present *XMM-Newton* data of dMe-type stars obtained during the Reflection Grating Spectrometer (RGS) Guaranteed Time Programme. We make use of the pn-European Photon Imaging Camera (EPIC-pn, Strüder et al., 2001), and the Optical Monitor (OM, Mason et al., 2001). The EPIC-pn covers the range 0.2–12 keV (1–62 Å). The OM observed with two different UV filters, one for each observation, namely the UVW1 (2450–3200 Å) and the UVW2 (1800–2250 Å) filter.

Table 3.1 gives a list of the targets, shows the spectral type, the distance to the star (from SIMBAD parallaxes), the observed UV range and UV filter. The index is for further reference in the later plots. While some of the X-ray results of these targets have already been published (Raassen et al., 2003; Ness et al., 2003; Magee et al., 2003), this is the first time that we make use of the simultaneously obtained

Table 3.1: Observational Parameters and Results

	EV Lac	UV Cet	YZ CMi	AU Mic	AT Mic
Index	A	B	C	D	E
Spectral Type	dM4.5e	dM5.5e+dM5.5e	dM4.5e	dM1e	dM4.5e+dM4.5e
UV Filter	UVW1	UVW1	UVW2	UVW2	UVW2
UV Range [Å]	2450–3200	2450–3200	1800–2250	1800–2250	1800–2250
$\bar{L}_{\rm uv}[10^{29}{\rm erg/s}]$	0.434	0.0258	1.28	12.3	6.39
$\bar{L}_{\rm x}[10^{29}{\rm erg/s}]$	0.545	0.0333	0.370	2.99	2.89
Time-lag UV−X-ray [s]	-600^{+600}_{-600}	-200^{+600}_{-200}	-600^{+600}_{-400}	-400^{+400}_{-400}	-1000^{+800}_{-1000}
X-ray/UV max. Correlation	0.68	0.90	0.78	0.68	0.84

UV data.

For all observations, OM observed in IMAGE mode, where a single exposure lasted 800 s and the dead-time between two exposures was 320 s, thus resulting in a time resolution of 1120 s. (Originally, the UV observations were meant to be taken in high-time resolution mode, but because of instrumental problems with the TIMING mode during the early stages of the mission, the IMAGE mode was used instead. These problems were resolved later on.) The data for the EPIC-pn light curves were binned into 200 s time intervals. All data were reduced with the *XMM-Newton* Science Analysis System (SAS) version 5.4.

3.4 Results

3.4.1 Light curves

3.4.1.1 Determining the luminosity

Figures 3.1 and 3.2 (left panels) display the X-ray and UV light curves of EV Lac, UV Cet, YZ CMi, AU Mic and AT Mic. In the ultraviolet, EV Lac and UV Cet (Fig. 3.1) were observed with the UVW1 filter, whereas YZ CMi, AU Mic and AT Mic (Fig. 3.2) were observed with the UVW2 filter.

The conversion from X-ray and UV count rates to luminosity has been made in the following way: The UV luminosity $L_{\rm uv}$ is given by

$$L_{\rm uv} = 4\pi d_\star^2 \cdot G \cdot \Delta_{\rm uv} \cdot c_{\rm uv}, \tag{3.2}$$

with $c_{\rm uv}$ the UV count rate and $d_\star$ the distance to the star (see Table 3.1). G is the factor to convert from count rate to flux, derived by folding stellar spectra with the in-flight response curves of the OM and tabulated on the *XMM-Newton* SAS homepage at Vilspa. The values of G for M-type stars are $7.32(\pm0.39) \cdot 10^{-16}\,\mathrm{erg\,cm^{-2}\,\AA^{-1}\,cts^{-1}}$ and $1.04(\pm0.21) \cdot 10^{-13}\,\mathrm{erg\,cm^{-2}\,\AA^{-1}\,cts^{-1}}$ for the UVW1 and the UVW2 filter, respectively. $\Delta_{\rm uv}$ is the bandwidth of the UV filter, 750 Å for

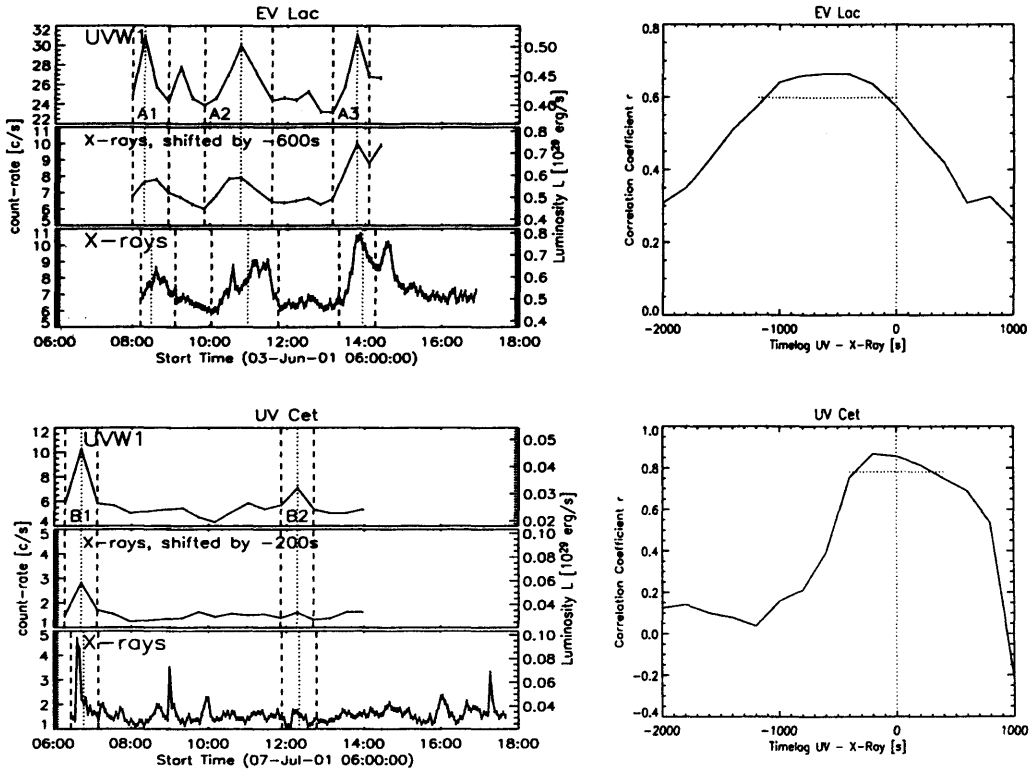

Figure 3.1: The light curves (left panels) and their cross-correlations (right panels) of EV Lac and UV Cet, where the UVW1 filter for the OM was used. The lowest panel in each left graph shows the 200s-binned X-ray data, the upmost panel the UV light curve, and the middle panel the X-ray light curve at maximum correlation (shifted by the time lag) and binned to UV resolution (800 s integration time and a cadence of 1120 s). The count rate is given on the left, the luminosity on the right ordinate. The dashed vertical lines indicate the start and the end of the flare, the dotted vertical lines the time of the flare peak in the UV. The right panels show the cross-correlation between the X-ray and UV light curve for each target (see main text). The horizontal dotted lines are at 90% level of each maximum and mark the peak error interval.

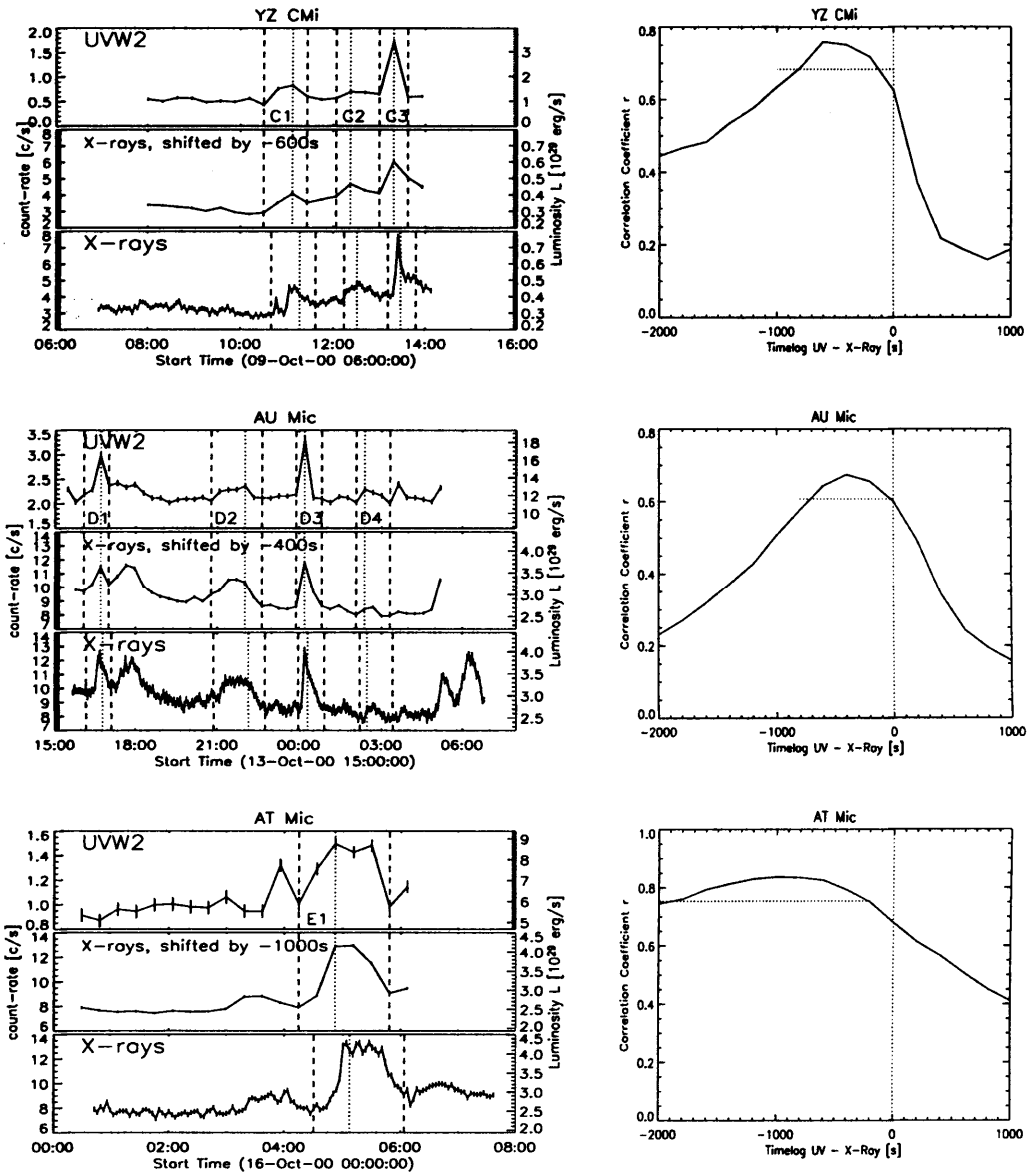

Figure 3.2: The light curves (left panels) and their cross-correlations (right panels) of YZ CMi, AU Mic and AT Mic, where the UVW2 filter for the OM was used. The same explanations as in Fig. 3.1 hold.

UVW1 and 450 Å for UVW2. The values of the average stellar UV luminosities over the whole observations, $\bar{L}_{uv}$, are displayed in Table 3.1.

For the X-ray luminosity, the average luminosity $\bar{L}_x$ has been obtained from fitting the EPIC-pn spectrum from the whole observation with a 3-Temperature CIE (collisional ionisation equilibrium) model within the SPEX package (Kaastra et al., 1996) with variable elemental abundances. The precise values of the abundances do not matter in this context, as the value for the average luminosity, which is directly given by the count rate in the spectrum, is stable. The value of $\bar{L}_x$ for each target, which includes dead-time corrections, is displayed in Table 3.1. The three temperatures are typically 2–3 MK, 7–8 MK and >20 MK. The X-ray luminosity L_x is then given by the average luminosity $\bar{L}_x$ divided by the average count rate $\bar{c}_x$ times the X-ray count rate c_x

$$L_x = \frac{\bar{L}_x}{\bar{c}_x} \cdot c_x. \tag{3.3}$$

One might argue that the different shapes of the quiescent and flaring X-ray spectrum have a non-linear effect on the scaling of the luminosity. The X-ray spectrum is dominated by lines in the range of 0.2–1 keV and has a decreasing exponential tail above 1 keV. During flares, the exponential tail falls off more slowly than during quiet times, indicating higher temperatures and energies, while the low-energy range rises uniformly. Our fits show that most of the energy comes from the low-energy range. The values for the total observations are 0.2–1 keV $\sim$ 70–75%, 1–2 keV $\sim$ 15–20%, and 2–12 keV $\sim$ 10%, while during flares the contribution to the lowest energy band is reduced by about 5%, and increased by about 5% for the highest energy band. This suggests that the approximation that the luminosity scales linearly with the count rate is a fair assumption.

3.4.1.2 Cross-correlation between the UV and X-ray flux

The two light curves from each of the five observations show a good correlation. For an increase in the UV, we generally also see an increase in the X-rays. Note

that the UV is broad-band emission and therefore the bulk of it being continuum (non-thermal) and not line emission (thermal).

According to the Neupert effect, the X-ray light curve should match the integrated UV light curve (or, equivalently, the derivative of the X-ray light curve matching the UV light curve). To include cooling, the UV light curve should in fact be convolved with a cutoff exponential decay profile instead of just integrated, with a decay time of 200 s giving a good fit for, e.g., Proxima Cen (Güdel et al., 2002). Unfortunately, the time resolution of the UV data (800 s integration time and 300 s time gap) is not good enough to test directly for the Neupert effect. Therefore, each pair of light curves has been cross-correlated in such a way that the 200s-binned X-ray light curve (lowest panels in the light curve plots of Figs. 3.1 and 3.2) was shifted by a multiple of 200 s, then binned to the UV resolution and correlated with the UV light curve (upmost panel). As the bin-size of the data compared is larger than the cooling decay time of $\sim$200 s and therefore the resolution is below the one required for observing the Neupert effect, no information would be gained by comparing the UV versus the derivative of the X-ray light curve instead of simply the two light curves. Therefore, the two light curves are cross-correlated directly in the above manner without using the derivative of the X-ray one.

The plots on the right hand side of Figs. 3.1 and 3.2 show the cross-correlation for each target. The abscissa displays the time-lag between the UV and X-ray light curves, the ordinate the corresponding correlation coefficient. For all observations, the function has a distinct peak with a maximum correlation coefficient between 0.68 and 0.90. For the error estimate in time, the width of the cross-correlation distribution function at the 90% level of the correlation coefficient maximum was calculated (horizontal dotted lines in the cross-correlation plot). This error corresponds to about the 1σ error of the Fisher z-test. In all but the UV Cet observation, which is dominated by short X-ray flares which are below the OM resolution, the entire peak within the error lies left of zero, indicating that flares tend to peak earlier in UV than in X-rays. The middle panels of the light curve plots show the X-ray

light curves at maximum correlation (shifted by the time-lag) and binned to UV resolution.

3.4.1.3 Flare identification

In both the UV and the X-ray (low 800s-resolution) light curves (upper two panels in Figs. 3.1 and 3.2) flares are identified. The flare criteria are: (i) It has to appear in both wave bands simultaneously. (ii) The difference between flare peak and start intensity exceeds 3σ of the noise (3×average noise). (iii) The difference between flare peak and end intensity exceeds 3σ in at least one of the light curves (and 1σ in the other). The beginnings and ends of the flares are marked with a dashed vertical line, the flare peak with a dotted vertical line. Each flare is named by a letter and a number displayed under the UV light curve.

3.4.2 The UV–X-ray relationship in flares

For each flare, the background-subtracted energy from flare start to end $E_f = \int_{f_{\rm start}}^{f_{\rm end}} \left(L(t) - L_f^{\rm min}\right) dt$ as well as the luminosity increase from flare start to flare peak have been obtained for both UV and X-rays (low 800s-resolution). Figure 3.3 shows the relationship between UV and X-rays for the observed flares from EV Lac and UV Cet (UVW1 filter, left side) and from YZ CMi, AU Mic and AT Mic (UVW2 filter, right side). The upper panels are for the luminosity, the lower panels for the energy relationship. We define the spectral luminosity density (luminosity per unit wavelength) $\mathcal{L} := L/\Delta$ and the spectral energy density $\mathcal{E} := E/\Delta$, with Δ being the width of the respective passband. The flare data are fitted with a power-law

$$\text{(X-ray)} = 10^c \cdot (\text{UV})^\kappa, \tag{3.4}$$

the values of c and κ are given in Table 3.2. The regressions have been made in the following way: For each regression, we have first applied two linear ordinary least-square (OLS) fits (Isobe et al., 1990) to the logarithmic data, one for Y dependent on X, taking the Y-error into account, the other for X dependent on Y, taking the

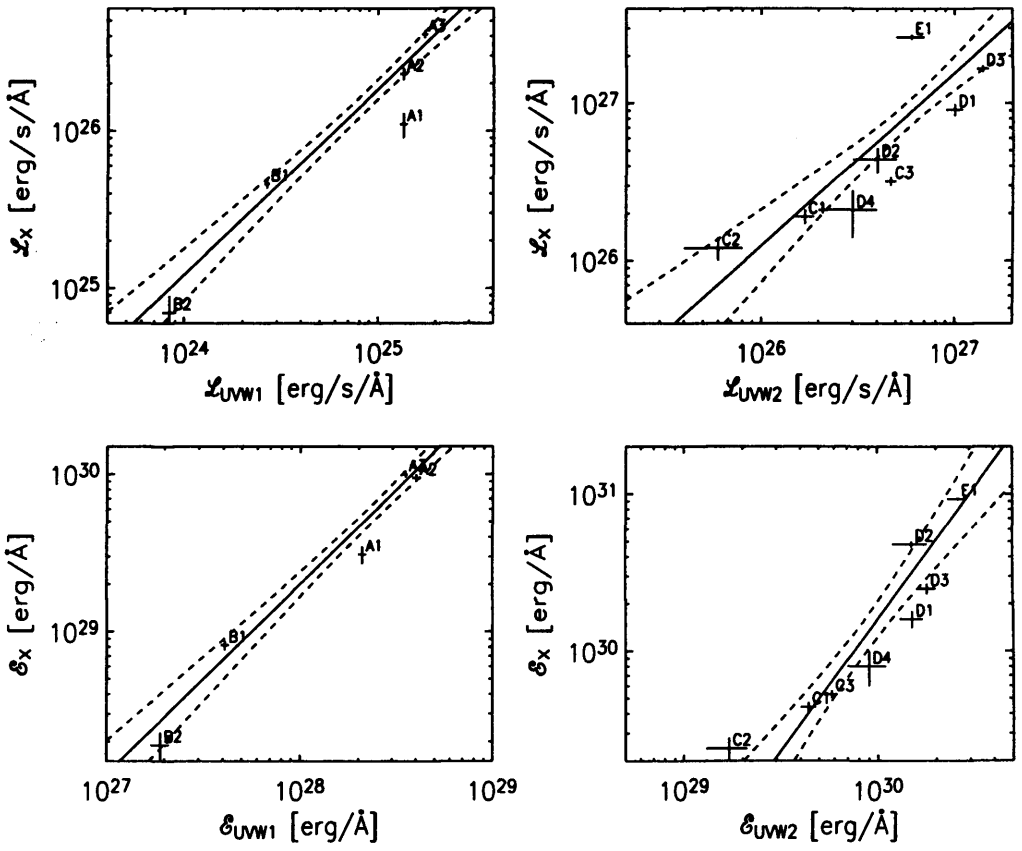

Figure 3.3: X-ray vs UV flare relationships. The two panels on the left use the UVW1, the ones on the right the UVW2 filter. The upper panels are for the luminosity increase, the lower panels for the flare energy. Used throughout for the regression are spectral luminosity density and spectral energy density, as defined in Sect. 3.4.2. The crosses denote the flares, their sizes corresponding to the 1σ error. They are labelled according to their identification as in Figs. 3.1 and 3.2. The solid line in the plot indicates the best fit power-law regression. The flares have been weighted with their individual errors for the regression. The dashed lines contour the 3σ error, where σ is the standard deviation of the mean. The regression values are given in Table 3.2.

Table 3.2: Relationship Parameters for log(X-ray) = $\kappa \cdot \log(\mathrm{UV}) + c$

		κ	c
$\mathcal{L}$	UVW1	1.17±0.05	−3.1±1.4
	UVW2	1.10±0.09	−2.5±2.5
$\mathcal{E}$	UVW1	1.21±0.05	−4.5±1.4
	UVW2	1.68±0.13	−20±4

X-error into account (linfit.pro in IDL). Given the two regressions (slopes β_1 and β_2), the bisector was calculated (slope $\beta_3 = \tan\frac{\mathrm{atan}\beta_1 + \mathrm{atan}\beta_2}{2}$) and the new variances obtained from Monte-Carlo simulations. The OLS bisector is thus chosen as the optimal regression.

For the luminosity (Eqs 3.2 and 3.3), we only considered the error from the counts, which basically follows Poisson statistics. Three further errors of the quantities used to derive the luminosities do not contribute much to the overall result. The uncertainty in stellar distance (< 5%) affects UV and X-ray luminosity alike and therefore does not influence the power-law slope. The G-factor of Eq. (3.2) carries an error of 5% for UVW1 and 20% for UVW2. As our targets all have similar spectral types, the possible systematic error is unlikely to affect the power-law exponent either. The third error is the (small) non-linear contribution from the determination of the X-ray luminosity, which has been neglected (see Sect. 3.4.1.1).

3.5 Discussion

Comparing the peak luminosity increase as well as the total energy of flares, we find that the UV and X-ray emissions are correlated and that the relationships follow power laws, with power-law indices between 1 and 2. For the UVW2 results, the different power-law indices for the luminosity and energy relationships indicate that different time scales are involved in the energy release of X-ray and UV emission.

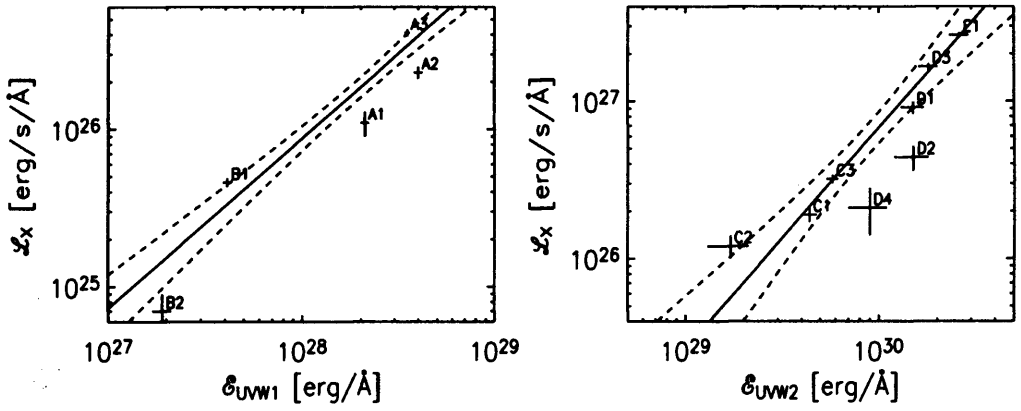

Figure 3.4: Relationship between X-ray luminosity increase and UV flare energy. The conventions are the same as in Fig. 3.3. The fit parameters are given in Table 3.3.

While the luminosity increase roughly scales with an index of unity, the energy, which is time-integrated luminosity, scales with a power-law index significantly larger than unity. This suggests that for larger flares the duration of the X-ray emission is relatively longer than the duration of the UV emission. We are careful not to draw quantitative conclusions for the UVW1 results because of the extremely small statistical sample.

The Neupert effect (Eq. 3.1) predicts a temporal correlation between UV energy and X-ray luminosity. Although our data do not have a high enough temporal resolution, we can still test for a consistency with the Neupert effect indirectly. If the Neupert effect holds, then the total UV flare energy should be roughly proportional to the X-ray peak luminosity increase. From the chromospheric evaporation scenario, we indeed expect that a larger influx of non-thermal energy results in a larger amount of hot plasma, i.e. in more X-ray emission. We test for such a correlation, which is plotted in Fig. 3.4, and the power-law fit parameters are given in Table 3.3. We find that there is such a correlation between the UV and the X-ray emission.

The existence of an X-ray-luminosity/UV-energy correlation is in agreement with

Table 3.3: Neupert Relationship Parameters: $\mathcal{L}_x = 10^c \cdot \mathcal{E}_{uv}^{\kappa}$

	κ	c
UVW1	1.08±0.05	−4.4±1.5
UVW2	1.40±0.11	−15±3

the Neupert-effect relationship and would suggest that the plasma is heated from the bottom of the magnetic flux tube to the top, first reaching the chromosphere and only a few hundred seconds later the hotter corona (from the time-delay in the flare emission between UV and X-rays), which is consistent with chromospheric evaporation. It does not, however, confirm the Neupert effect. For that, the time resolution would have to be much better. The power-law exponent is close to unity for the UVW1 flares and somewhat larger for the UVW2 flares. If this correlation were indeed due to the Neupert effect, a power-law exponent of 1 would indicate that the factor of proportionality q in Eq. (3.1) would be similar for all flares and thus imply similar physical conditions (e.g. the physics of energy transport and transformation) for all flares. A power-law exponent of a different value would suggest an energy dependence of q.

We would like to remark here that time resolution of the light curve also has an effect on the slope. While the flare energy is not strongly dependent on the bin size, the luminosity increases are. If the bin size is larger than the time scale of the flare, the underestimation of the luminosity increase can be severe. For X-rays, comparing the 200s-binned data with the 800s-binned data, we find that for small flares the luminosity increase is underestimated more than for large flares if the bins are large. For the UV flares, which are known to be more impulsive and have shorter time scales than the X-ray flares, the luminosity increase might be underestimated throughout. The luminosity-energy relationship is especially affected by this underestimation and the true correlation might be less steep and closer to unity.

It may also be that all these correlations are just a manifestation of the big flare syndrome (BFS), which states that statistically all energetic flare phenomena are more intense in larger flares, regardless of the detailed physics (Kahler, 1982). On the other hand, a correlation of two a priori unrelated parameters tells us something about the underlying physics. A correlation between extensive parameters (e.g. volume and mass) can be regarded as trivial, but a correlation between intensive parameters (e.g. energy and luminosity) is not trivial. Since in this paper we are studying correlations between intensive parameters, even if the correlations are due to the BFS, they tell us something about the underlying physics. We can test for the BFS, if we compare the correlation coefficient of flare parameters we expect to correlate based on flare models, like $L_x - L_{uv}$, $E_x - E_{uv}$ and the relationship following from a possible Neupert effect $L_x - E_{uv}$, to flare parameters which have no physical reason to correlate ($E_x - L_{uv}$). The correlation of the latter would reflect merely the BFS. The former being significantly higher than the latter would indicate an additional physical cause than just the BFS. Indeed, for the UVW2 filter, the relationship $E_x - L_{uv}$ gives a much lower correlation coefficient ($r = 0.63$) than the ones which are physically related ($r = 0.83$ for luminosity, $r = 0.92$ for energy and "Neupert"). Therefore, the UVW2 correlations are probably reflecting more than just the BFS. However, the correlation coefficients for the small UVW1 sample are all above 0.95, including the BFS control parameters $E_x - L_{uv}$, and cannot distinguish between trivial and non-trivial scalings.

The slopes of the average stellar luminosities are close to unity, in agreement with Mathioudakis & Doyle (1989). If the total stellar emission in X-rays and UV is a result of the superposition of many flares, then the X-ray to UV ratio of the average stellar luminosity should be similar to the X-ray to UV ratios of the flare energies. This is indeed so. For the flares, the ratio of X-ray to UV spectral energy density ranges from 10 to 29 (average of 19) for UVW1 and from 0.9 to 3.6 (average of 1.7) for UVW2. For the entire sample of stars, the ratio of X-ray to UV average spectral luminosity density is between 15 and 16 for the UVW1 filter and between

1.6 and 3.3 for the UVW2 filter. The quiescent spectral luminosities have the same ratios. The energy ratios among the flares have a relatively wide spread because the power-law exponent is greater than unity. The stellar luminosity ratios within each UV wave band vary much less and are very close to the average flare energy ratios. Previously, Haisch et al. (1990) also reported that the ratio between energy losses in coronal X-rays and chromospheric Mg II lines is similar in flares and in quiescence in the dMe star Proxima Cen. This indicates a similar energy release physics both in flares and in the low-level emission. A possible explanation is that the low-level emission is in fact produced by a large number of unresolved flares that heat chromospheric gas and build up a corona by chromospheric evaporation. This hypothesis has recently found strong support from statistical light curve analysis (Güdel et al., 2003; Arzner & Güdel, 2004).

The extremely good temporal correlation between UV and X-ray flares is noteworthy. For almost every increase in UV emission, we also observe a corresponding increase in X-rays, which is a similar result to the one found between the optical U-band and X-rays in a recent observation of Proxima Cen (Güdel et al., 2004). The overall good correlation between UV and X-ray flare occurrence is contrary to many previous observations, where some X-ray flares do not show a UV (or radio) counterpart and vice versa. This is especially true for older observations, which might be due to poorer instrumental performance. On the Sun, however, soft X-ray flares (usually less intense than the typical stellar flare observed here) only occasionally show simultaneous white-light emission, but all white-light flares also have a corresponding X-ray flare. Recent investigations by Matthews et al. (2003) show that white-light production is connected to peak pressure. It might be that in these more energetic stellar flare events such a critical peak pressure is almost always present, and therefore all flares are observed in both wavebands.

In the UVW2 observations, we notice that there are two types of flares. The impulsive ones with a linear increase, an exponential decrease and a sharp peak, and the flares with a flat top. The latter are rising somewhat slower than the

impulsive ones, showing prolonged, sustained peak emission. The tops of these flares (E1, D2, C2) are not constant, and in the case of E1 show periodic variations. We note that in the energy relationship plot these flat-top flares lie above the best-fit power-law correlation, which means that either there is a deficit in UV emission, or that there is an excess in X-rays. A similar phenomenon is seen in the correlation between microwave and hard X-ray emission in solar flares (Kosugi et al., 1988), where the long duration flares lie above the mean linear correlation, indicating a larger microwave to hard X-ray ratio for these flares.

3.6 Conclusions

We have investigated X-ray and UV light curves of several dMe stars, focusing on the temporal coincidence of flares and possible correlations between fluxes and radiative energies. The aim of this project was to study causal relations between mechanisms that produce UV and X-ray emission. The chromospheric evaporation scenario developed from solar observations and flare simulations predicts that the impulsive-phase optical/UV emission, most likely due to accelerated electrons impacting on the chromosphere, should precede the more slowly evolving soft X-ray emission that is emitted by the heated plasma. Specifically, the Neupert effect should approximately hold, i.e. the X-ray light curve is proportional to the time integral of the optical/UV light curve. Further, if the energy in the plasma stems from the accelerated electron population, we expect that the flare amplitudes are roughly correlated in amplitude or radiated energy.

We find evidence of both features predicted by the evaporation scenario. Firstly, most UV flares characteristically precede the X-ray peaks by typically ten minutes, which approximately coincides with the soft X-ray flare rise time. Secondly, we find a close near-linear correlation between the peak fluxes of the optical and the X-ray flares. The correlation becomes non-linear for the total radiative energies, implying that for larger flares the time scales of the X-ray flares become longer compared to

the UV flare time scales.

An interesting aspect is the comparison of the X-ray to UV energy loss rate ratio of flares with the corresponding ratio between average emissions. We find that the two are indeed similar, which suggests that the total emission is a superposition of individual flare emissions. Our observations thus support a picture in which stellar chromospheres and coronae are continuously heated by impulsive energy release processes.

Chapter 4

X-ray flare oscillation

4.1 Summary

We present the first X-ray observation of an oscillation during a stellar flare. The flare occurred on the active M-type dwarf AT Mic and was observed with *XMM-Newton*. The soft X-ray light curve (0.2–12 keV) is investigated with wavelet analysis. The flare's extended, flat peak shows clear evidence for a damped oscillation with a period of around 750 s, an exponential damping time of around 2000 s, and an initial, relative peak-to-peak amplitude of around 15%. We suggest that the oscillation is a standing magneto-acoustic wave tied to the flare loop, and find that the most likely interpretation is a longitudinal, slow-mode wave, with a resulting loop length of $(2.5 \pm 0.2)\, 10^{10}$ cm. The local magnetic field strength is found to be 105 ± 50 G. These values are consistent with (oscillation-independent) flare cooling time models and pressure balance scaling laws. Such a flare oscillation provides an excellent opportunity to obtain coronal properties like the size of a flare loop or the local magnetic field strength for the otherwise spatially-unresolved star. This work was published in (Mitra-Kraev et al., 2005b).

4.2 Introduction

Oscillations in the solar corona have by now been observed for many years. Wavelength regimes ranging from radio to hard X-rays have been investigated in the search for evidence of waves. Table 1 in Aschwanden et al. (1999) provides a summary and description of the different periods found (0.02 to 1000 s). Most of these waves have been explained by magneto-hydrodynamic (MHD) oscillations in coronal loops, see Roberts (2000) for a detailed review of waves and oscillations in the corona.

One of the most exciting aspects of "coronal seismology" is that it potentially provides us with the capability for determining the magnetic field strength in the corona (Roberts et al., 1984), as well as, in the stellar case, with information on otherwise unresolved spatial scales, e.g., flare loop lengths. It is notoriously difficult to measure the magnetic field strength in the corona because of the very high speeds of coronal electrons, which broaden spectral lines far beyond the width of Zeeman splitting. Techniques using both near-infrared emission lines and radio observations are successful, but have poor spatial resolution. Indirect methods are commonly used, such as the extrapolations of the coronal magnetic field from the photospheric magnetic field, which in turn can be measured using the Zeeman effect.

Many of the observations of waves have been determined from variations in intensity. However, a huge step forward was achieved in solar coronal physics due to the high spatial resolution available with the Transition Region and Coronal Explorer (*TRACE*, Handy et al., 1999). Aschwanden et al. (1999) observed the first spatial displacement oscillations of coronal loops. It was suggested that these oscillations were triggered by a fast-mode shock from a flare site, and they were interpreted as standing fast kink-mode waves.

Nakariakov & Ofman (2001) made use of such flare-related spatial oscillations to determine the magnetic field strength (13 ± 9 G), which in the case of a standing kink wave is related to the period of the oscillation, the density of the loop, and

the length of the loop. Another model used to derive the magnetic field strength from loop oscillations was put forward by Zaĭtsev & Stepanov (1989), which assumes that the oscillation is triggered by a centrifugal force, generated by the evaporating chromospheric plasma moving upward along the magnetic field. In this case, the magnetic field strength is given by the amplitude of the oscillation, as well as the loop density and temperature. The model also predicts loop lengths if collisional damping is assumed. (Or vice versa, density and temperature, if the loop length is known.)

Although waves are observed across the electromagnetic spectrum on the Sun, observations on other stars are rarer. The principal reason for this is that the Sun can be spatially resolved, whereas on stars, the signal for the wave must be strong enough to be observed above the full disk emission. The first oscillation associated with a stellar flare was reported by Rodonò (1974), who observed the flare star II Tau with high-speed optical photometry, and found a long-lived oscillation during flare decay with a mean period of 13 s. In a series of papers in the late 1980's and early 1990's, Andrews and co-workers (e.g., Andrews, 1990) presented optical observations of dMe flare stars, where they observed quasi-periodicities with periods of a few tens of seconds, and put forward the idea that these were coronal loop oscillations. Mullan et al. (1992) also found optical oscillations (periods of the order of a few minutes) in dMe stars, concluding that they more likely arise from a coronal than from a photospheric origin. In a later paper, Mullan & Johnson (1995) found oscillations in X-ray data of dMe stars. These oscillations have periods in the range of several tens to a few hundreds of seconds. They were not associated with any flare, though they were interpreted as coronal loop oscillations. Optical stellar flare oscillations have been observed by Mathioudakis et al. (2003), who found a period of 220 s in the decay phase of a white-light flare on the RS CVn binary II Peg, and also by Zhilyaev et al. (2000), who found coherent oscillations of 13 s and 26 s during the early stages of a flare on EV Lac. Solar observations of soft X-ray flare oscillations, with periods ranging from around 4 to 20 minutes, include work by Švestka (1994);

McKenzie & Mullan (1997); Mariska (2005).

In this work, we investigate the first X-ray observation of an oscillation during a stellar flare. Section 4.3 describes the target, AT Mic, as well as the observation. In Sect. 4.4, we present the data analysis, determining the period and amplitude of the oscillation through wavelet analysis. In Sect. 4.5, we determine the magnetic field strength and the length of the coronal loop by assuming that the oscillation is due to a magneto-acoustic wave. As a validity check, the value of loop length was compared to the value determined from a radiative cooling model, as well as from pressure balance scaling laws. The latter also gives an independent estimate of the magnetic field strength. Finally, we discuss the results and give conclusions (Sect. 4.6).

4.3 Target and Observation

AT Mic (GJ 799A/B) is an M-type binary dwarf, with both stars of the same spectral type (dM4.5e+dM4.5e). Both components of the binary flare frequently. The radius of AT Mic given by Lim et al. (1987) is $2.6 \cdot 10^{10}$ cm, using a stellar distance of 8.14 pc (Gliese & Jahreiss, 1991). Correcting for the newer value for the distance from HIPPARCOS (10.2 ± 0.5 pc, Perryman et al., 1997), and using the fact that the stellar radius is proportional to the stellar distance for a given luminosity and spectral class, we obtain a stellar radius of $r_\star = 3.3 \cdot 10^{10}\,\mathrm{cm} = 0.47\, r_\odot$. The mass of AT Mic given by Lim et al. (1987) is $m_\star = 0.4\, m_\odot$.

For our analysis we used the *XMM-Newton* (Jansen et al., 2001) observations of AT Mic on 16 October 2000 during revolution 156. Raassen et al. (2003) have analysed this data spectroscopically, obtaining elemental abundances, temperatures, densities and emission measures, while a comparative flare analysis between X-ray and simultaneously observed ultraviolet emissions can be found in Mitra-Kraev et al. (2005a). Here, we solely used the 0.2–12 keV X-ray data from the pn-European Photon Imaging Camera (EPIC-pn, Strüder et al., 2001).

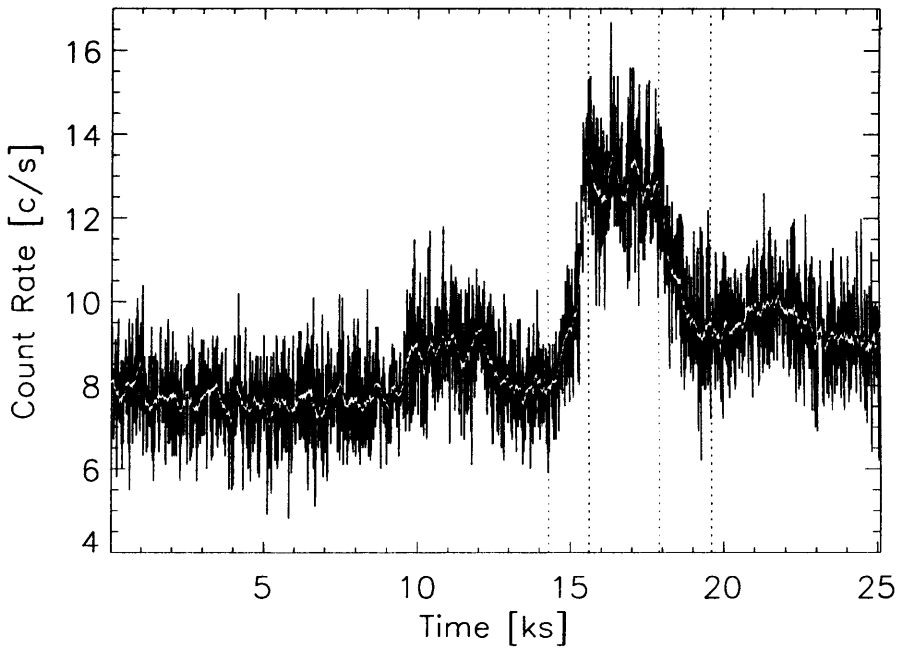

Figure 4.1: The AT Mic 0.2–12 keV X-ray 10-s bin light curve (shown in black). Overplotted in white is the same light curve smoothed with a sliding time window of 200 s. The time is in ks, starting from the beginning of the observation (2000-10-16 00:42:00). The vertical dotted lines mark the flare start, end of rise phase, end of extended top phase and end of the flare.

Figure 4.1 shows the AT Mic light curve. The observation started at 00:42:00 and lasted for 25.1 ks (~7 h). A large flare, starting ~15 ks into the observation, increases the count-rate from flare onset to flare peak by a factor of 1.7, and lasts for 1 h 25 min. It shows a steep rise (rise time $\tau_r = 1300$ s) and decay (decay time $\tau_d = 1700$ s). There is an extended peak to this flare, which shows clear oscillatory behaviour. Applying a multi-temperature model, Raassen et al. (2003) obtain a best fit with a mean flare temperature $T = 24 \pm 4$ MK and a quiescent temperature $T_e = 13 \pm 1$ MK, and from the O VII line ratio a flare and quiescent electron density of $n = 4^{+5}_{-3}\,10^{10}\,\mathrm{cm}^{-3}$ and $n_e = (1.9 \pm 1.5)\,10^{10}\,\mathrm{cm}^{-3}$, respectively. The total flare and quiescent emission measures are $\mathrm{EM} = (19.5 \pm 0.8)\,10^{51}\,\mathrm{cm}^{-3}$ and $\mathrm{EM}_e = (12.2 \pm 0.5)\,10^{51}\,\mathrm{cm}^{-3}$. The total emitted energy in the 0.2–12 keV band of this flare is $\sim 6 \cdot 10^{32}$ erg (Mitra-Kraev et al., 2005a).

4.4 Analysis

4.4.1 Data preparation

For the extraction of the EPIC-pn light curve we used the *XMM-Newton* Science Analysis System (SAS) version 6.0. Light curves with a cadence of 1 s were extracted for concentric regions around the source (20:41:51.156, -32:26:11.02, ICRS 2000 coordinates), and a background, off-set from the source on the same detector chip (20:41:48.428,-32:29:00.66); both regions used a radius of 41.325 arcsec. The selected energy range is 0.2–12 keV (λ = 1–62 Å). The obtained errors for the count rates follow Poisson statistics for all data points. The background light curve is subtracted from the source light curve. Data missing due to telemetry absences are identified by obtaining the 1-s light curve of the entire detector chip; they manifest as time intervals with zero count rate. At such times, the background-subtracted raw light curve is interpolated. This light curve is then re-binned to 10-s bins and used for further analysis.

4.4.2 Continuous wavelet transform and frequency band decomposition

We apply a continuous wavelet transform (CWT) to the 10-s light curve, following the approach laid out by Torrence & Compo (1998). For our analysis, we use the Morlet wavelet $\Psi_0(\eta) = \pi^{-1/4} e^{i6\eta} e^{-\eta^2/2}$. Figure 4.2 displays the CWT. The vertical dotted lines denote the start (14.3 ks), the end of the rise phase (15.6 ks), the beginning of the decay phase (17.9 ks) and the end (19.6 ks) of the flare. The contours give significance levels of 68%, 95% and 99.9%, respectively. At flare rise, the power is enhanced at all timescales in the CWT. The bold arrow points to the flare oscillation, which causes a local maximum in the wavelet coefficient plane. It has a period between 500 and 1200 s and occurs during flare maximum, with a significance level of $> 99.9\%$. Note that there is another local maximum of 68% significance at a period of $\sim$1000 s occurring during a weaker flare at around $t =$ 10 ks, which suggests that this earlier flare might oscillate as well. A third, minor flare at $t = 22$ ks, on the other hand, shows no oscillation. Here, we investigate only the major oscillation during the largest flare.

We split the CWT into three frequency bands with periods of $P > 1200$ s, $500\,\mathrm{s} < P < 1200$ s, and $10\,\mathrm{s} < P < 500$ s, so that the middle band encompasses only the oscillation range. The light curve is reconstructed for the three bands separately. Figure 4.3 shows these decomposed light curves (upper three panels), and their sum, the reconstructed light curve (lowest panel). As the decomposition is a linear transform, it is easy to derive the standard errors for the decomposed light curves (see the following section, Sect. 4.4.3, for the error treatment in our CWT analysis), they are represented by the shaded areas around each light curve. Figure 4.3 demonstrates how the oscillation has been separated from the flare profile, allowing the oscillation to be analysed separately.

Figure 4.4 shows the isolated oscillation (solid line) to which we fit a damped sine curve (dashed line). The fitted curve has an oscillation with a period of $P = 750$ s,

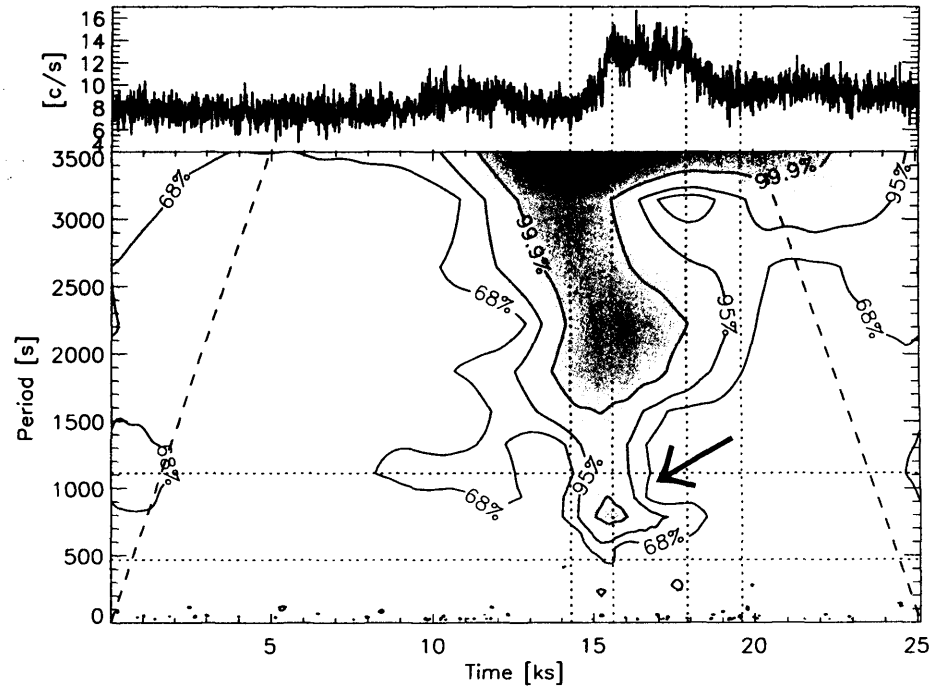

Figure 4.2: The upper panel shows the 10-s bin light curve. The lower panel displays the high-frequency wavelet coefficients of the continuous wavelet transform of the above light curve, using a Morlet wavelet (see Sect. 4.4.2). The contours give the 68%, 95% and 99.9% significance levels. The dashed lines represent the cone of influence. The vertical dotted lines are the same as in Fig. 4.1. The arrow points to the flare oscillation in the wavelet domain and the horizontal dotted lines mark the division between the high (noise), medium (oscillation) and low frequency ranges.

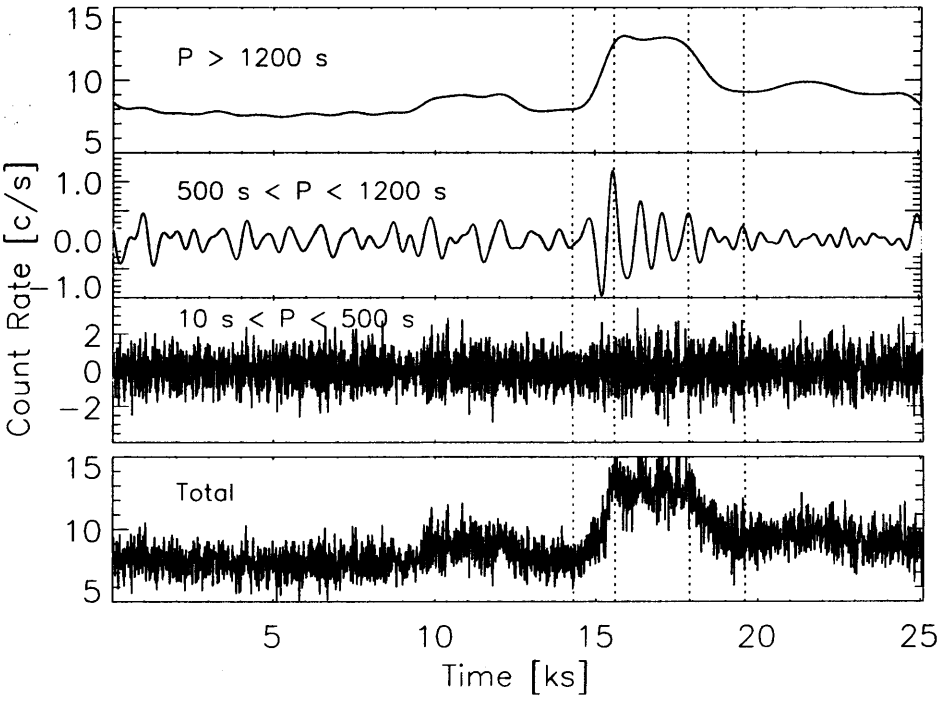

Figure 4.3: The reconstructed light curve divided into three frequency bands, low ($P > 1200$ s), medium (500 s $< P <$ 1200 s, including the oscillation) and high (10 s $< P <$ 500 s, mainly noise); together they add up to the original data (lowest panel). The shaded areas show the standard errors. The vertical dotted lines are the same as in Fig. 4.1. A coherent oscillation is easily identified during flare peak.

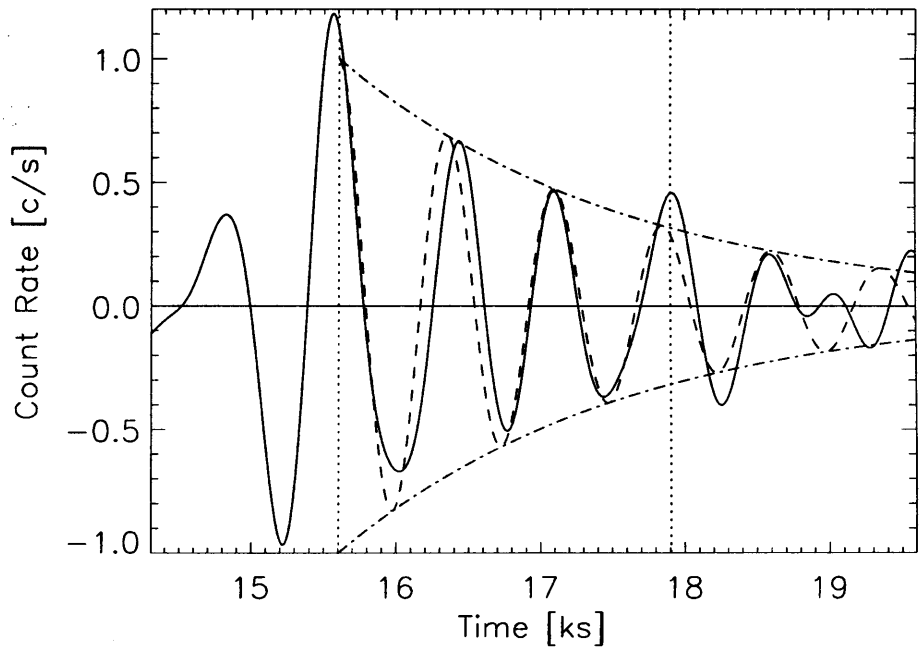

Figure 4.4: The flare part of the $P = 500...1200$ s reconstructed light curve (Fig. 4.3, second panel). The vertical dotted lines bound the flare top. The solid line shows the reconstructed light curve from the data, whereas the dashed line is a damped sine curve (bounded by the exponential envelope, dashed-dotted line) with an oscillation period of $P = 750$ s and an exponential decay time of $\tau = 2000$ s. The relative peak-to-peak amplitude is initially 15%.

an exponential decay (damping) time of $\tau = 2000\,\mathrm{s}$, and an amplitude of $1\,\mathrm{count\,s^{-1}}$, which gives, with an average count rate of $13\,\mathrm{counts\,s^{-1}}$ during flare peak (from the low-frequency light curve), a peak-to-peak amplitude of $\Delta I/I = 15\%$.

A continuous wavelet transform is able to provide us with all our aims simultaneously: the wave is located in time and frequency (=1/period), it is naturally isolated from the underlying flare profile and thus the amplitude and damping are easily available from the fit parameters for a damped sine wave. The low signal-to-noise ratio is dealt with by disentangling the high frequencies from the lower oscillating frequency. In particular, this provides us with a better estimate for the amplitude. While the period derived from the smoothed light curve is broadly the same as the period obtained from wavelet analysis, the amplitude $\Delta I/I = (I_{max} - I_{min})[(I_{max} + I_{min})/2]^{-1} = 10\%$, with I_{max} (I_{min}) the intensity at the first peak (dip), is considerably underestimated.

4.4.3 CWT error analysis

In this section, we derive the error used in our CWT analysis. The continuous wavelet transform of the signal f is given by convolving the signal with a wavelet function Ψ

$$W = \Psi * f \tag{4.1}$$

or in components:

$$W_{jn} = \sum_m \Psi^*_{jnm} \cdot f_m, \tag{4.2}$$

with $W_{jn} = W(t_n, s_j)$, $\Psi_{jnm} = \Psi\left(\frac{(n-m)\Delta t}{s_j}\right) = \sqrt{\frac{\Delta t}{s_j}}\,\Psi_0\left(\frac{(n-m)\Delta t}{s_j}\right)$, $f_m = f(t_m)$, the * denoting the complex conjugate and the scale $s_j = s_0\,2^{j\delta j}$. In our analysis, we set $s_0 = 1$ and $\delta j = 0.25$ for the Morlet wavelet. Significance levels can be derived as

$$\sigma^{\mathrm{Re}}_{jn} = \sqrt{\sum_m \mathcal{R}e(\Psi_{jnm})^2 \cdot \sigma^2_m} \tag{4.3}$$

$$\sigma^{\mathrm{Im}}_{jn} = \sqrt{\sum_m \mathcal{I}m(\Psi_{jnm})^2 \cdot \sigma^2_m} \tag{4.4}$$

$$\chi^2 = \left(\frac{\mathcal{R}e(W_{jn})}{\sigma_{jn}^{\mathrm{Re}}}\right)^2 + \left(\frac{\mathcal{I}m(W_{jn})}{\sigma_{jn}^{\mathrm{Im}}}\right)^2 \equiv \chi_2^2 \tag{4.5}$$

for σ_m^2 the variance of f_m, and χ^2 the χ^2-distribution of W_{jn}. The signal can be reconstructed by using

$$f_n = c \cdot \sum_j \frac{\mathcal{R}e\{W_{jn}\}}{\sqrt{s_j}}, \tag{4.6}$$

with c the normalisation constant (see, e.g., Torrence & Compo, 1998). If a filter F is applied to the wavelet coefficients, $\widetilde{W}_{jn} = W_{jn} \cdot F_{jn}$, the filter coefficients being 0 or 1, the filtered signal is then given by

$$f_n = c \cdot \sum_j \frac{\mathcal{R}e\{\widetilde{W}_{jn}\}}{\sqrt{s_j}}. \tag{4.7}$$

Inserting Eq. (4.2) into Eq. (4.7) and rearranging the sums, we obtain

$$f_n = \sum_m A_{mn}\, f_m, \tag{4.8}$$

with

$$A_{mn} = c \cdot \sum_j \frac{\mathcal{R}e\{\Psi_{jnm}\} \cdot F_{jn}}{\sqrt{s_j}}. \tag{4.9}$$

Thus, the signal can be filtered and reconstructed using a linear transform, which is determined by the wavelet function and the filter. The variance of the reconstructed light curve is then given by

$$\sigma_n^2 = \sum_m A_{mn}^2\, \sigma_m^2. \tag{4.10}$$

The signal can be decomposed without loss, if the sum of the different filters used is 1 for all filter components.

4.5 Results

Our analysis clearly shows that there is an oscillation during the X-ray flare on AT Mic. The oscillation, which has a confidence level $> 99.9\%$, starts when the flare reaches its maximum and continues during the extended flare top. A damped sine

curve with an oscillation period of $P = 750\,\mathrm{s}$ and an exponential decay time of $\tau = 2000\,\mathrm{s}$ fits the data. The initial relative amplitude is $\Delta I/I = 0.15$.

In the following, we investigate the different types of magneto-acoustic loop oscillations. Comparing their various estimates for the flare loop length with two other, independent methods for the loop length, namely from radiative cooling times and from pressure balance, we find the most likely oscillation mode. We also derive the magnetic field strength.

4.5.1 Magneto-acoustic waves

Zaĭtsev & Stepanov (1989) introduced a model, where a hard X-ray oscillation is excited by a centrifugal force, which the evaporating plasma exerts on the flare loop, stretching the magnetic field lines upward and triggering Alfvén oscillations. In this scenario, the relative amplitude of the oscillation is determined by the additional energy from filling the magnetic flux tube with hot plasma

$$\frac{\Delta I}{I} \approx \frac{4\pi n k_B T}{B^2}. \tag{4.11}$$

With $\Delta I/I = 0.15$, $n = (4 \pm 3) \cdot 10^{10}\,\mathrm{cm}^{-3}$, $T = (24 \pm 4)\,\mathrm{MK}$ and k_B the Boltzmann constant, the magnetic field then is $B = (105 \pm 50)\,\mathrm{G}$.

Roberts et al. (1984) showed that for a straight cylindrical geometry several types of magneto-acoustic wave modes in a magnetic loop are feasible, namely the slow (acoustic), the fast kink and the fast sausage modes. For a standing oscillation in a loop, the loop length L is given by

$$L = jcP/2, \tag{4.12}$$

with P the oscillation period, j the mode number and c the appropriate wave speed. For slow modes in the long wavelength limit, c is the tube speed c_t, with

$$\frac{1}{c_t^2} = \frac{1}{c_s^2} + \frac{1}{c_A^2}, \tag{4.13}$$

whereas for the fast kink modes, c is the kink speed c_k, with

$$c_k^2 = \frac{nc_A^2 + n_e c_{Ae}^2}{n + n_e}, \tag{4.14}$$

with the sound speed $c_s = \sqrt{\gamma p/\rho}$ and the Alfvén speed $c_A = B/\sqrt{4\pi\rho}$. $\gamma = 5/3$ is the adiabatic constant for a monatomic gas/plasma, p the gas pressure and ρ the plasma density.

The period of the (global) sausage mode is given by $P = 2L/c_p$, where c_p is the phase speed of the sausage mode and lies somewhere between the Alfvén speed inside and the one outside the loop (Nakariakov et al., 2003). A necessary condition for the existence of the global sausage mode is also $L/2a < 0.65\sqrt{n/n_e}$, with a the tube radius. With the measured loop density around double the surrounding density we have $L/2a < 0.9$, which brakes down the geometry of a loop as the loop length (L) then would have to be smaller than the loop cross-section ($2a$). Thus we exclude the sausage mode on these grounds.

The sound speed is $c_s = \sqrt{2\gamma k_B T/m_p} = 1.66{\cdot}10^4\sqrt{T} = (8.1{\pm}0.7)\,10^7\,\mathrm{cm\,s^{-1}}$. Using the centrifugal model and inserting Eq. (4.11) into the expression for the Alfvén speed, we obtain $c_A = (k_B T)^{1/2}[m_p(\Delta I/I)]^{-1/2} = (1.1{\pm}0.1)\,10^8\,\mathrm{cm\,s^{-1}}$. We immediately see that, assuming the centrifugal model, the ratio of Alfvén to sound speed is determined by the relative oscillation amplitude and is $c_A/c_s = [2\gamma(\Delta I/I)]^{-1/2} \approx 1.41$. Using this last relation, the tube speed then is $c_t \approx 0.82c_s = (6.6 \pm 0.6) \cdot 10^7\,\mathrm{cm\,s^{-1}}$. To obtain the kink speed, we also need to know the Alfvén speed outside the loop, c_{Ae}. Assuming the same value for the magnetic field strength inside and outside the loop, $c_{Ae} = c_A\sqrt{n/n_e} = (1.7 \pm 1.4)\,10^8\,\mathrm{cm\,s^{-1}}$. Note the large error because of the large density error. The kink speed then is $c_k = c_A\sqrt{2n/(n+n_e)} = (1.3 \pm 1.1)\,10^8\,\mathrm{cm\,s^{-1}}$. Thus, we have $(c_t = 0.82c_s) < c_s < (c_A = 1.41c_s) < (c_k = 1.65c_s) < (c_{Ae} = 2.05c_s)$.

Assuming a standing slow-mode oscillation, the loop length is $L_{sm} = Pc_t/2 = (2.5 \pm 0.2)\,10^{10}\,\mathrm{cm}$. For a standing fast kink-mode oscillation, a loop length of $L_{fk} = Pc_k/2 = (5 \pm 4)\,10^{10}\,\mathrm{cm}$ is derived.

4.5.2 Loop length from radiative cooling times

The loop length can also (and independently of any oscillation) be estimated from rising and cooling times obtained from the temporal shape of the flare, applying a flare heating/cooling model (see, e.g., Cargill et al., 1995). We follow the approach by Hawley et al. (1995) who investigated a flare on AD Leo observed in the extreme ultraviolet. The shape of this flare is very similar to our flare on AT Mic, but roughly 10 times larger, and shows a flat top, too.

The flare loop energy equation for the spatial average is given by

$$\frac{3}{2}\,\dot{p} = Q - R, \tag{4.15}$$

with Q the volumetric flare heating rate, R the optically thin cooling rate and $\dot{p}$ the time rate change of the loop pressure. During the rise phase, strong evaporative heating is dominant ($Q \gg R$), while the decay phase is dominated by radiative cooling and strong condensation ($R \gg Q$). At the loop top, there is an equilibrium ($R = Q$). The loop length, assumed to be constant, can be derived as

$$L = \frac{1500}{(1 - x_d^{1.58})^{4/7}} \cdot \tau_d^{4/7} \cdot \tau_r^{3/7} \cdot T^{1/2}, \tag{4.16}$$

where τ_r is the rise time, τ_d the flare decay time (indicated in Fig. 4.2 with the vertical dotted lines), T the apex flare temperature and $x_d^2 = c_d/c_{max}$, with c_{max} the peak count rate and c_d the count rate at the end of the flare. Inserting these values, the loop length is found to be $L \approx 2.5 \cdot 10^{10}$ cm.

4.5.3 Pressure balance scaling laws

To maintain stable flare loops, the gas pressure of the evaporated plasma must be smaller than the magnetic pressure

$$2nkT \leq \frac{B^2}{8\pi}. \tag{4.17}$$

Knowing the flare density and temperature, we get a lower limit for the magnetic field strength $B > 80 \pm 60$ G. Again, there is a large error because of the large

uncertainty for the density. Shibata & Yokoyama (2002) assume pressure balance and give equations for B and L:

$$B = 50 \left(\frac{EM}{10^{48}\,\mathrm{cm}^{-3}}\right)^{-1/5} \left(\frac{n_e}{10^{9}\,\mathrm{cm}^{-3}}\right)^{3/10} \left(\frac{T}{10^{7}\,\mathrm{K}}\right)^{17/10} \mathrm{G} \quad (4.18)$$

$$L = 10^{9} \left(\frac{EM}{10^{48}\,\mathrm{cm}^{-3}}\right)^{3/5} \left(\frac{n_e}{10^{9}\,\mathrm{cm}^{-3}}\right)^{-2/5} \left(\frac{T}{10^{7}\,\mathrm{K}}\right)^{-8/5} \mathrm{cm}. \quad (4.19)$$

Using these relations, we obtain a magnetic field strength of $B = 75 \pm 40\,\mathrm{G}$ and a loop length of $L = (2.8 \pm 1.7)\ 10^{10}\,\mathrm{cm}$.

Combining the above results, we find that both pressure balance considerations as well as the centrifugal oscillation model are consistent. The derived loop lengths from pressure balance and radiative cooling times are consistent with each other and in agreement with the loop length derived assuming a slow-mode oscillation or a fast kink mode. We further discuss the plausibility of the different modes in the following section.

4.6 Discussion and conclusions

We have investigated an X-ray oscillation during a flare on AT Mic, observed by *XMM-Newton*. In order to locate the oscillation in time and frequency, we applied a continuous wavelet transform to the time series, and found that the oscillation, starting at flare peak and continuing during the flare's flat-top phase, with a period around $P = 750\,\mathrm{s}$, has a confidence level of $> 99.9\%$ (Fig. 4.2). We then reconstructed the light curve from the CWT for three different frequency bands (Fig. 4.3). In particular, the light curve passed through a low-pass filter ($P > 1200\,\mathrm{s}$, first panel), displays the overall shape of the light curve and picks out the long-lasting flares, whereas the light curve reconstructed from wavelet coefficients in the range around the oscillation period ($500\,\mathrm{s} < P < 1200\,\mathrm{s}$, second panel), isolates the oscillation. The coherent oscillation during the large flare can be fitted with a damped sine curve with a period of $P = 750\,\mathrm{s}$ and an exponential decay time of $\tau = 2000\,\mathrm{s}$ (Fig. 4.4). The initial, relative peak-to-peak amplitude of the oscillation is found

Table 4.1: Comparison of values derived for the indicated models

Model	Loop length	Magnetic field
Slow mode[a]	$(2.5 \pm 0.2)\ 10^{10}$ cm	
Fast kink mode[a]	$(5 \pm 4)\ 10^{10}$ cm	
Centrifugal force model[b]		(105 ± 50) G
Pressure balance[c]	$(2.8 \pm 1.7)\ 10^{10}$ cm	(75 ± 40) G
Radiative cooling[d]	$2.5 \cdot 10^{10}$ cm	

[a](Roberts et al., 1984)
[b](Zaĭtsev & Stepanov, 1989)
[c](Shibata & Yokoyama, 2002)
[d](Hawley et al., 1995)

to be $\Delta I/I = 15\%$. Decomposing a light curve in such a way is a powerful tool for isolating an oscillation from a flare, as well as disentangling the flare and the oscillation from the high-frequency noise. Because the effect of noise can thus be greatly reduced, this method provides us with a more accurate value for the oscillation amplitude than a value potentially obtained from a binned or smoothed light curve, which is always underestimated, especially if the bins are large.

Interpreting this oscillation as a standing magneto-acoustic wave in the flare loop, we infer that it is a longitudinal slow-mode wave, oscillating at the fundamental frequency. This mode has a node at the loop apex and is capable of causing the largest global flux variations. Using the relations derived by Roberts et al. (1984), we find a flare loop length of $L = (2.5 \pm 0.2)\ 10^{10}$ cm. This value is consistent with estimating the loop length from radiative cooling times of the flare (Hawley et al., 1995) as well as from pressure balance considerations (Shibata & Yokoyama, 2002). Table 4.1 provides a comparison of these results. The derived loop length of a fast kink wave, which has a large error due to a large error in density, is also consistent with the two independent methods of radiative cooling times and pressure balance. This mode, however, is basically incompressible (Nakariakov et al., 2004), and it would be hard to imagine how it could cause intensity perturbations in a spatially

unresolved light curve. We discount fast sausage-mode waves, since they would require a loop aspect ratio ($L/2a$) smaller than 1, in which case the cylindrical geometry assumption breaks down. In summary, we conclude that the observed oscillation is most likely a standing longitudinal slow-mode wave.

To estimate the magnetic field strength, we apply the centrifugal force model of Zaĭtsev & Stepanov (1989), where the magnetic loop is stretched by a centrifugal force which is caused by the upwardly evaporating plasma, stretching the loop beyond equilibrium and thus exciting MHD waves. The flux tube starts to oscillate up and down (i.e. in the plane of the loop), resulting in the excitation of the vertically polarized kink oscillation. The same upflows can also excite acoustic modes, as the particle density inside the loop also oscillates. This acoustic oscillation can be seen in the thermal radiation (soft X-rays and extreme ultra-violet). Non-thermal radiation, originating from gyro-synchrotron (radio) and bremsstrahlung (hard X-rays and optical), caused by fast electrons trapped within the loop and moving back and forth from one end of the loop to the other, also oscillates: the speed of the trapped electrons, and hence the non-thermal radiation, is modulated by the plasma density. The magnetic field strength thus obtained is $B = (105 \pm 50)\,\mathrm{G}$. The large error results from the large uncertainty in the particle density. This value for the magnetic field strength is consistent with pressure balance considerations (Shibata & Yokoyama, 2002), where $B = (75 \pm 40)\,\mathrm{G}$.

The observed rapid damping of the oscillation (a damping time comparable to the oscillation period) is in agreement with other magneto-acoustic wave observations (e.g., Ofman & Wang, 2002; Verwichte et al., 2004). So far, various models have been put forward to explain the fast damping. In the case of slow-mode waves, Ofman & Wang (2002) numerically find that thermal conduction is the dominant dissipation mechanism in loops with $T \geq 6\,\mathrm{MK}$.

An alternative to the interpretation of a standing magneto-acoustic wave causing the flare oscillation is that repeated and rapid flaring is occurring. This might also explain the flat-top character of the time profile of this flare, which differs from the

usual shape of solar flares, which shows a rapid rise from beginning to peak, followed by a slow decay (see, e.g., Švestka, 1989). A possible mechanism to trigger periodic flaring could be an MHD oscillation in a nearby loop (Nakariakov et al., 2006). In any case, the mechanism must be of a periodic and exponentially-decaying nature in order to explain the observed damped oscillation.

The derived length of the flare loop is about the size of the stellar radius and is comparable in absolute size to loop lengths of large solar flares. In particular, Švestka (1994) investigated solar X-ray observations which showed periods close to 20 min. They associated them with spatially resolved large-scale coronal loops with loop lengths of (2–3) 10^{10} cm, and interpreted the oscillations as slow-mode MHD waves. Terekhov et al. (2002) observed an X-ray oscillation with $P = 143$ s during a solar flare, and derived a loop length of (1–3) 10^{10} cm. The centrifugal force model, originally derived for non-thermal X-rays (Zaĭtsev & Stepanov, 1989), has also been applied to millimetre-wave emission (Stepanov et al., 1992), thermal X-rays (Terekhov et al., 2002), and, in the stellar case, to optical emission (Mullan et al., 1992; Mathioudakis et al., 2003).

This is the first time that an oscillation has been observed in X-rays in a stellar flare, and has been used to derive a flare loop length and a local magnetic field strength. Comparable loop dimensions and magnetic field strengths indicate the similar natures of AT Mic's corona and that of our Sun. Because of the smaller radius of these M-type stars ($r_\star \approx 0.5\, r_\odot$), the loop length is in fact of the order of the stellar radius, whereas the magnetic field strength is around the upper limit for solar coronal values. This is consistent with this class of low mass stars (dMe-type) being very X-ray active.

Chapter 5

High-density flares on EV Lacertae

5.1 Summary

This chapter presents detailed statistical analyses of spectral changes in the O VII (21.6–22.1 Å) and O VIII (λ18.97) lines between phases of quiescence and high flaring activity in soft X-ray emission of active M stars. During flares, the plasma is known to become hotter, but also changes in density are anticipated, as the reconnected flare loops will be filled with evaporated chromospheric material. The density can be measured by the ratio of the flux from the forbidden (f) and the intercombination (i) line of He-like triplets, in this case O VII i (λ21.80) and f (λ22.10). The *Chandra* database was searched for flares from dMe stars which were observed with the High Energy Transmission Grating Spectrometer (HETGS). As no flare was adequately bright and long-lasting to produce enough photons for a sufficiently well exposed spectrum, the spectra of several flares were co-added and compared to the quiescent stellar spectrum. The observation of EV Lac was particularly useful to make this comparison, as the first third of the 100 ks observation was relatively quiet, while the remaining part was dominated by many flares. For three other targets, AD Leo, Proxima Cen and AU Mic, a distinction between flaring and quiescent times was not as clear, and the spectra are not sufficiently well exposed to reveal significant

changes. For EV Lac, a significant increase in the O VII *i* line during the flaring phase is found, indicating a strong density increase. Using a bootstrap and cumulative distribution functions, solid statistical confidence limits on line flux changes can be given. An average O VII flare density of $3 \cdot 10^{11}\,\mathrm{cm}^{-3}$ is found, as compared to the quiescent density of $5 \cdot 10^{10}\,\mathrm{cm}^{-3}$. From the measured densities, the flaring volume is estimated at around 10% of the quiet corona.

5.2 Introduction

Coronae of cool stars are likely to be highly structured similar to the solar corona, where the ionised particles are tied to the magnetic field lines. As the emission measure, which is proportional to the luminosity, is given by $\mathrm{EM} = n_e n_p V$, where n_e and n_p are the electron and proton density and V the emitting volume, regions with high densities are brighter than those with low densities. While the solar disk can be observed in detail, stars are unresolved point sources. Any features in the stellar light curve or its spectrum are therefore superpositions of all processes occurring on this star during that time. Flares, huge energy events which can dominate the light curve for a few minutes to several hours, are manifestations of the magnetic field reconnecting to a state of lower potential energy. In this process, the plasma is heated and due to chromospheric evaporation fills post-flare loops and arcades. An increased density of a flare plasma is an indicator of chromospheric evaporation; measuring the loop density and its corresponding emission measure enables us to determine the emitting flare volume, which is unobservable by direct means.

The multi-million degree hot stellar coronae and flares are bright in soft X-rays. The corresponding densities can be obtained from the density-sensitive lines in this spectral range, in particular from the He-like transitions of C V, N VI, O VII, Ne IX, Mg XI and Si XIII (Gabriel & Jordan, 1969; Porquet et al., 2001). In cool stars with a negligible ultraviolet radiation field, the upper level of the forbidden line *f* ($1s\,2s\,{}^3S_1$) has two major channels of transitions into other levels, either radiative decay into

the ground state $1s^2\,{}^1S_0$ (with very long decay times, because this transition is forbidden) or, if the plasma density is sufficiently high, collisional excitation into the upper level of the intercombination line i ($1s\,2p\,{}^3P_1$). With increasing density, the latter transition becomes increasingly important, thus leading to simultaneous reduction in f-line flux and increase in the i-line.

Chandra and *XMM-Newton* allow us to do time-resolved spectroscopy, as all observed X-ray photons are recorded with their individual energy and arrival time. Therefore we can obtain spectra from any given combination of time intervals. In particular, the light curve can be split into flaring and quiescent parts. Ideally, one would like to compare the spectrum of one flare (or a part thereof) to the quiescent state. However, this is only possible for very large flares with many recorded photons. Güdel et al. (2002) observed a huge flare on Proxima Centauri, with a 60-fold increase in soft X-ray flux from pre-flare to peak level, and were able to determine densities from the O VII and Ne IX f/i ratio for different flare stages, the density increasing 20-fold from pre-flare to peak level (from $2 \times 10^{10}\,\mathrm{cm}^{-3}$ to $4 \times 10^{11}\,\mathrm{cm}^{-3}$) and then gradually decreasing again. However, it requires a great deal of luck to capture such a huge flare in the course of only 20–30 hours of observation, the characteristic time usually allocated for stellar X-ray observations. The huge flare of Proxima Cen was to date the only one large enough to do time-resolved density analysis in X-rays. More common are flares with flux increases of a few times the pre-flare value. Attempts were made to obtain flare versus quiescent densities from such more averaged sized flares (Raassen et al., 2003; van den Besselaar et al., 2003), and trends toward higher densities for flares were inferred, but the photon-count statistics were not high enough to measure a significant increase in density (the 1σ errors were overlapping). More common are density comparisons between different stars (Ness et al., 2001, 2002; Testa et al., 2004a).

Recently, Maggio & Ness (2005) found density variations measured from spectral lines in the corona of AD Leo between exposures taken several months apart. The intercombination lines of the Ne IX and Si XIII He-like triplets were strongly enhanced

for the observation where the light curve seems to be in the declining phase of a large flare, as opposed to the observation where the emission was at a relatively constant low level. Based on these findings, our aim was to search particularly for (i) observations with flares, and (ii) for any changes in intercombination line fluxes between flare and non-flaring part of an observation, to ascertain whether the density changes can be positively attributed to flares. Once a flare density is measured, the emitting flaring volume can also be estimated.

Therefore, we searched the *Chandra* High-Energy Transmission Grating (HETG) archive for stellar flares, in particular from dMe stars, and looked for variability in the i and f lines of He-like triplets between quiescent and active stages. Here, the focus is entirely on the O VII lines (resonance line r at 21.60 Å, i at 21.80 Å, f at 22.10 Å), as this line triplet is well separated and unblended. The EV Lac observation was the only one from a flare star which has distinct flaring and quiescent stages, allowing to compare the two. Neither flare itself is large enough to analyse its spectrum alone, but combining all bigger flares we are able to extract an active spectrum with an adequate signal-to-noise ratio. Finding strong indications for significant line changes in the i line of O VII for our manually chosen active versus quiescent spectrum, we devised a bootstrap to estimate the statistical significance of the observed variations, and find that the variations are indeed significant. An earlier analysis of the same observation was made by Osten et al. (2005), who additionally presented simultaneous observations with radio, optical and ultraviolet. They concluded that the density changes between quiescent and flares derived from f/i ratios are not significant. However, they did not devise a bootstrap, nor applied any other elaborate statistical analysis tools. Because the flares are relatively short, close in time but differing manually chosen flare intervals can have quite different f/i ratios. Thus, comparing only one active to a quiescent spectrum without taking statistical behaviour into account can lead to inconclusive findings. The bootstrap method for the oxygen lines is also applied to three other dMe-star observations (Proxima Cen, AD Leo and AU Mic), but no significant density variations are found there, mainly

because there was no clearly identifiable flaring versus quiescent state, and the flares are even smaller. From the f/i ratios of the EV Lac observation we derive densities and also estimate the flaring volume.

We also derive temperatures from the $G = (f + i)/r$ as well as from the r/Lyα ratios, and briefly discuss the inconsistencies between the two. We check for resonance scattering, which might be an explanation for the large G-ratio, but cannot be confirmed in other lines. However, the problem can be resolved by allowing for a recombining flare plasma, i.e., a plasma not in thermal equilibrium. This last point will be analysed and discussed in more detail in the following chapter.

5.3 Data reduction

We extracted light curves and grating spectra utilizing the *Chandra* Interactive Analysis of Observations (CIAO) software, version 3.2.1, following the science threads for CIAO 3.2[1]. The CIAO software allows us to apply time filters. As each detected photon is recorded with its energy and arrival time, we can define any number of non-consecutive time intervals and extract photons that arrive within these times.

The photons detected through *Chandra*'s High-Energy Transmission Grating Spectrometer (HETGS or HETG) are recorded in a two-dimensional array, the zeroth order of the grating spectrometer forming an image of the star (point-source), while the higher orders of the spectrum are projected outwards from the stellar image in a line according to their diffraction, plus and minus orders in opposite directions. The two gratings, the Medium-Energy Grating (MEG) with a range of 2.5–26 Å and the High-Energy Grating (HEG) with a range of 1.7–17.5 Å form two such lines (or arms) at an angle of 10°. In this chapter, only the MEG data is used, as the focus is laid on the oxygen lines, which are beyond the wavelength range covered by HEG.

All the data older than version DS 7.3.0 had to be reprocessed, starting with

[1] http://cxc.harvard.edu/ciao/threads/

the level 1 event file (evt1). If the observation was processed before DS 7.4.0, the `acis_detect_afterglow` correction was removed with `dmtcalc`, ACIS hot pixels and cosmic ray afterglows identified (`acis_run_hotpix`), creating a new bad-pixel file, which was then incorporated into a new evt1 file using `acis_process_events`. The position of the zeroth-order image was then obtained with `tgdetect`, the region mask created with `tg_create_mask`, and grating events to spectral orders assigned (`tg_resolve_events`). This gives a new level 1.5 event file. A new level 2 event file (evt2) is then generated by applying grade/status and Good Time Interval (GTI) filters (`dmcopy`). Next, the `destreak` tool was applied to remove falsely deposited charge on the ACIS detector chips. Afterwards, a barycenter correction (`axbary`) was applied to the evt2 file, accounting for the difference in photon arrival times as the Earth and *Chandra* move around the Sun. The grating spectrum (pha2) is then extracted from the evt2 file with `tgextract`. From this, the grating RMFs and ARFs were created (`mkgrmf` and `fullgarf`) for the +1 and -1 order spectra of MEG and HEG. The light curve was extracted from the evt2 file (`dmextract`) for the HEG and MEG grating arms individually, excluding the zero order photons. Now, specific quiescent and flaring time intervals are chosen according to the light curve, and using them, quiescent and flaring spectra were extracted from the evt2 file. The +1 and -1 order time-filtered spectra were co-added using the RMFs and ARFs of the entire observation.

5.4 Analysis and results

In this section, the data analysis method is described using the observation of EV Lac. First, the light curve and spectra of EV Lac are presented (Sect. 5.4.1), then the statistical analysis method introduced using EV Lac data (Sect. 5.4.2), and finally the statistical method is also applied to three other dMe stars (AD Leo, AU Mic and Proxima Cen) in Sect. 5.4.3.

5.4.1 Light curve and spectra

Figure 5.1 (top panel) shows the light curve of EV Lac observed with *Chandra*. It has a quiet (Q) phase during the first part of the observation and an active (A) phase during the second part, which makes it an ideal candidate to look for spectral changes between the two phases. As none of the flares are large enough to accumulate sufficient photons during its duration to obtain a spectrum with an adequate signal-to-noise ratio, we sum up the photons of several flares in order to obtain a flaring spectrum with a reasonably good signal-to-noise ratio. Of course, physical properties of individual flares may differ widely, and we keep in mind that by co-adding several flares we can only gain information about their average, which need not coincide with any individual flare.

We split the observation manually into a flaring (black) and a quiescent (blue) part, and reduce the spectrum of each. The lower left panel of Fig. 5.1 shows the X-ray spectrum in the range of 21.4–22.2 Å, containing the He-like O VII line triplet, with the resonance line r at 21.6 Å, the intercombination line i at 21.8 Å, and the forbidden line f at 22.1 Å. The spectrum in black was obtained from the flaring phase of the observation and corresponds to the black part of the light curve, while the blue part corresponds to the quiescent phase of the observation. The thickness of the spectral lines outlines the standard error, which roughly means that if the lines overlap there is no significant change in line intensity from one spectrum to the other, while if they are well separated the change is significant. The lower right panel of Fig. 5.1 displays the O VIII Lyα line, centred around 18.97 Å, for the same data.

In collisionally ionised plasmas, which is the case for stellar coronae, the line ratio $R \equiv f/i$ is density sensitive and decreasing with increasing density, while the line ratio $G \equiv (f+i)/r$ is temperature sensitive and decreasing with increasing temperature (Gabriel & Jordan, 1969; Porquet et al., 2001). Of the O VII line triplet (Fig. 5.1, bottom left panel), the intercombination line is the only line showing a

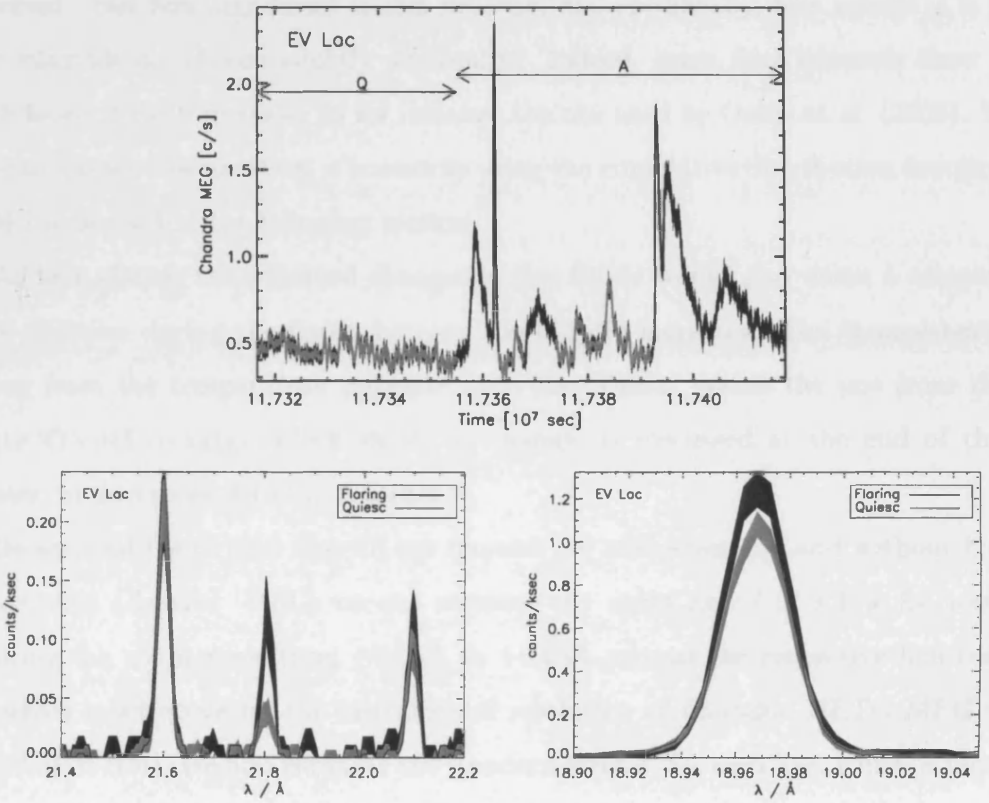

Figure 5.1: The *Chandra* HETG-MEG light curve (top), O VII-triplet (bottom left) and O VIII line (bottom right) of EV Lac. The light curve was divided into flaring (black) and quiescent (blue) time intervals. The two different coloured spectra correspond to these times. For illustrating purposes, the spectra were smoothed by a factor of 5, matching the instrumental resolution of 0.023 Å. The thickness of a spectral line corresponds to its standard error. The light curve, with an observing cadence of 3.24104 s, was binned by a factor of 10 and smoothed by a factor of 20 for the plot; the 1σ error bars are plotted about every 160 s; and the time is given in seconds after midnight of 1 January 1998. The quiet (Q) and active (A) phase of the observation as defined in the left panel will be used for the analysis in Sect. 5.4.2.

significant increase from the quiescent to the flaring state. The other two lines remain at the same flux level. This means that the density during the flares is increased. But how significant is this increase, and specifically, how robust is it if flare intervals are chosen slightly differently? Indeed, some flare intervals show a much lesser density increase, as for instance the one used by Osten et al. (2005). In order to answer this question, a bootstrap using the cumulative distribution function (CDF) is devised in the following section.

At first glance, the obtained changes in line fluxes would also mean a temperature decrease during the flares, because the G-ratio increases. The inconsistency arising from the temperature estimate from the G-ratio versus the one from the O VII r/O VIII Lyα-ratio, which shows no change, is discussed at the end of this chapter, and in more detail in Chapter 6.

Because all the oxygen lines of our interest are well separated and without line blends with *Chandra* MEG, we can measure the count rate l of a line by accumulating the count rates from -0.05Å to $+0.05$Å around the respective line centre, which is adequate for the instrumental resolution of *Chandra* HETG-MEG of 0.023Å (FWHM). We also estimate the standard error σ_l for each line, which is measured and basically follows Poisson statistics (square root of the number of photon counts). The background and continuum are neglected, as they are both small. For each spectral line, we calculate the count-rate excess (difference between flaring and quiescent) $\Delta l \equiv l_1 - l_2$, where $l_{1,2}$ is the count rate of a line from spectrum 1 and 2, respectively. We use the notation $l = i$ for the O VII intercombination line, $l = f$ for O VII forbidden line, $l = r$ for O VII resonance line, and $l = \alpha$ for O VIII-Lyα line. The corresponding error $\sigma_{\Delta l}$ is given by error propagation $\sigma_{\Delta l}^2 = \sigma_{l_1}^2 + \sigma_{l_2}^2$, where σ_{l_1} and σ_{l_2} is the error in l_1 and l_2, respectively. We also introduce the notation ${}^l\Phi \equiv \Delta l/\sigma_{\Delta l}$, which is the count-rate excess of a line in units of its standard error (a value of ${}^l\Phi = 0$ means identical fluxes, $l_1 = l_2$, a value of ${}^l\Phi = 1$ means that the lines differ with a significance of 1σ).

5.4.2 Statistical assessment

How significant is ${}^{l}\Phi$? To answer this question we devise a bootstrap by reconstructing the cumulative distribution function (CDF) for each line. The CDF is defined as $F(\Phi) \equiv \int_{-\infty}^{\Phi} f(\phi)\, \mathrm{d}\phi$, where $f(\phi)$ is the normalised probability density function. Thus, Φ is an increasing function from 0 to 1 over $-\infty < \Phi < \infty$. Practically, we get the CDF by obtaining a large set of random variables (observations) Φ_n, with $n = 1, 2, ..., N$ and N the number of elements in the set, so that the variables are sorted ($\Phi_{n+1} \geq \Phi_n$ for all n). For $\Phi_n \leq \Phi < \Phi_{n+1}$, the CDF is then given by $F(\Phi) = n/N$.

We obtain the CDFs by slicing the observation into 12 or less random, disjoint time intervals, then co-adding the photons of the even sections into one and the photons of the odd sections into the other spectrum, such that the two spectra add up to the total observation (each photon is associated to either one of the two spectra), and assigning one of the two spectra randomly as spectrum 1 and the other one as spectrum 2. We then calculate ${}^{i}\Phi$, ${}^{f}\Phi$, ${}^{r}\Phi$, and ${}^{\alpha}\Phi$ for this spectral pair. This process is repeated 1000 times so that each ${}^{l}\Phi$ has $N = 1000$ elements. As an additional constraint, we only allow pairs of spectra where each of the pairing spectrum was accumulated over at least 20 ks (in the case of EV Lac, at least 10 ks for the other targets); this is to ensure a reasonable signal-to-noise ratio for each spectrum and results in an actual N which is somewhat smaller than 1000.

Figure 5.2 shows the CDFs $F({}^{i}\Phi)$, $F({}^{f}\Phi)$, $F({}^{r}\Phi)$, and $F({}^{\alpha}\Phi)$ for the entire EV Lac observation. For comparison, the line between the shaded and the white area is the CDF of the normal distribution $\int_{-\infty}^{\Phi} \frac{1}{\sqrt{2\pi}} \mathrm{e}^{-\frac{\phi^2}{2}}\, \mathrm{d}\phi$. First, we notice that all the CDFs are symmetric around $\Phi = 0$ and $F = \frac{1}{2}$, which confirms that our statistics is unbiased, as the ${}^{l}\Phi$'s are random and therefore have equal probability to be positive or negative. As the spectral noise is dominated by Poisson statistics, $F({}^{l}\Phi)$ is expected to follow the normal distribution if the line does not change

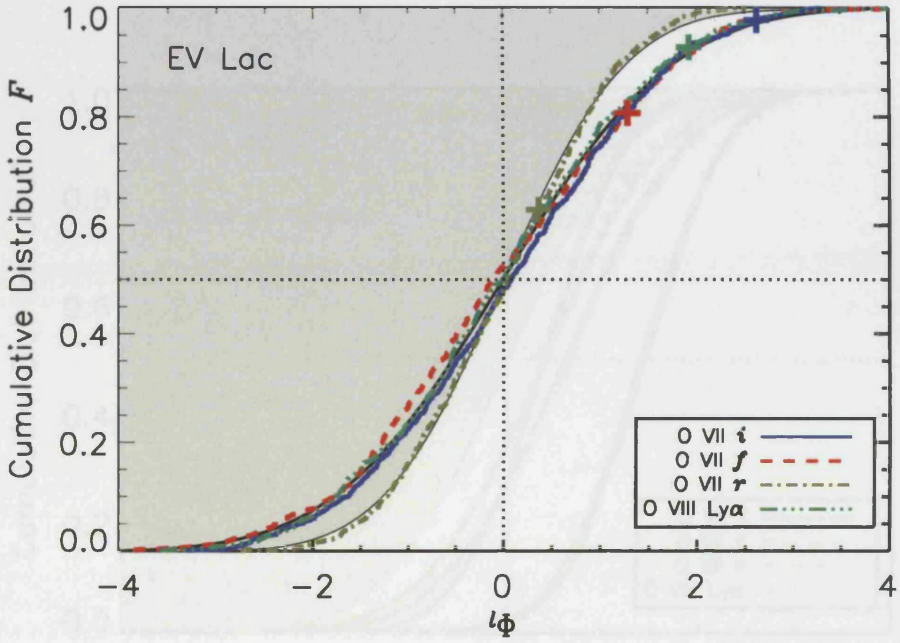

Figure 5.2: The cumulative distribution functions (CDFs) for the O VII-i (21.8Å), O VII-f (22.1Å), O VII-r (21.6Å), O VIII-Lyα (18.97Å) line difference in units of its standard error (see main text) between two disjoint random spectra of the entire EV Lac observation. The dividing line between the grey shaded and the white region in the graph is the CDF of the normal distribution. The r-line follows the normal distribution, implying that there is no variation beyond noise statistics. The CDFs for the other lines are all broadened, implying a significant change beyond noise, i.e. line variability due to density or temperature changes. The crosses mark the values corresponding to the line differences of the two manually selected spectra shown in Fig. 5.1, the values being $F(^{i}\Phi) = 0.98$, $F(^{f}\Phi) = 0.81$, $F(^{r}\Phi) = 0.63$, $F(^{\alpha}\Phi) = 0.93$.

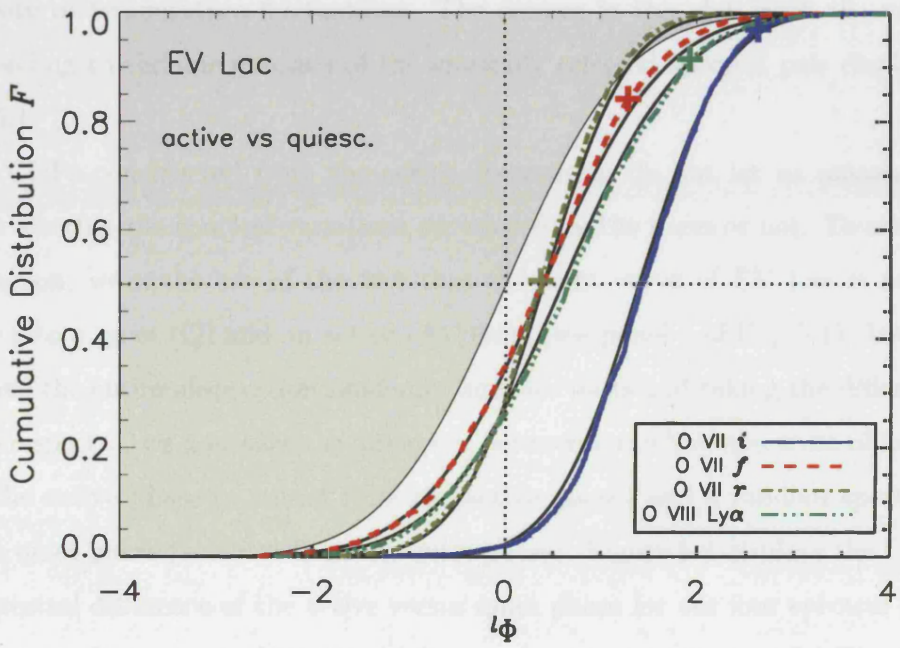

Figure 5.3: Same as Fig. 5.2, except that the line excess is calculated from the difference of a random spectrum from the active phase and a random spectrum from the quiet phase. All the lines are shifted toward positive ${}^{l}\Phi$, indicating a generally higher flux during flare activity than during quiescence. The i line is shifted the most, being the only one where more than 95% of the distribution has positive values. The crosses marking the values of the two manually chosen spectra are at $F({}^{i}\Phi) = 0.97$, $F({}^{f}\Phi) = 0.84$, $F({}^{r}\Phi) = 0.51$, $F({}^{\alpha}\Phi) = 0.92$.

intrinsically during the entire observation, but only fluctuates because of photon-count uncertainty. This is the case for $F(^{r}\Phi)$, meaning that the resonance line does not vary beyond flux uncertainty. The other CDFs, however, have a broader distribution. They vary more than just because of the photon count uncertainty, but because there is a real change in the physical conditions during the observation, i.e. density or temperature fluctuations. The crosses in the plot mark the values corresponding to the line excesses of the manually selected spectral pair displayed in Fig. 5.1.

The CDFs constructed from the entire observation do not let us answer the question whether the spectral variations are caused by the flares or not. To address this question, we make use of the fact that the light curve of EV Lac is neatly divisible into a quiet (Q) and an active (A) phase (see panel 1 of Fig. 5.1). Instead of dividing the entire observation randomly into two parts and taking the difference of the two spectra, we now take the difference between a random spectrum obtained during the active phase (a subset from the active phase) and a random spectrum from the quiet phase (a subset from the quiet phase). Figure 5.3 displays the CDFs of the spectral difference of the active versus quiet phase for our four spectral lines of interest, again in units of its standard error (same convention as for Fig. 5.2). The shift of all CDFs along the x-axis toward positive values reflects the general flux increase during the active phase compared with the quiet one. The r, f and α lines are shifted only very little, while the i line is shifted considerably toward larger values, implying a relative larger flux increase during flare activity for this line compared with the other ones. The confidence level for a line increase (where $^{l}\Phi > 0$) is 97% for the i line, but considerably smaller for the other lines (66% for f, 68% for r and 74% for α). Therefore we conclude that although the f as well as the α lines along with the i line show flux variations during the entire observation (because of a deviation from the normal distribution, see Fig. 5.2), the i line is the only one which is significantly (with a confidence level of 97%) enhanced during flares. The count-rate increase of the i line is also the only one which has a confidence

level above 95% in either and both the distributions (total as well as active versus quiescent).

5.4.3 Results of other dMe stars

Can we also observe temporal variations of the investigated oxygen lines in other flare stars? We analysed the data of AD Leo, Proxima Cen and AU Mic, all active M-type dwarfs like EV Lac which were also observed by *Chandra* HETG. Figure 5.4 shows the light curve (left panels) of, from top to bottom, AD Leo, Proxima Cen and AU Mic, again manually divided into two parts (black and blue), and the corresponding spectral lines of O VII (middle panels) and O VIII (right panels). AD Leo and AU Mic have many small flares or fluctuations comparable to the small variations during the quiescent phase of the EV Lac observation, where the flux level changes by less than a factor of 2. In comparison, the flux changed by up to a factor of 4 during the flares of EV Lac. These ongoing small variations make it impossible to split any of the observations into two different activity stages like the one for EV Lac, thus only statistical behaviour of the total observation can be determined, but no comparison between two different phases is possible. Proxima Cen has a flare at the beginning of the observation with a flux increase by a factor of approximately 3 and thereafter stays at a very low emission level. The flux level of the quiescent phase of Proxima Cen is at about half the level of any of the other quiet emission levels. Therefore, the signal-to-noise ratio is rather poor, which is reflected in the weak lines and large error regions of the spectrum. By looking at each pair of the manually chosen spectra, none of the oxygen emission lines of these three stars varies significantly, except for the O VIII line of Proxima Cen, which is because of the larger flux and suggests a higher temperature during the flare.

Figure 5.5 shows the CDFs, obtained in the same manner as Fig. 5.2 for EV Lac (Sect. 5.4.2), for the oxygen lines of AD Leo, Proxima Cen and AU Mic. In AD Leo (left panel), the i and α lines are normally distributed, while r and f show a small

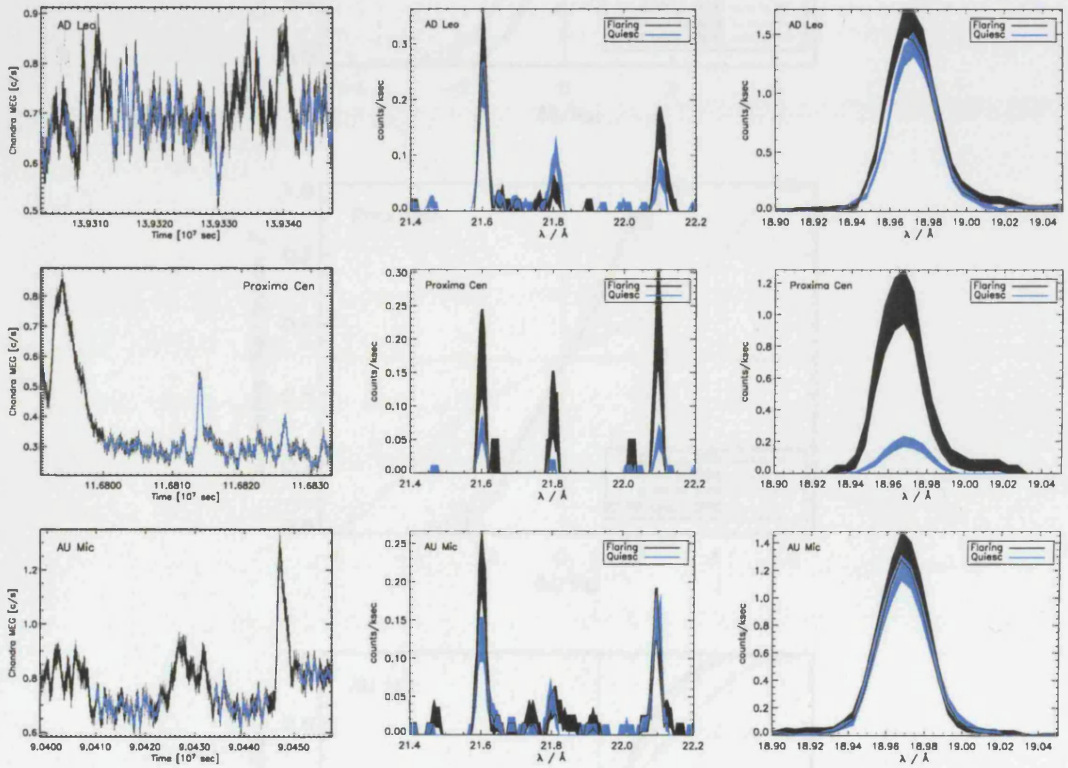

Figure 5.4: Light curves and spectral lines of, from top to bottom, AD Leo, Proxima Cen and AU Mic.

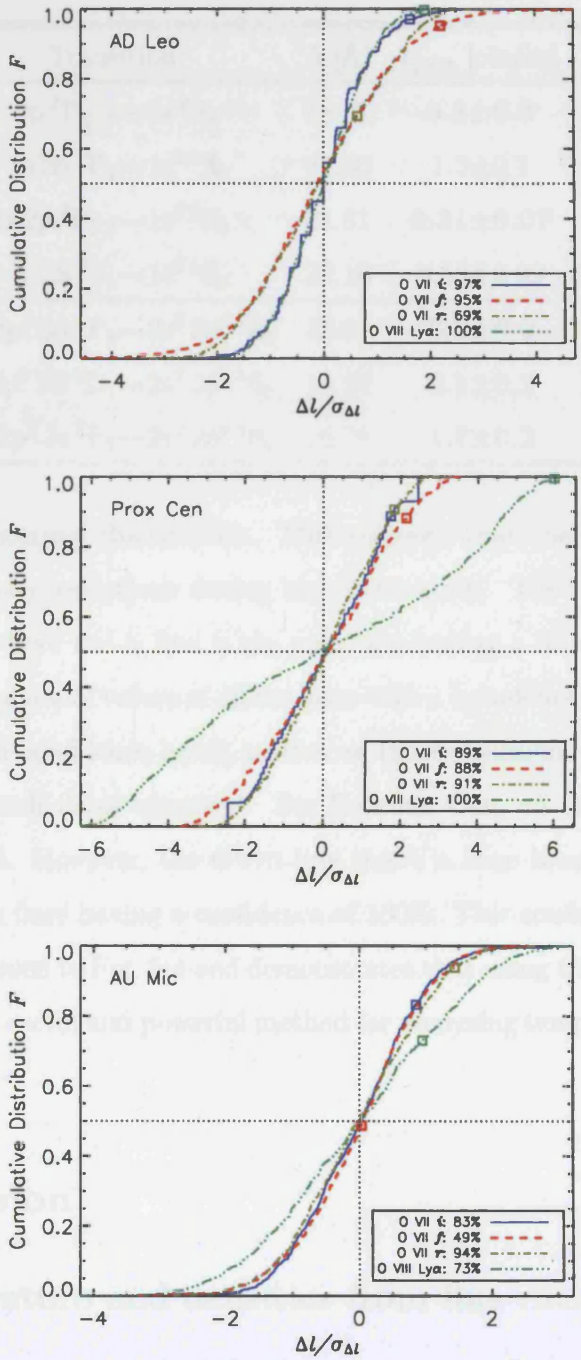

Figure 5.5: Cumulative distribution functions of the count-rate excess of the spectral lines O VII-i, O VII-f, O VII-r and O VIII-Lyα, for AD Leo, Proxima Cen and AU Mic.

Table 5.1: EV Lac line count rates. In bold are significant changes.

Ion	Transition	λ [Å]	l_{quiet} [cts/ks]	l_{active} [cts/ks]
O VIII Lyα	$2p\,^2P_{\frac{1}{2},\frac{3}{2}} \rightarrow 1s\,^2S_{\frac{1}{2}}$	18.97	**6.8±0.3**	**7.9±0.4**
O VII *r*	$1s2p\,^1P_1 \rightarrow 1s^2\,^1S_0$	21.60	1.3±0.1	1.4±0.2
O VII *i*	$1s2p\,^3P_{1,2} \rightarrow 1s^2\,^1S_0$	21.81	**0.31±0.07**	**0.7±0.1**
O VII *f*	$1s2s\,^3S_1 \rightarrow 1s^2\,^1S_0$	22.10	0.53±0.09	0.7±0.1
Fe XVII	$2s^2\,2p^5\,3d\,^1P_1 \rightarrow 2s^2\,2p^6\,^1S_0$	15.01	**3.3±0.2**	**4.6±0.3**
Fe XVII	$2s^2\,2p^5\,3d\,^3D_1 \rightarrow 2s^2\,2p^6\,^1S_0$	15.26	**2.1±0.2**	**2.8±0.3**
Fe XVII	$2s^2\,2p^5\,3s\,^3P_1 \rightarrow 2s^2\,2p^6\,^1S_0$	16.78	**1.7±0.2**	**2.6±0.3**

deviation from the normal distribution. This suggests that there might be small temperature or density variations during the observation. The same goes for AU Mic (right panel), where the α line is the only one having a broader than normal distribution. As the manual values of all the lines with a broadened distribution have not particularly high confidence levels, neither of these variations can positively be attributed to the small flares observed. For Proxima Cen, all the O VII lines are normally distributed. However, the O VIII line shows a huge broadening, with the manual value for the flare having a confidence of 100%. This confirms the clear line flux change directly seen in Fig. 5.4 and demonstrates that using CDFs to determine confidence levels is a useful and powerful method for analysing temporal flux changes in spectral lines.

5.5 Discussion

5.5.1 Temperature and densities from line ratios

The count rates of relevant lines, both for the quiescent as well as the active phase of the EV Lac observation, are displayed in Table 5.1. Bold numbers indicate significant changes (non-overlapping errors) between the two spectra. Of the oxygen lines,

Table 5.2: EV Lac line ratios and derived densities and temperatures. In bold are ratios which show significant changes.

	quiet (Q)	active (A)	flaring (A-Q)
R = f/i	**1.7±0.5**	**1.0±0.2**	**0.44±0.36**
G = $(f+i)/r$	**0.6±0.1**	**1.0±0.2**	5.6±12.3
$(f+i+r)/\alpha$	0.31±0.03	0.35±0.04	0.6±0.6
r/α	0.19±0.02	0.18±0.03	0.1±2.0
Fe XVII (λ15.26/λ15.01)	0.6±0.1	0.61±0.08	0.5±0.6
Fe XVII (λ16.78/λ15.01)	0.52±0.07	0.57±0.07	0.7±0.5
n_e [10^{10}cm^{-3}]	**5 [3,9]**	**11 [9,16]**	**32 [16,226]**
T_G [MK]	4	1.5	-
$T_{r/\alpha}$ [MK]	4	4	-

O VIII Lyα and O VII i both increase more than the sum of their standard errors, while O VII r and f remain the same.

The first part of Table 5.2 displays various ratios using the numbers from Table 5.1. Both the R- and G- ratios show significant changes between the quiescent and the flaring spectrum. From these ratios, we estimate an electron density n_e and an electron temperature T_G using the tabulated calculations from Porquet et al. (2001). During quiescence, we obtain $n_e = 5 \cdot 10^{10}\,\mathrm{cm}^{-3}$ and $T_G = 4\,\mathrm{MK}$, while during flares the average density doubles $1 \cdot 10^{11}\,\mathrm{cm}^{-3}$, and the pure flare density (as derived from the active minus the quiescent spectrum) is estimated at $3 \cdot 10^{11}\,\mathrm{cm}^{-3}$, with a lower and upper limit of $1.6 \cdot 10^{11}\,\mathrm{cm}^{-3}$ and $2 \cdot 10^{12}\,\mathrm{cm}^{-3}$, respectively. The flare temperature apparently drops by more than a factor of 2. Another temperature estimate using the O VII r to O VIII Lyα ratio ratio remains the same in both spectra and gives temperatures of 4 MK (using the CHIANTI database), the same as the temperature obtained from the G-ratio for the quiescent spectrum. We conclude that there is no measurable oxygen temperature increase during the flares, and that

the G-ratio is altered for other reasons, which will be discussed in the following sections. Therefore, a temperature of 4 MK was used for all density estimates from R-ratios (as the R-ratio is only weakly dependent on temperature, the exact value of the temperature does not matter much anyway), using the tabulated values of Porquet et al. (2001), with the radiation temperature value set to zero.

5.5.2 Resonant scattering

The temperature-sensitive G-ratio is larger for the active phase than what it is for the quiescent phase, suggesting a *lower* temperature during the flares. This contradicts our knowledge about flares, which usually show an increased temperature, and is also not consistent with the temperature derived from the r/Lyα ratio, which remains unchanged. In fact, the overall flare temperature is very high indeed, as is seen in the rise of lines with hotter formation temperature in the entire soft X-ray spectrum (Chapter 6). Therefore, we seek another mechanism responsible for the suppression of the r-line flux. One possibility is resonance scattering, i.e., the absorption of a passing photon of the right energy by photo-excitation and subsequent re-emission of a photon out of the line-of-sight. The transition $^1S_0 \rightarrow {}^1P_1$ (r) is affected by resonance scattering, as its oscillator strength is high, while the transitions $^1S_0 \rightarrow {}^3P_{1,2}$ (i) and $^1S_0 \rightarrow {}^3S_1$ (f) are not subject to resonance scattering, as these atomic transitions would need a change of spin. This means that photons from the r line may get lost or amplified on their way to the observer, depending on the geometry of dense structures, which the photons have to traverse on their way to the observer. In particular, if a dense, elongated structure lies in the path of the photons, resonant photons may be scattered out of the line-of-sight. Such a geometry is possible, especially as we assume the flares to be associated with dense coronal loops. A support for this view is obviously the strong density increase during the flares. The i and f photons, however, are not affected by this scattering effect. Thus, only the resonance line would be suppressed and the overall effect is

an increased G-ratio. Testa et al. (2004b) for instance find a suppression of the Lyα and r lines of oxygen and neon and relate it to resonance scattering.

We test the hypothesis of resonance scattering by looking at line ratios of certain Fe XVII lines, which are particularly sensitive to resonance scattering (Ness et al., 2003). The line at λ=15.01 Å is most affected, while the line at λ=15.26 Å scatters less than a quarter of the λ15.01 line, and scattering of the λ16.78 line is even less probable at only 0.04 times that of the λ15.01 line. We look at both the λ15.26/λ15.01 and λ16.78/λ15.01 ratios during quiescent and active emission, which are listed in Table 5.2. Contrary to findings by Matranga et al. (2005) of flares on AB Dor where resonant scattering is found, both the ratios here do not vary between the two states. Therefore, we reject the hypothesis for resonance scattering and investigate other possibilities.

5.5.3 Transient recombination

Spectra with He-like triplets which show a G-ratio of 4 or more, i.e., the r line is much weaker than the sum of the i and f lines, are indicative of a cooling, recombining plasma (Pradhan, 1985), a plasma which is no longer in ionisation equilibrium. In a cooling plasma, with recombination processes dominating collisional ionisation, the $^1P_1$ state is populated by recombinations and cascades from higher orbit recombinations to a much lesser extent than the ^3P and ^3S states.

Flares are prototypical high-energy, non-equilibrium events, releasing electromagnetic continuum radiation over a wide range of the spectrum, from radio to γ rays. It has earlier been suggested that flare plasma should be treated as a collisional ionizing plasma in its initial phase, and radiative recombining in its gradual cooling phase (Liedahl, 1999), as it is heated by an initial shock and subsequently cools via radiative processes. However, such spectra are rarely observed, because their usual short integration period of a flare duration of only a few minutes yields low signal-to-noise ratios. We will elaborate in more detail on this topic in Chapter 6, where the

pure flare spectrum (active minus quiet spectrum) of EV Lac is presented. Transient recombination is therefore a viable explanation for spectra which were obtained from the decay phase of flares, or a superposition of those with more quiescent emission. The latter may be in a collisional ionisation equilibrium (CIE) state, but the former is not, making it a hybrid plasma where CIE interpretations are no longer valid.

5.5.4 Flaring volume

The emission of the active phase is given by the superposition of the emission of the quiescent phase and the pure flaring emission. Note that the pure flaring emission is an average over all selected flares. Let us assume that the volume from where the active emission originates equals the quiescent emitting volume, i.e., the flare replaces part of the quiet corona. We also use the definition of the emission measure, $\mathrm{EM} = \int n_e n_p \, \mathrm{d}V$, with n_e the electron, n_p the proton density integrated over the emitting volume V. We set $n_p = n_e$ (a more exact approximation usually used is $n_p = 0.85 n_e$) and assume n_e is constant within the emitting volume. This leads to the following identities for volumes and emission measures, with A denoting active, Q quiescent, and F flaring phase

$$\mathrm{EM}_{\mathrm{Q,A,F}} = n^2_{\mathrm{Q,A,F}} \, V_{\mathrm{Q,A,F}} \tag{5.1}$$

$$\mathrm{EM}_{\mathrm{A}} = \mathrm{EM}_{\mathrm{Q}} + \mathrm{EM}_{\mathrm{F}} \tag{5.2}$$

$$V_{\mathrm{A}} = V_{\mathrm{Q}}. \tag{5.3}$$

Rearranging the above equations (e.g., substituting Eqs 5.1 into Eq. 5.2, then replacing V_{A} by Eq. 5.3 and solving for $V_{\mathrm{F}}/V_{\mathrm{Q}}$), we obtain

$$\frac{V_{\mathrm{F}}}{V_{\mathrm{Q}}} = \frac{n^2_{\mathrm{A}} - n^2_{\mathrm{Q}}}{n^2_{\mathrm{F}}}. \tag{5.4}$$

Inserting the values for the densities from Table 5.2, we obtain $V_{\mathrm{F}} \approx 0.1 V_{\mathrm{Q}}$, i.e., the flaring volume is about 10% of the quiescent corona. As the density intervals are adjacent, this is only a rough estimate; within the error margin, $V_{\mathrm{F}}/V_{\mathrm{Q}}$ can take any value from 0 up to almost 1.

5.6 Conclusions

We find that the intercombination line flux of O VII increases significantly during flares on EV Lac, while the other O VII line fluxes remain unchanged. This suggests increased densities (from $\sim$ 5 to 30 $\times$ $10^{10}\,\mathrm{cm}^{-3}$) during flares at 4 MK. For solar flares, similar flare-density enhancements derived from the O VII f/i-line ratio were observed by Doschek et al. (1981). We obtain (i) a quiescent density, (ii) an active density, which is given by the superposition of flares and quiet corona at 4 MK, and (iii) a flaring density, which is derived from the line ratios of the active minus quiescent spectrum. The latter has the largest uncertainties because of error propagation. Based on these densities, the flaring volume is estimated to be around 10% of the quiet coronal volume.

A bootstrap was devised to statistically assess the significance of the line flux changes. Of the lines of the O VII-triplet and O VIII Lyα, and requesting a confidence limit of over 95%, only the O VII i line showed significant flux increase during flares, implying a larger density. The statistical assessment also worked for a flare on Proxima Cen, where the O VIII Lyα line was significantly enhanced due to a hotter temperature. The bootstrap is an excellent method to statistically confirm that a variable is significantly changing, even when the error margins are rather large (over 30% in this case) and a simple comparison between two states is inconclusive.

For collisionally ionised plasma in thermal equilibrium (coronal plasma), the G-ratio can also be used to determine the electron temperature of the plasma. However, the rise in only the intercombination line and not in the resonance or the forbidden line yields a lower flare temperature using the G-ratio, which is counterintuitive and is not supported by the temperature derived from the O VII r/O VIII Lyα ratio. We tested for the occurrence of resonance scattering during flares, which could be a possible explanation, as the photons of the r line would be affected to a much larger extend than the ones from the i or f lines. However, other ratios, namely of Fe XVII lines, which would also be affected by resonance scattering are not changed

between quiescent and flaring state in this observation, so the resonance scattering hypothesis has to be rejected. We suggest that the suppressed resonance flux along with the increased flux in the intercombination line during the flares is due to a recombining plasma (Pradhan, 1985), as is the case for cooling plasmas in non-ionisation equilibria. This is consistent with what we know about flares, high-energy phenomena in thermal non-equilibrium. They cool during their decaying phase, and a 'coronal' plasma assumption is no longer valid.

Chapter 6

The recombining X-ray flare spectrum of EV Lac

6.1 Summary

In this chapter, the pure flaring spectrum of the active M-type star EV Lac is presented, as observed by the *Chandra* observatory in the soft X-ray range 1.7–26 Å. While the quiescent spectrum is in collisional ionisation equilibrium (CIE), as expected for a thermal, coronal plasma, this is no longer true for the flaring spectrum. While, as expected, the latter is dominated by hotter lines than the quiescent one, we also find that certain line ratios of the flaring spectrum are incompatible with a "coronal" plasma in thermal equilibrium. However, they are consistent with a highly ionised, rapidly cooling plasma. These findings have major consequences for interpreting the plasma of active stellar coronae. In particular, such thermal non-equilibrium conditions lead to a suppression of the resonance line and affects the G-ratio of He-like ions, which is often used for temperature diagnostics. Active stellar coronae, where the emission is thought to come from a superposition of numerous small flares, should no longer be treated in CIE, but rather as a hybrid plasma with an additional cooling component. Inconsistencies between the temperature derived

from the G-ratio and temperatures derived by other means can thus be resolved.

6.2 Introduction

Traditionally, a stellar coronal plasma is treated as being collisionally ionised and in thermal equilibrium, which is usually a good approximation. This assumption is normally also made for flaring plasmas. However, coronal flares, which release huge amount of energies on short time scales (several tens of minutes to a few hours), are quintessentially in a non-equilibrium state, and therefore a flaring plasma need not show the same characteristics as a quiescent one. In this chapter, we discuss inconsistencies in the flaring spectrum of EV Lac if it is interpreted as a purely collisionally ionised plasma, and suggest that treating it instead as a recombining plasma resolves the puzzle.

It is generally accepted that a flaring plasma is hotter, as the line emission from ions with higher formation temperature is usually enhanced. Basically, temperatures can be obtained using two types of line ratios: (i) from lines of the same element but in different ionisation states, or (ii) from lines of the same ion. In particular, He- and H-like transitions have good diagnostic capabilities in the X-ray range, as the transitions of C, N, O, Ne, Mg and Si all lie within 1–40 Å. In recent years, during the *Chandra* and *XMM-Newton* era, inconsistencies have been found between estimating the temperature with the G-ratio and by other means, especially for active stellar coronae. It is suspected that the G-ratio, which is given by $\frac{f+i}{r}$, where r is the resonant line transition ($1s^2\,{}^1S_0$–$1s\,2p\,{}^1P_1$), i the intercombination line transition ($1s^2\,{}^1S_0$–$1s\,2p\,{}^3P_{1,2}$) and f the forbidden line transition ($1s^2\,{}^1S_0$–$1s\,2s\,{}^3S_1$) is not always reliable.

To interpret a spectrum one needs to establish the dominant physical process which led to its formation. A plasma can either be in ionisation equilibrium (IE), which applies to the majority of observed spectra, or in a non-equilibrium state or non-IE (NIE) (Liedahl, 1999). Both cases can again be split into two categories.

In equilibrium, the plasma can either be in collisional ionisation equilibrium (CIE), where electron-ion collisions are balanced by radiative recombination, or in photo-ionisation equilibrium (PIE), where an intense radiation field strips ions of their outer electrons, which are then recaptured via radiative recombination and cascade back into lower orbits (Kahn et al., 2002). The first is characteristic of a coronal plasma in thermal equilibrium, with million K high electron temperatures, while the second type is characterised by rather cool temperatures around 1000 K, but with a strong radiation field, and applies to accretion powered sources such as X-ray binaries and active galactic nuclei. Transient plasmas in NIE can either be dominated by ionisation (collisional or photo-), as observed in super-nova remnants (SNR), or by recombination (Liedahl, 1999). As time-scales in SNR are rather large, i.e., hundreds of years, such transient plasmas can easily be observed there.

The G-ratio of the He-like triplets is a good indicator about the plasma type. For G between 0.7 and 1.5, the plasma is usually in CIE, while G below 0.7 holds for an ionizing, and G above 1.5 for a recombining plasma (Pradhan, 1985). A large G-ratio arises because recombining electrons (from direct recombination and radiative cascades following recombination onto higher levels) mainly end up in the $^3S_1$ state (and, if the density is large enough, can from there be excited to the $^3P_{1,2}$ states) and to a much lesser extent in the resonant 2p $^1P_1$ state. In fact, while the $n = 2$ state is the predominant excited resonance line $^1P_1$ under collisions, electrons can recombine as likely to any other resonant level (3p, 4p, etc.), and therefore in a recombining plasma the r line is also suppressed when compared to higher n-states (Bautista & Kallman, 2000). In particular, an enhanced $1s^2\ ^1S_0$ – 1s 3p $^1P_1$ line compared to the r line is a further indicator of a recombining plasma. On the other hand, if the plasma is ionised, photoexcitation is occurring from the ground into the resonant $^1P_1$ state, which enhances the r line and decreases the G-ratio (also, electrons from the $^3S_1$ state (f) are photo-excited into the $^3P_{1,2}$ state (i), decreasing the R-ratio, independently from density conditions). The G-ratio is temperature dependent for any of the above scenarios, but the dependency is not the

same (Bautista & Kallman, 2000). Therefore, using the G-ratio as a temperature diagnostics tool, one needs to first establish the type of plasma observed. A further plasma type could also be a hybrid plasma, i.e., a superposition to different kinds of the above described plasmas, which makes G-ratio temperature diagnostics even trickier.

Solar and stellar flares are transient phenomena on rather short time-scales, few seconds for the ionisation phase, and tens of minutes for the cooling phase. The ionisation phase is given by a strong increase in temperature caused by reconnection of magnetic field lines, which unleashes a shock through the flare site, releasing non-thermal hard X-ray, γ-ray, ultra-violet and radio radiation, and seen in soft X rays in the rise phase of a flare light curve, while the cooling phase is given by the gradual, long decay of the soft X-ray light curve.

We present the X-ray spectrum of EV Lac extracted during the entire flaring phase of several flares, and compare it to the quiescent plasma. While the quiescent plasma is in CIE, we argue that the flaring plasma shows the characteristics of a recombining plasma in NIE. The dMe star EV Lac as well as the *Chandra* data extraction were already described in Sect. 5.3, and will not be repeated here.

6.3 Results and discussion

The here presented active and quiescent spectra are the same ones used in Chapter 5 and referred to as manually selected spectra. The quiescent one was extracted from the blue part of the observation (accumulated over 60.6 ks), as indicated in the light curve of Fig. 5.1 (top panel), while the active one was assimilated from the flaring part shown in black (accumulated over 39.1 ks). The flaring spectrum is defined as the difference between active and quiescent spectrum, as we assume that the flaring emission is superimposed on the quiescent one, and not replacing it. The total fluxes in the quiescent as well as the flaring spectrum are comparable and are listed in Table 6.1.

Table 6.1: *Chandra* HETG fluxes of EV Lac during quiescence and flares

Instrument	Wavelength Range (Å)	Quiescent Flux (10^{28} erg s^{-1})	Flaring Flux (10^{28} erg s^{-1})
MEG	2.5–26.0	2.8	3.1
MEG	1.7–17.5	1.9	2.5
HEG	1.7–17.5	2.0	2.6

Spectra from both the *Chandra* High-Energy Transmission Grating Spectrometer (HETG or HETGS) High-Energy Grating (HEG) arm, with a spectral range from 1.2–15 Å and a resolution of 0.012 Å (FWHM), as well as from the Medium-Energy Grating (MEG) arm with a spectral range of 2.5–26 Å and a resolution of 0.023 Å (FWHM) were extracted.

Figures 6.1–6.9 show the *Chandra* HETG-MEG and HETG-HEG spectra of EV Lac. The quiescent spectrum is given by the light blue line, the active spectrum by the black dotted line, and the pure flaring spectrum (active minus quiescent) by the solid dark red line. The largest 1σ error within each panel is plotted in one of the upper corners, and the errors roughly scale with the flux. For illustration purposes, the spectrum was smoothed by a factor of 5, matching the instrumental resolution of 0.023 Å for MEG and 0.012 Å for HEG. Three different flux scales (with units 10^{-12} erg cm^{-2} s^{-1} Å^{-1}) are used to present the figures. The flux range of the first three figures (Figs 6.1–6.3) goes from 0 to 40 and displays nicely the most pronounced changes; medium resolution can best be seen in Figs 6.4–6.6 with a flux range from 0 to 10; and the last three figures (Figs 6.7–6.9) with a flux range from 0 to 3 display the most details. For wavelength ranges where there are MEG as well as HEG data, the corresponding two spectral plots are shown in the same figure, with MEG in the top and HEG in the bottom panel (Figs 6.1–6.2, 6.4–6.5, and 6.7–6.8). We note that both the MEG and HEG spectra are in good agreement. Here, the spectra are discussed qualitatively. Fitting spectral models to derive elemental abundances, differential emission measures etc. are left to the future.

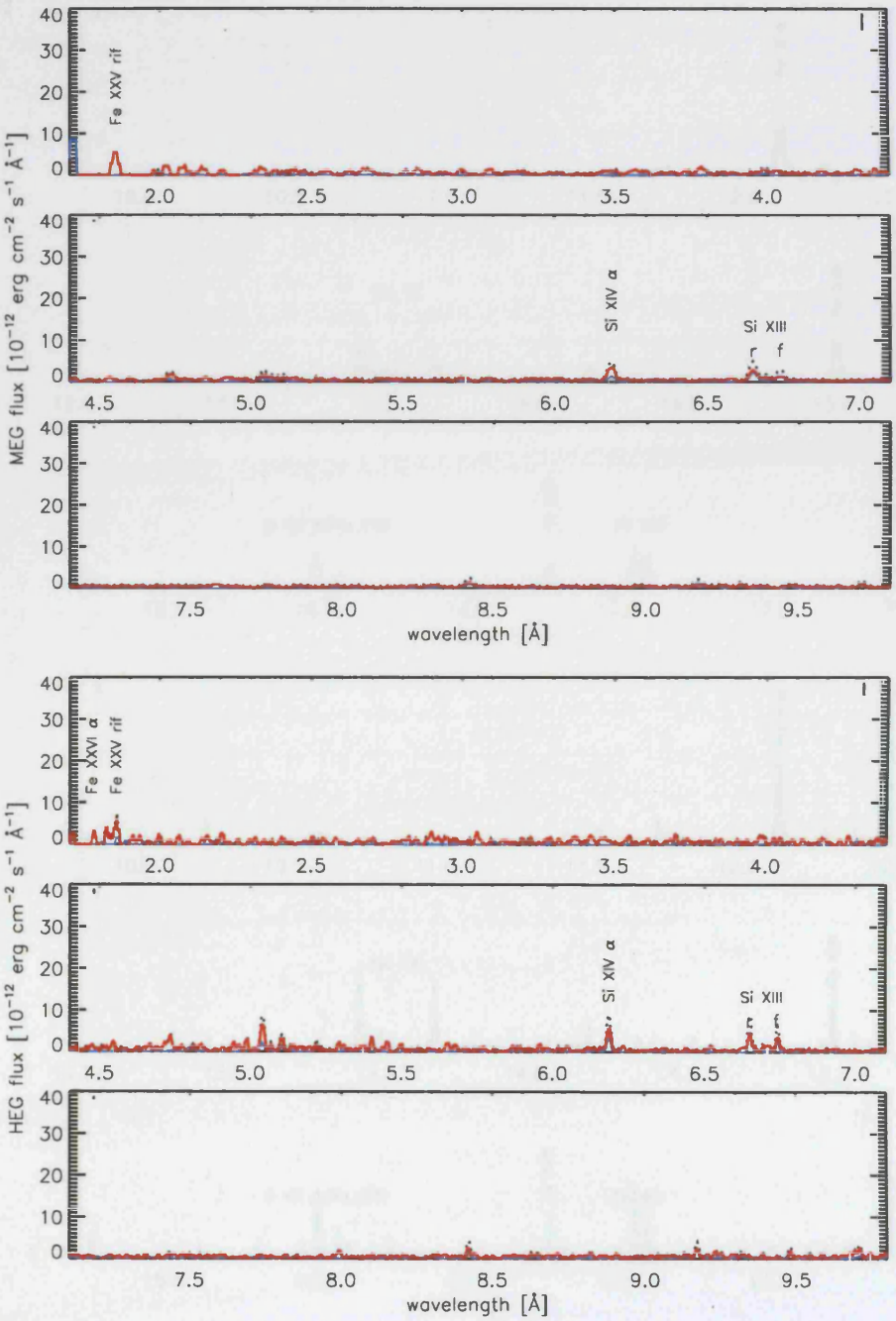

Figure 6.1: The *Chandra* MEG (top) and HEG (bottom) spectra between 1.7 and 9.8 Å of flaring (red) and quiescent (blue) states of EV Lac – strongest lines.

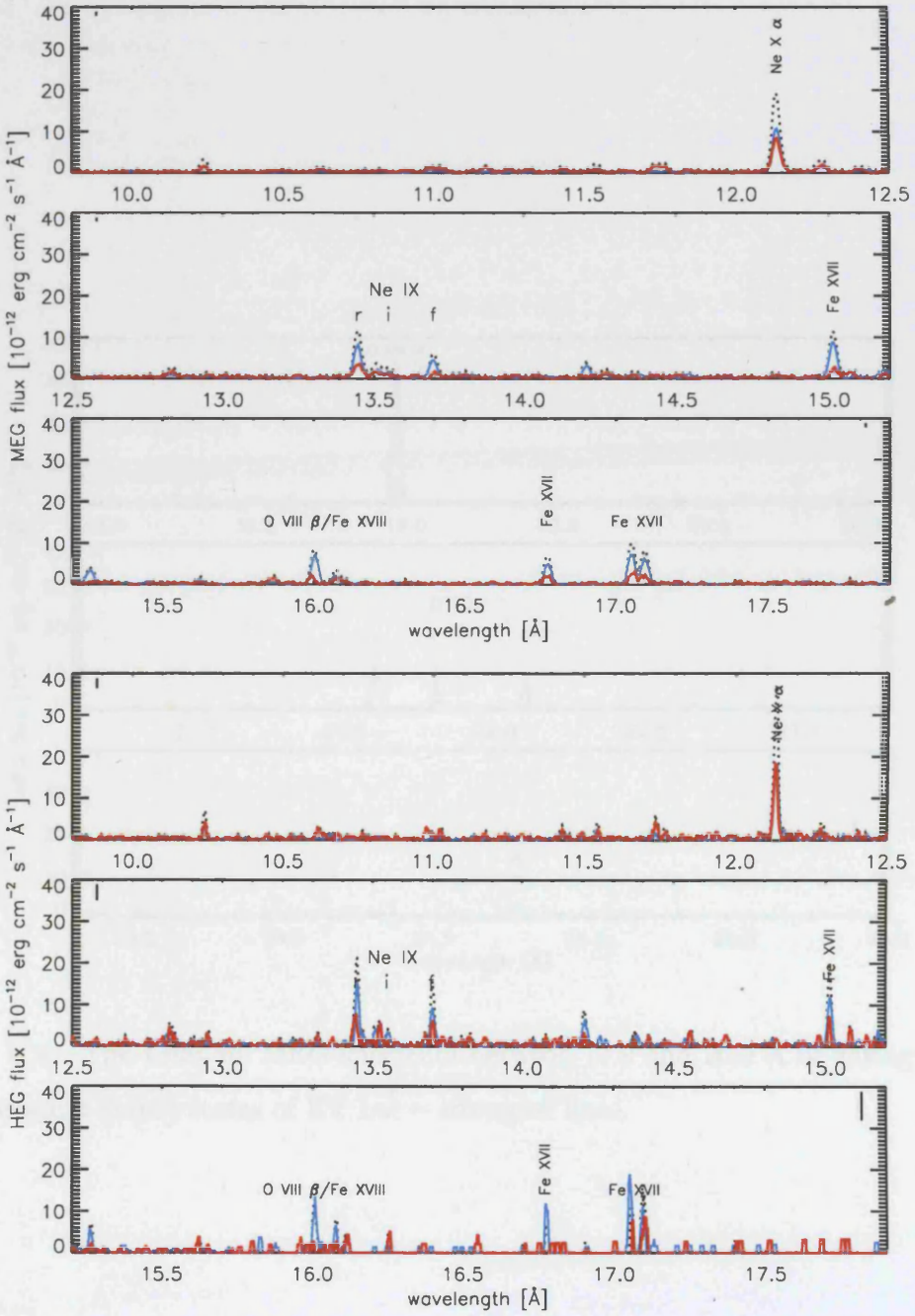

Figure 6.2: The *Chandra* MEG (top) and HEG (bottom) spectra between 9.8 and 17.9 Å of flaring (red) and quiescent (blue) states of EV Lac – strongest lines.

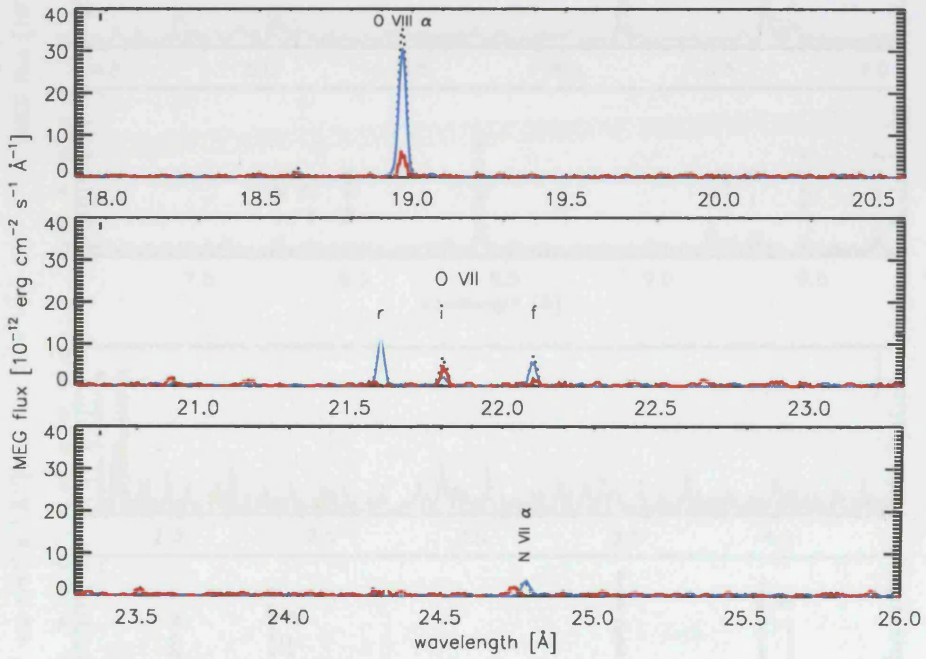

Figure 6.3: The *Chandra* MEG spectrum between 17.9 and 26.0 Å of flaring (red) and quiescent (blue) states of EV Lac – strongest lines.

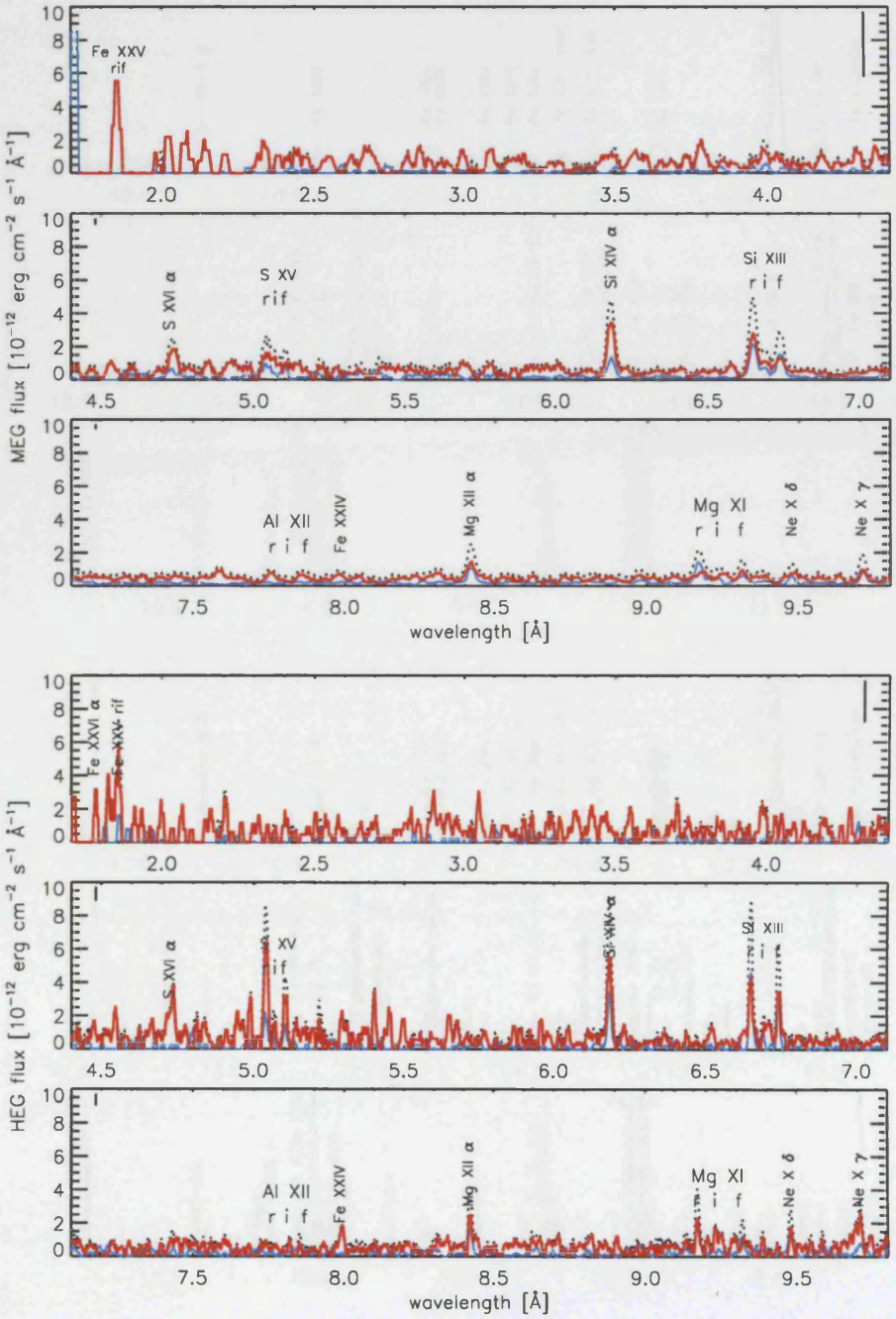

Figure 6.4: The *Chandra* MEG (top) and HEG (bottom) spectra between 1.7 and 9.8 Å of flaring (red) and quiescent (blue) states of EV Lac – medium zoom.

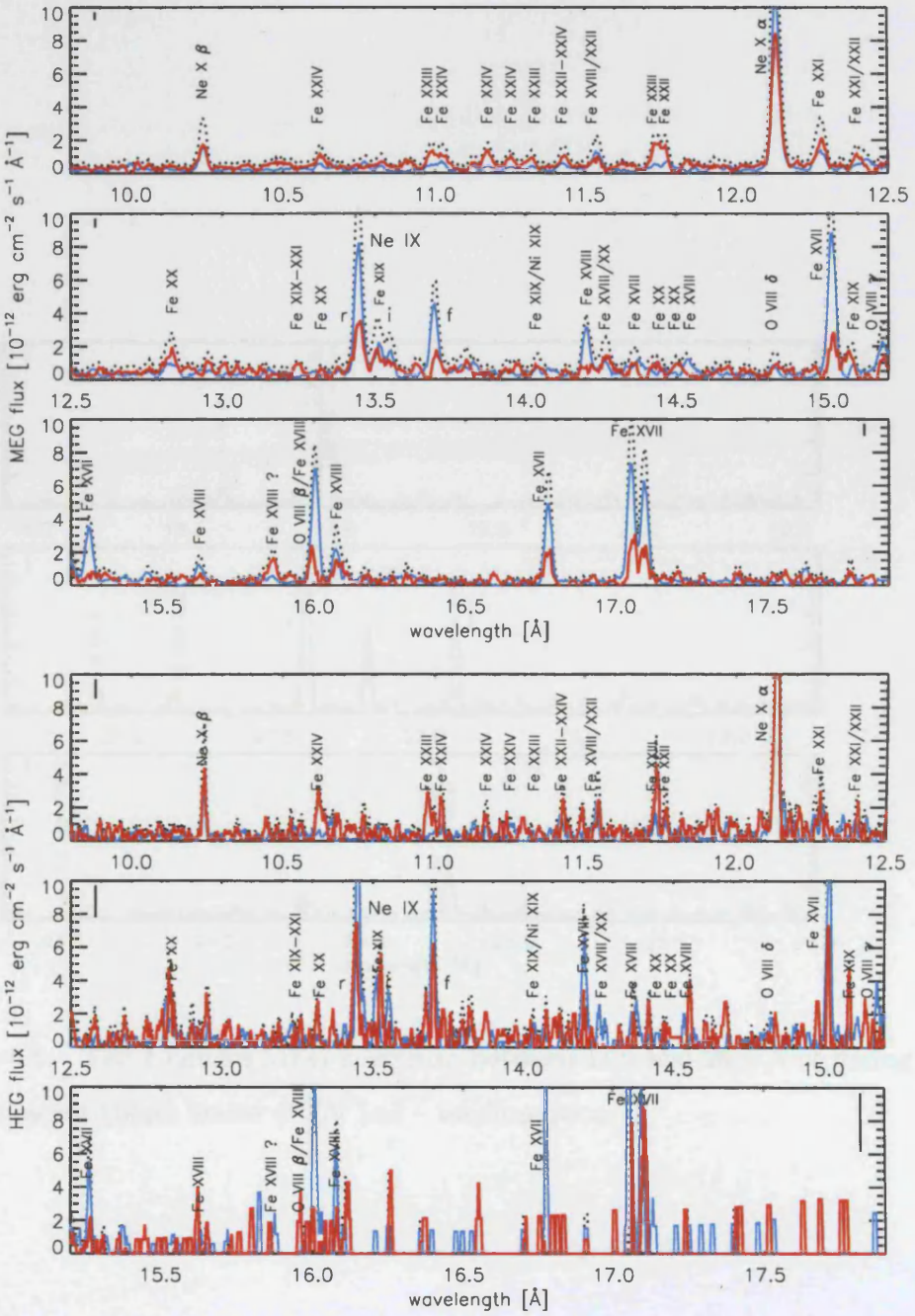

Figure 6.5: The *Chandra* MEG (top) and HEG (bottom) spectra between 9.8 and 17.9 Å of flaring (red) and quiescent (blue) states of EV Lac – medium zoom.

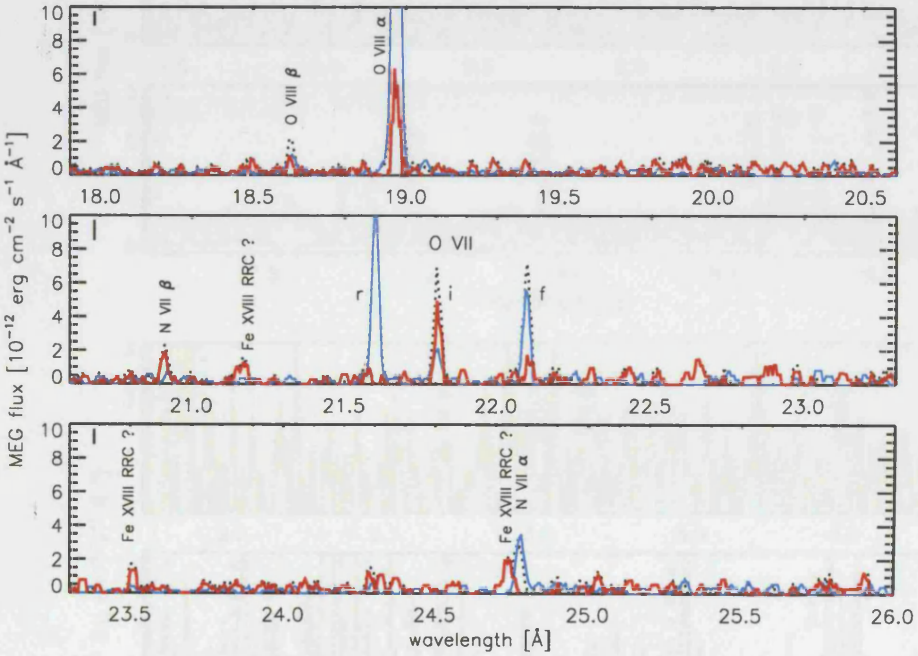

Figure 6.6: The *Chandra* MEG spectrum between 17.9 and 26.0 Å of flaring (red) and quiescent (blue) states of EV Lac – medium zoom.

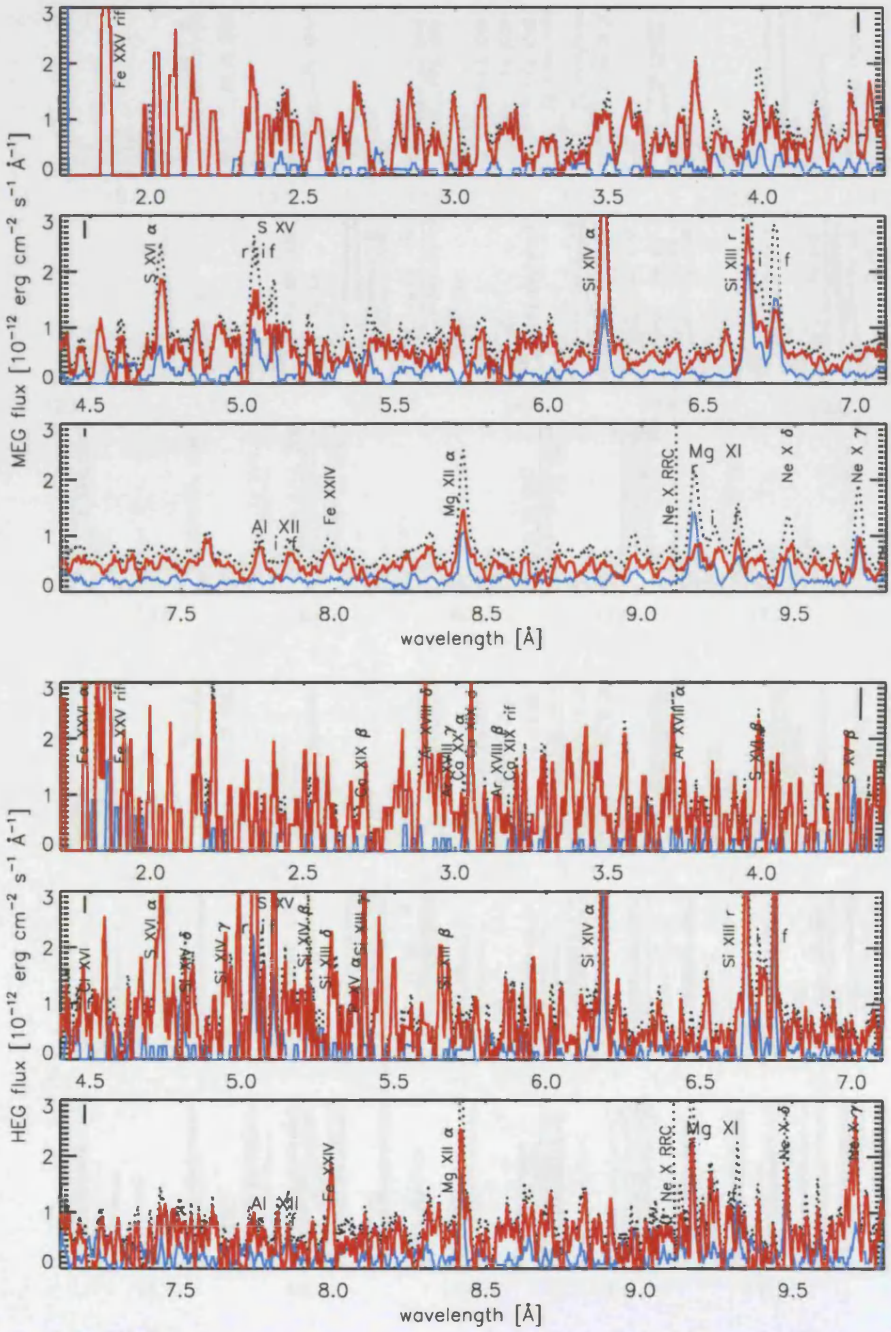

Figure 6.7: The *Chandra* MEG (top) and HEG (bottom) spectra between 1.7 and 9.8 Å of flaring (red) and quiescent (blue) states of EV Lac – details.

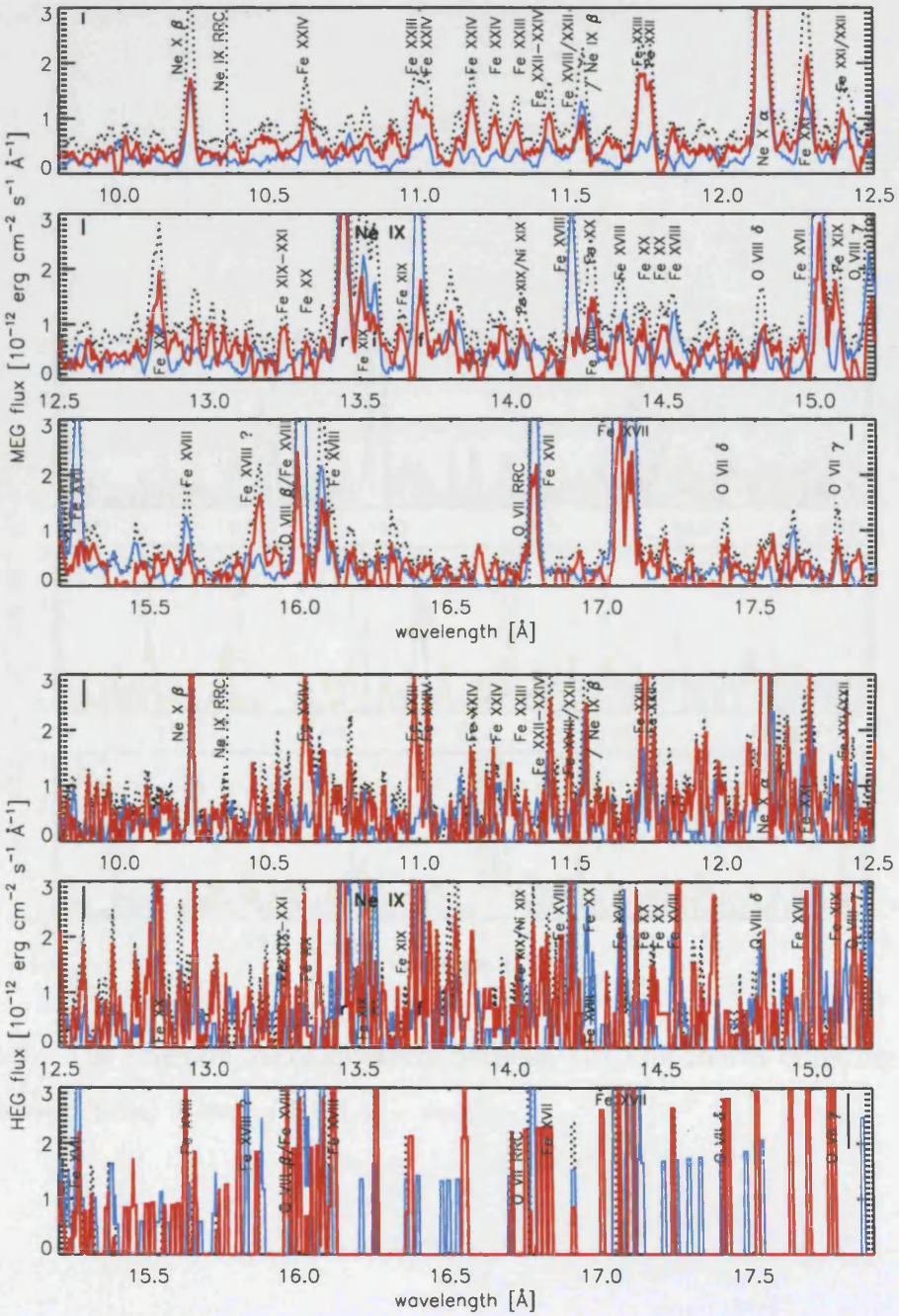

Figure 6.8: The *Chandra* MEG (top) and HEG (bottom) spectra between 9.8 and 17.9 Å of flaring (red) and quiescent (blue) states of EV Lac – details.

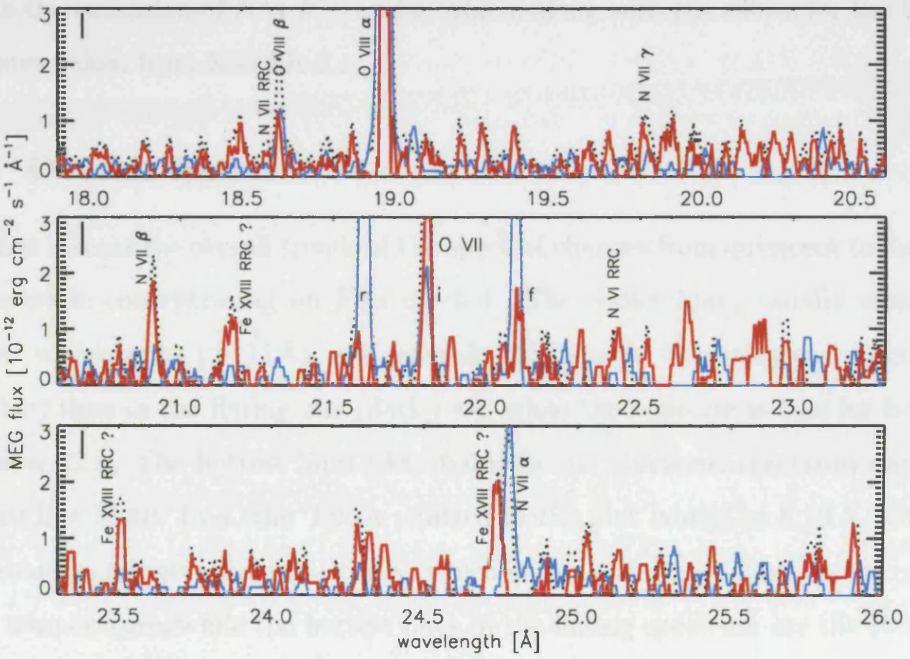

Figure 6.9: The *Chandra* MEG spectrum between 17.9 and 26.0 Å of flaring (red) and quiescent (blue) states of EV Lac – details.

6.3.1 Spectral lines

We discuss all prominent lines in the spectra, with special focus on the resonant transition lines of H-like ($np\,^2P_{1/2} \rightarrow 1s\,^2S_{1/2}$, Lyman series), and He-like ($1s\,np\,^1P_1 \rightarrow 1s^2\,^1S_0$) ions (with n=2,3,4,...), some Fe L-shell transitions, and the intercombination ($1s\,2p\,^3P_{1,2} \rightarrow 1s^2\,^1S_0$) and forbidden ($1s\,2s\,^3S_1 \rightarrow 1s^2\,^1S_0$) transitions of He-like ions. We also check for radiative recombination continua (RRC) to either rule out or confirm photoionisation. Displayed line transition values were taken from CHIANTI 5.1, with the exception of N VI β, γ and δ, which, along with the values for the RRC edges, were taken from XSTAR 2.1.

6.3.2 Overall trends

Let us first discuss the overall trends of the spectral changes from quiescent to flaring emission while concentrating on Figs 6.1–6.3. The cooler lines, usually situated at longer wavelengths (> 12 Å), are generally stronger in the quiescent spectrum (light blue) than in the flaring one (dark red), while the opposite is true for hotter lines below 12 Å. The hottest lines identifiable in the quiescent spectrum are the resonance line Si XIV Lyα (the 'Ly' is omitted in the plot labels) at 6.19 Å, with a peak formation temperature of ~16 MK, which gives us an upper limit on the quiet coronal temperature, while the hottest lines in the flaring spectrum are the Fe XXV with a temperature of ~63 MK, the (unresolved) He-like triplet being at 1.85–1.86 Å, and possibly even the Fe XXVI resonance line (λ1.78) at 100 MK, which is visible in the HEG spectrum.

The strongest line in the quiescent spectrum is O VIII Lyα (λ18.97, $T_{\rm peak}$ = 13 MK), while in the flaring spectrum this line is strongly reduced, with now Ne X Lyα (λ12.13, 13 MK) being the strongest line, which has the same flux as during quiescence.

It is not clear whether a continuum exists at all or not. In the MEG spectrum, the X-ray spectrum seems to be elevated between ca. 6 and 12 Å, more so in the

flaring than in the quiescent phase, while in the same range in the HEG spectrum, this does not seem to be the case, as the flux level approaches zero now and again. Therefore, the MEG elevations seems more like a pseudo-continuum, consisting of unresolved lines.

6.3.3 The He-like transitions

An increase in the i line, such that f/i is decreased, is indicative of a density increase, while a relative decrease of the r line compared to f and i suggests a recombination plasma. Another indicator of a recombination plasma is the He-like $r\beta/r\alpha$ ratio ($1s^2\,{}^1S_0$ - $1s3p\,{}^1P_1$)/($1s^2\,{}^1S_0$ - $1s2p\,{}^1P_1$). This ratio increases for similar reasons like the G-ratio, namely because the $1s2p\,{}^1P_1$ is populated by recombinations to a relatively lesser extent than the $1s3p\,{}^1P_1$ state (Bautista & Kallman, 2000), or, differently expressed, a recombining electron has no preference into which $1s\,n\,p\,{}^1P_1$ state to recombine, while for excitation it is much more likely to make the resonant transition with the lowest energy.

The O VII lines show a strong recombination signature. While the quiescent spectral lines show normal CIE behaviour, the r line is practically reduced to zero in the flaring phase, while the O VII β line flux remains the same, thus relatively increasing compared to the much reduced r flux, indicative of a recombining plasma. Earlier, we have ruled out resonance scattering as a cause for the reduced r-line flux, by independent comparison of Fe XVII (λ15.01, λ15.26, and λ16.78) line ratios (Sect. 5.5.2). Additionally, as was already investigated in Chapter 5, the i line shows a strong enhancement, while the f line has decreased, so that $R < 1$ which implies a high density.

Does the possible recombination last long enough to be observed? Table 6.2 displays the calculated equilibration timescales for collisional ionisation ($\tau_{\rm ion}$) and radiative recombination ($\tau_{\rm rec}$) using the rate coefficients given by Mewe et al. (1985)

Table 6.2: Collisional ionisation and recombination equilibration timescales τ

		O VII r	O VII i	O VII f
$T_e = 100\,\mathrm{MK}$	τ_{ion} [s]	0.02	2.6	11
$n_e = 30 \cdot 10^{10}\,\mathrm{cm}^{-3}$	τ_{rec} [s]	1470	240	150
$T_e = 100\,\mathrm{MK}$	τ_{ion} [s]	0.07	7.9	34
$n_e = 10 \cdot 10^{10}\,\mathrm{cm}^{-3}$	τ_{rec} [s]	4420	720	460
$T_e = 100\,\mathrm{MK}$	τ_{ion} [s]	0.15	16	68
$n_e = 5 \cdot 10^{10}\,\mathrm{cm}^{-3}$	τ_{rec} [s]	8850	1440	920
$T_e = 10\,\mathrm{MK}$	τ_{ion} [s]	0.04	0.28	1.3
$n_e = 30 \cdot 10^{10}\,\mathrm{cm}^{-3}$	τ_{rec} [s]	200	37	44
$T_e = 10\,\mathrm{MK}$	τ_{ion} [s]	0.11	0.84	3.9
$n_e = 10 \cdot 10^{10}\,\mathrm{cm}^{-3}$	τ_{rec} [s]	600	110	130
$T_e = 10\,\mathrm{MK}$	τ_{ion} [s]	0.22	1.7	7.9
$n_e = 5 \cdot 10^{10}\,\mathrm{cm}^{-3}$	τ_{rec} [s]	1190	220	270
$T_e = 4\,\mathrm{MK}$	τ_{ion} [s]	0.10	0.31	1.5
$n_e = 30 \cdot 10^{10}\,\mathrm{cm}^{-3}$	τ_{rec} [s]	90	18	27
$T_e = 4\,\mathrm{MK}$	τ_{ion} [s]	0.29	0.94	4.6
$n_e = 10 \cdot 10^{10}\,\mathrm{cm}^{-3}$	τ_{rec} [s]	270	53	81
$T_e = 4\,\mathrm{MK}$	τ_{ion} [s]	0.59	1.9	9.2
$n_e = 5 \cdot 10^{10}\,\mathrm{cm}^{-3}$	τ_{rec} [s]	540	110	160

(which are also used by CHIANTI) for the O VII r, i and f lines at different temperatures and densities. If the equilibration times are small compared to flare rise and decay times, respectively, then the plasma can be treated in thermal equilibrium. This is indeed so for the ionisation timescale $\tau_{\rm ion}$, which is in all tabulated cases much smaller than the typical flare rise time of a few minutes. However, the recombination equilibration time $\tau_{\rm rec}$ for the r line is several thousands of seconds for 100 MK high temperatures, which is in the same order of or even larger than the flare decay time. The observed 100 MK flare temperature of EV Lac strongly supports the NIE interpretation of the flare spectrum. Thus it is possible to observe a transient recombining flare plasma which is not in thermal equilibrium.

The **Ne** IX lines are consistent with a coronal plasma, though recombination cannot be ruled out completely. The He-like triplet line flux is reduced in all the three lines during the flaring phase, implying less emission at the formation temperature of Ne IX, with the i line even completely disappeared, possibly because of a low overall flux and not necessarily because of lower density. Here, the β line is of no help, as this line is blended with Fe XVIII (possibly decreased flux during flares) and Fe XXII (possibly increased flare flux).

Mg XI shows decreased r flux and increased i and f flux during the flares, which suggests recombination and higher density (i only appeared in the flaring spectrum). **Al** XII is weak (probably low abundance), but the r and f lines are appearing in the flaring spectrum (from zero in quiescence). The **Si** XIII r and i line fluxes increase, whereas f slightly decreases, indicating higher density. Si XIII β also appears, hinting at recombination. **S** XV rif and **Fe** XXV rif are present but not well resolved.

6.3.4 The H-like Lyman-series

Relative increase of higher Lyman (Ly) transitions (β, γ, δ, ...) as compared to Lyα are indicative of a recombining plasma for the same reasons as the He-like resonant line transitions. **O** VIII Lyα is strongly reduced during flaring, while Lyβ

is reduced also but relatively less (it is unfortunately blended with Fe XVIII, which is also expected to be reduced), and Lyγ and Lyδ are even less reduced, hinting at recombination. **Ne X** Lyα is a little reduced, while Lyβ remains its flux, and so do Lyγ and Lyδ, which could be a recombination signature. The remaining H-like transitions, which are all below 9.5 Å, are rather messy because of the line jungle at low wavelengths. Mg XII Lyα seems to retain its flux, while Si XIV, S XV, Ca XVX and Fe XXVI all appear because of the enhanced temperature from the flare.

The Lyα line of **N VII** is blue-shifted and less intense in the flaring plasma, while Lyβ and Lyγ of N VII also appear to be blue-shifted but with increased intensity, which would be indicative of a recombining, up-flowing plasma.

6.3.5 Photoionisation?

A last question remains. Was the recombining plasma excited by collisions or by photoionisation? If there were a strong radiation field, the r lines of the He-like triplets would not be so much suppressed, because photoexcitation would enhance this level. Another way to check is to look for radiative recombination continua (RRC). The broadness of the RRC is proportional to $k_B T_e$, with k_B the Boltzmann constant and T_e the electron temperature (Kahn et al., 2002). For photoionised plasma, the $k_B T_e \ll 1$ is small and therefore the RRC has a large peak, while for collisionally ionised plasma $k_B T_e \approx 1$ and the RRC is small and buried in the spectral background.

Can any RRC be identified? The O VII RRC edge lies at 16.76 Å. Unfortunately, in the MEG spectrum this edge is still within the blue wing of the Fe XVII (λ16.78) line, and in the HEG spectrum the effective area above 16 Å is too small to see anything. Nevertheless, in the blown-up spectrum of that region (Fig. 6.10) it can be seen that the Fe XVII line is much lower during the flaring phase, while the flare emission in the O VII RRC region exceeds the quiescent emission. However, this excess emission is very weak, and comparing the broadness of this line with Figure 1

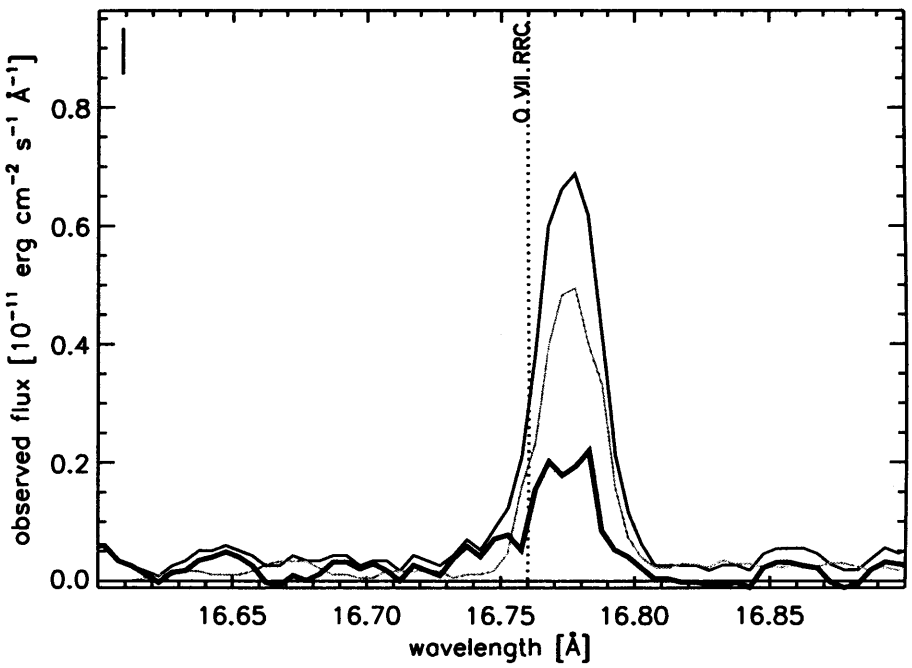

Figure 6.10: The O VII RRC edge blended by the Fe XVII line.

in Kahn et al. (2002) gives an electron temperature estimate of 15 MK, which is about the coronal flare temperature and therefore not caused by any radiation field. All RRCs of ions at shorter wavelengths are, if at all visible, extremely small, and often blended with stronger emission lines.

The RRC for N VI (λ22.4) and for N VII (λ18.6), however, seem to be recognisable, but very weakly (Fig. 6.9). In the same wavelength regime, there are also two unidentified lines in the flaring spectrum, which could be Fe XVIII RRC (λ21.2 and λ23.5). If this is indeed so, then the blue-shifted N VII lines in the flaring spectrum would have been formed by photoionisation. This could possibly have been caused by a strong UV radiation field which was generated by the flare lower down in the atmosphere. The cooler nitrogen would then be heated and ionised by the photons, and in turn flow up-wards. Thus, if this picture holds (given the relatively weak N lines and relatively large error margins), we are observing chromospheric evaporation into the corona.

6.4 Conclusions

The temperature derived from the G-ratio is inconsistent with the one derived from the O VII r/O VIII Lyα ratio, the latter being the more believable one, as it does not change from quiescence to active state, while the G-ratio temperature is lower in the active phase, which is counterintuitive. In recent years, many researchers have encountered inconsistencies with the G-ratio in the stellar coronal context. From the Fe XVII line ratios we rule out resonance scattering as an explanation. We argue qualitatively that the flaring plasma is no longer in thermal equilibrium, but that it is a recombining plasma, and therefore the temperature dependence of the G-ratio is changed. This picture is additionally supported by the relative increase of the resonance β line compared to the α one. Such conditions are so far better known in the context of, e.g., supernova shock waves (Pradhan, 1985) or accretion-powered sources (Kahn et al., 2002), where the plasma is ionised by the strong

photon radiation field and therefore constantly recombining. In stellar flares, the plasma is likely to be predominantly ionised by high-energy collisions between ions and electrons arising from shocks caused by the flare (Liedahl, 1999). In extreme cases photoionisation caused by a strong ultra-violet radiation field, which can be produced by the flare itself, may also play a role, as perhaps for the N VI-VII lines, a view which is supported by recent radiative hydrodynamic models of M dwarf flares (Allred et al., 2006). Additionally, a blue-shift is observed in the N VII lines, suggesting cooler material evaporates from the chromosphere into the corona. After an initial rapid ionisation due to the sudden appearance of hot temperatures, the plasma recombines, which happens during the gradual phase of the flare. This is what we observe in the accumulated flaring spectrum. The expectation would be that with better resolution and/or for a huge flare, the spectrum from the increasing phase of the flare would show an ionizing plasma, which has other characteristic distinctions, e.g. an enhanced resonance α line.

Chapter 7

Conclusions and outlook

7.1 Conclusions

In this thesis, I have investigated several flares on seven dMe-type stars. The findings are consistent with the standard flare model of magnetic reconnection, followed by particle acceleration, which leads to the production of a strong UV radiation field, plasma heating, chromospheric evaporation, increased plasma density in the corona, and transient non-ionisation equilibrium plasma conditions dominated by radiative recombinations.

There is a good correlation between flare emission from the UV and the soft X-ray regimes. Simultaneous UV and X-ray observations of flare stars by *XMM-Newton* show that for every larger X-ray flare there is a corresponding UV flare and vice versa. The UV flares typically precede the X-ray flares by around 10 minutes, which approximately coincides with the soft X-ray flare rise time. The flares follow power-law relationships (i) between UV and X-ray flare energy, (ii) between UV and X-ray peak luminosity increase, and (iii) between UV energy and X-ray peak luminosity increase. There is no good power-law correlation between UV peak luminosity increase and X-ray energy, which has been used as a control relationship, but was not expected to show a correlation other than the "Big Flare

Syndrome" (e.g., all quantities correlate for big flares). The first two relationships show that the underlying physics is the same for all the observed flares. The third relationship is consistent with the Neupert effect, which states that processes leading to non-thermal emissions, here the UV, are directly responsible for the heating of the plasma, which in turn radiates in soft X rays. This was the first time where UV versus X-ray scaling laws were investigated and correlations found between flares from different stars.

For one particular flare characterised by a damped oscillation (in intensity) during its flat-top phase, loop length and magnetic field strength could be estimated using its oscillation. The derived loop length of around 250 Mm is comparable to a large solar post-flare loop, while rather large compared to the star itself (about the length of the stellar radius). The coronal magnetic field strength of around 100 G was also found to be on the larger side of solar coronal values. It is, however, what can be expected from a star which has a larger X-ray activity than the Sun at solar maximum.

This was the first ever X-ray oscillation observed during a stellar flare. Between the two competing hypotheses of the cause for the observed oscillation, post-flare loop oscillation versus repeated flaring, the former is perhaps more supported. The supporting factors for the loop oscillation are that the oscillation has a smooth exponential decay and a regular oscillation frequency, both of which are difficult to explain with random repeated flaring. In Chapter 3 we also found a possible UV deficiency (or X-ray excess) in this flare.

The coronal electron density is enhanced during flares, as seen here in a significant increase of the O VII intercombination line, and UV radiation is found to correlate with X rays over many different-sized flares, consistent with the Neupert effect. Some cooler ions in the long wavelength X-ray regime may be photoionised by such a UV radiation field, as line ratios of N VII and appearing radiative recombination continua suggest, thus heating the lower-lying plasma, which then evaporates upwards, as seen in possible blue-shifts of the same lines. The overall flare plasma is no longer in

collisional ionisation equilibrium, but shows the characteristics of a cooling plasma in non-ionisation equilibrium.

The non-ionisation equilibrium observed in the EV Lac flares can be observed because the equilibration time for the recombining plasma can reach several thousands of seconds, which is in the order of the flare decay and long enough to be observed. The equilibration time can be this high because of the very high temperatures occurring during the flares. The appearance of the Fe XXVI line in the *Chandra* HEG spectrum during flares is indicative of flare temperatures of up to 100 MK. Thus, the flare plasma may be rapidly heated by a large initial shock, highly ionizing even the heavy elements such as iron, and stripping the less heavy elements like oxygen completely of their electrons. After the shock, this hot flare plasma, which is tied to the flare loop, then starts to rapidly cool, as the hot flare loop (tens to a hundred MK) is embedded in the cooler coronal surrounding (several MK only). The highly ionised ions recapture their electrons and recombine. This radiative cooling signature is especially clear in the O VII lines with the repressed r line.

The observed flares on the dMe stars are all small to medium sized ones, compared to the occasional huge flares seen on these stars and described in the literature. Compared with solar flares, however, the observed flares are large, comparable in size and energy to large solar flares. Comparing these flares to the relative size of the star, the flares are huge, having loop structures similar in size to the stellar radius. On the Sun, this happens only for extreme cases like for equatorial loops connecting the northern with the southern hemisphere, or magnetic loops ranging from one active region to another one. As the dMe stars are likely to be covered entirely in active regions, the magnetic carpet and overlying coronal loop structures are much more entangled and extended than on the Sun, the entanglement leading to more frequent reconnection and flares, the extension to larger flares sizes. This very strongly supports that these stars have stronger and more active magnetic fields, which is likely to be linked to the large convection zones (in relative as well as absolute terms) which these stars have, and the resulting magnetic-field generation

by an efficient convective dynamo. The flare mechanisms, on the other hand, are similar to solar flares: reconnection, particle acceleration, chromospheric heating, chromospheric evaporation, temperature and density enhancements.

Thus, I conclude that flares on dMe stars are caused by the same mechanisms which also trigger solar flares, namely reconnection of the rearranging magnetic field lines, and that their signatures are similar too, except that some features can be explored from a slightly different angle, as the situation on these stars can be more extreme than on the Sun. In particular, UV or WL flares can better be studied on the, in this wavelength regime, less luminous M-type stars, and high-energy X-ray related phenomena can be even more energetic than on the Sun.

7.2 Outlook

An imminent future project would be to find other cases of transient radiative recombining plasmas caused by a collisional, high-temperature shock wave, which could be observed during the gradual decaying phase of a soft X-ray flare. The preceding transient collisional ionizing plasma, which occurs during the rising phase of a soft X-ray flare, has already been observed for solar flares, but would be much more challenging to see in stellar flares. To my knowledge, neither detailed theoretical calculations or numerical models, nor other observational examples are available to date which deal with a cooling plasma during flare decay, although they were anticipated. It would be a worthwhile project to model this observed flaring plasma of EV Lac.

It would be very interesting to measure for a wide range of flares how UV correlates with density or pressure, a project which might only become feasible with the next generation of high-resolution X-ray spectrometers like *Xeus* or *Constellation-X*. Recent solar observations of flares triggering a surface wave (Kosovichev & Zharkova, 1998; Donea & Lindsey, 2005) suggest that only in certain conditions flare energy can be transferred all the way down to the photosphere. These surface waves caused

by flares are so far only seen during the declining phase of the 11-year solar cycle. They are observed in WL, and therefore they are always accompanied by a WL flare. But do WL flares always produce surface ripples? I speculate that they might, and that their radiation is actually produced on the photosphere (UV might be produced a bit higher up). They could be generated when the flare pressure is large enough, and only then, so that the pressure wave originating from the flare reconnection site can propagate all the way to the photosphere before being dissipated.

Global mode measurements on M-type stars will soon become available with the recently launched *COROT* satellite and other dedicated observatories to asteroseismology. Determining whether M-type stars actually do have a tachocline or whether they are fully convective, as well as measuring their interior rotation profile will shed light on the production mechanism of their strong magnetic fields.

Bibliography

Alekseev, I. Y. 2005, Spots, activity cycles, and differential rotation on cool stars, *Ap*, **48**, 20

Allred, J. C., Hawley, S. L., Abbett, W. P., & Carlsson, M. 2006, Radiative hydrodynamic models of optical and ultraviolet emission from M dwarf flares, *ApJ*, **644**, 484

Andrews, A. D. 1990, Investigation of micro-flaring and secular and quasi-periodic variations in dMe flare stars: VI. quasi-periodicities in Gliese 644 AB (V 1054 Oph) prior to a large X-ray flare, *A&A*, **239**, 235

Antonucci, E., Gabriel, A. H., & Dennis, B. R. 1984, The energetics of chromospheric evaporation in solar flares, *ApJ*, **287**, 917

Arzner, K. & Güdel, M. 2004, Are coronae of magnetically active stars heated by flares? III. analytical distribution of superposed flares, *ApJ*, **602**, 363

Aschwanden, M. J., Fletcher, L., Schrijver, C. J., & Alexander, D. 1999, Coronal loop oscillations observed with the Transition Region and Coronal Explorer, *ApJ*, **520**, 880

Audard, M., Güdel, M., & Guinan, E. F. 1999, IMPLICATIONS FROM EXTREME-ULTRAVIOLET OBSERVATIONS FOR CORONAL HEATING OF ACTIVE STARS, *ApJ*, **513**, L53

Audard, M., Güdel, M., & Skinner, S. L. 2003, SEPARATING THE X-RAY EMISSIONS OF UV CETI A AND B WITH CHANDRA, *ApJ*, **589**, 983

Ayres, T. R., Brown, A., Osten, R. A., et al. 2001, CHANDRA, EUVE, HST, AND VLA MULTIWAVELENGTH CAMPAIGN ON HR 1099: INSTRUMENTAL CAPABILITIES, DATA REDUCTION, AND INITIAL RESULTS, *ApJ*, **549**, 554

Ayres, T. R., Fleming, T. A., Simon, T., et al. 1995, THE RIASS CORONATHON: JOINT X-RAY AND ULTRAVIOLET OBSERVATIONS OF NORMAL F-K STARS, *ApJS*, **96**, 223

Barrado y Navascués, D., Stauffer, J. R., Song, I., & Caillault, J.-P. 1999, THE AGE OF BETA PICTORIS, *ApJ*, **520**, L123

Bautista, M. A. & Kallman, T. R. 2000, RECOMBINATION SPECTRA OF HELIUM-LIKE IONS, *ApJ*, **544**, 581

Cargill, P. J., Mariska, J. T., & Antiochos, S. K. 1995, COOLING OF SOLAR FLARE PLASMAS. I. THEORETICAL CONSIDERATIONS, *ApJ*, **439**, 1034

Catura, R. C., Acton, L. W., & Johnson, H. M. 1975, EVIDENCE FOR X-RAY EMISSION FROM CAPELLA, *ApJ*, **196**, L47

Chabrier, G. & Baraffe, I. 1997, STRUCTURE AND EVOLUTION OF LOW-MASS STARS, *A&A*, **327**, 1039

Chabrier, G. & Küker, M. 2006, LARGE-SCALE α^2-DYNAMO IN LOW-MASS STARS AND BROWN DWARFS, *A&A*, **446**, 1027

Chen, C. H., Patten, B. M., Werner, M. W., et al. 2005, A SPITZER STUDY OF DUSTY DISKS AROUND NEARBY, YOUNG STARS, *ApJ*, **634**, L189

Cincunegui, C., Díaz, R. F., & Mauas, P. J. D. 2007, A POSSIBLE ACTIVITY CYCLE IN PROXIMA CENTAURI, *A&A*, **461**, 1107

Delfosse, X., Forveille, T., Ségransan, D., et al. 2000, ACCURATE MASSES OF VERY LOW MASS STARS IV. IMPROVED MASS-LUMINOSITY RELATIONS, *A&A*, **364**, 217

den Herder, J. W., Brinkman, A. C., Kahn, S. M., et al. 2001, THE REFLECTION GRATING SPECTROMETER ON BOARD XMM-NEWTON, *A&A*, **365**, L7

Dennis, B. R. & Zarro, D. M. 1993, THE NEUPERT EFFECT: WHAT CAN IT TELL US ABOUT THE IMPULSIVE AND GRADUAL PHASES OF SOLAR FLARES?, *Sol. Phys.*, **146**, 177

Dere, K. P., Landi, E., Mason, H. E., Fossi, B. C. M., & Young, P. R. 1997, CHIANTI - AN ATOMIC DATABASE FOR EMISSION LINES, *A&AS*, **125**, 149

Donea, A.-C. & Lindsey, C. 2005, SEISMIC EMISSION FROM THE SOLAR FLARES OF 2003 OCTOBER 28 AND 29, *ApJ*, **630**, 1168

Doschek, G. A., Feldman, U., Landecker, P. B., & McKenzie, D. L. 1981, HIGH RESOLUTION SOLAR FLARE X-RAY SPECTRA - THE TEMPORAL BEHAVIOR OF ELECTRON DENSITY, TEMPERATURE, AND EMISSION MEASURE FOR TWO CLASS M FLARES, *ApJ.* **249**, 372

Doyle, J. G. 1987, AN ACTIVITY-ROTATION RELATIONSHIP IN F-M DWARFS FROM MG II H AND K FLUX, *MNRAS*, **224**, 1

Drake, J. J., Stern, R. A., Stringfellow, G. S., et al. 1996, DETECTION OF QUIESCENT EXTREME-ULTRAVIOLET EMISSION FROM THE VERY LOW MASS DWARF VAN BIESBROECK 8: EVIDENCE FOR A TURBULENT FIELD DYNAMO, *ApJ*, **496**, 828

Fuhrmeister, B., Schmitt, J. H. M. M., & Wichmann, R. 2004, FE XIII CORONAL LINE EMISSION IN COOL M DWARFS, *A&A*, **417**, 701

Gabriel, A. H. & Jordan, C. 1969, INTERPRETATION OF SOLAR HELIUM-LIKE ION LINE INTENSITIES, *MNRAS*, **145**, 241

García-Alvarez, D., Jevremović, D., Doyle, J. G., & Butler, C. J. 2002, OBSERVATIONS AND MODELLING OF A LARGE OPTICAL FLARE ON AT MICROSCOPII, *A&A*, **383**, 548

Gliese, W. & Jahreiss, H. 1988, THE THIRD CATALOGUE OF NEARBY STARS WITH SPECIAL EMPHASIS ON WIDE BINARIES, *Ap&SS*, **142**, 49

Gliese, W. & Jahreiss, H. 1991, PRELIMINARY VERSION OF THE THIRD CATALOGUE OF NEARBY STARS, Astron. Rechen-Institut, Heidelberg

Gordon, K. C. & Kron, G. E. 1949, FLARE OF A DME STAR, BD+202465, OBSERVED PHOTOELECTRICALLY, *PASP*, **61**, 210

Gray, D. F. 1992, THE INFERRED COLOR INDEX OF THE SUN, *PASP*, **104**, 1035

Güdel, M. 2004, X-RAY ASTRONOMY OF STELLAR CORONAE, *A&A Rev.*, **12**, 71

Güdel, M., Audard, M., Kashyap, V. L., Drake, J. J., & Guinan, E. F. 2003, ARE CORONAE OF MAGNETICALLY ACTIVE STARS HEATED BY FLARES: II. EUV AND X-RAY FLARE STATISTICS AND THE DIFFERENTIAL EMISSION MEASURE DISTRIBUTION, *ApJ*, **582**, 423

Güdel, M., Audard, M., Reale, F., Skinner, S. L., & Linsky, J. L. 2004, FLARES FROM SMALL TO LARGE: X-RAY SPECTROSCOPY OF PROXIMA CENTAURI WITH *xmm newton*, *A&A*, **416**, 713

Güdel, M., Audard, M., Skinner, S. L., & Horvath, M. I. 2002, X-RAY EVIDENCE FOR FLARE DENSITY VARIATIONS AND CONTINUAL CHROMOSPHERIC EVAPORATION IN PROXIMA CENTAURI, *ApJ*, **580**, L73

Haisch, B. M., Butler, C. J., Foing, B., Rodonó, M., & Giampapa, M. S. 1990, ROTATIONAL MODULATION AND FLARES ON RS CANUM VENATICORUM AND

BY DRACONIS-TYPE STARS. XV - OBSERVATIONS OF PROXIMA CENTAURI AND SOLAR CALIBRATION DATA, *A&A*, **232**, 387

Handy, B. N., Acton, L. W., Kankelborg, C. C., et al. 1999, THE TRANSITION REGION AND CORONAL EXPLORER, *Sol. Phys.*, **187**, 229

Harrington, R. S. & Dahn, C. C. 1980, SUMMARY OF U.S. NAVAL OBSERVATORY PARALLAXES, *AJ*, **85**, 454

Hawley, S. L., Fisher, G. H., Simon, T., et al. 1995, SIMULTANEOUS EXTREME-ULTRAVIOLET EXPLORER AND OPTICAL OBSERVATIONS OF AD LEONIS: EVIDENCE FOR LARGE CORONAL LOOPS AND THE NEUPERT EFFECT IN STELLAR FLARES, *ApJ*, **453**, 464

Hawley, S. L. & Pettersen, B. R. 1991. THE GREAT FLARE OF 1985 APRIL 12 ON AD LEONIS, *ApJ*, **378**, 725

Heise, J., Brinkman, A. C., Schrijver, J., et al. 1975, EVIDENCE FOR X-RAY EMISSION FROM FLARE STARS OBSERVED BY ANS, *ApJ*, **202**, L73

Hudson, H. S., Acton, L. W., Hirayama, T., & Uchida, Y. 1992, WHITE-LIGHT FLARES OBSERVED BY YOHKOH, *PASJ*, **44**, L77

Isobe, T., Feigelson, E. D., Akritas, M. G., & Babu, G. J. 1990, LINEAR REGRESSION IN ASTRONOMY. I., *ApJ*, **364**, 104

Jansen, F., Lumb, D., Altieri, B., et al. 2001, XMM-NEWTON OBSERVATORY: I. THE SPACECRAFT AND OPERATIONS, *A&A*, **365**, L1

Jenkins, L. F. 1952, GENERAL CATALOGUE OF TRIGONOMETRIC STELLAR PARALLAXES

Johns-Krull, C. M. & Valenti, J. A. 1996, DETECTION OF STRONG MAGNETIC FIELDS ON M DWARFS, *ApJ*, **459**

Joy, A. H. & Humason, M. L. 1949, OBSERVATIONS OF THE FAINT DWARF STAR L 726-8, *PASP*, **61**, 133

Kaastra, J. S., Mewe, R., & Nieuwenhuijzen, H. 1996, in Frontiers science series, Vol. 15, UV and X-ray Spectroscopy of Astrophysical and Laboratory Plasmas: Proceedings of the Eleventh Colloquium on UV and X-ray ... held on May 29–June 2, 1995, Nagoya, Japan, ed. K. Yamashita & T. Watanabe (Universal Academy Press), 411

Kahler, S. W. 1982, THE ROLE OF THE BIG FLARE SYNDROME IN CORRELATIONS OF SOLAR ENERGETIC PORTON FLUXES AND ASSOCIATED MICROWAVE BURST PARAMETERS, *JGR*, **87**, 3439

Kahn, S. M., Behar, E., Kinkhabwala, A., & Savin, D. W. 2002, X-RAY SPECTROSCOPY OF ASTROPHYSICAL PLASMAS, *Phil. Trans. R. Soc. Lond. A*, **360**, 1923

Kalas, P., Liu, M. C., & Matthews, B. C. 2004, DISCOVERY OF A LARGE DUST DISK AROUND THE NEARBY STAR AU MICROSCOPII, *Science*, **303**, 1990

Kosovichev, A. G. & Zharkova, V. V. 1998, X-RAY FLARE SPARKS QUAKE INSIDE THE SUN, *Nature*, **393**, 317

Kosugi, T., Dennis, B. R., & Kai, K. 1988, ENERGETIC ELECTRONS IN IMPULSIVE AND EXTENDED SOLAR FLARES AS DEDUCTED FORM FLUX CORRELATIONS BETWEEN HARD X-RAYS AND MICROWAVES, *ApJ*, **324**, 1118

Krucker, S. & Benz, A. O. 1998, ENERGY DISTRIBUTION OF HEATING PROCESSES IN THE QUIET SOLAR CORONA, *ApJ*, **501**, L213

Lacy, C. H. 1977, RADII OF NEARBY STARS: AN APPLICATION OF THE BARNS-EVANS RELATION, *ApJS*, **34**, 479

Landi, E., Zanna, G. D., Young, P. R., et al. 2006, CHIANTI - AN ATOMIC DATABASE FOR EMISSION LINES. VII. NEW DATA FOR X-RAYS AND OTHER IMPROVEMENTS, *ApJS*, **162**, 261

Ledrew, G. 2001, THE REAL STARRY SKY, *JRASC*, **95**, 32

Leggett, S. K., Allard, F., Berriman, G., Dahn, C. C., & Hauschildt, P. H. 1996, INFRARED SPECTRA OF LOW-MASS STARS: TOWARD A TEMPERATURE SCALE FOR RED DWARFS, *ApJS*, **104**, 117

Liedahl, D. A. 1999, THE X-RAY SPECTRAL PROPERTIES OF PHOTOIONIZED PLASMAS AND TRANSIENT PLASMAS, **520**, 189

Lim, J., Nelson, G. J., & Vaughan, A. E. 1987, A MULTI-PURPOSE, MULTI-CHANNEL RADIOSPECTROGRAPH FOR THE PARKES TELESCOPE, *Proc. ASA*, **7**, 2

Linsky, J. L., Bornmann, P. L., Carpenter, K. G., et al. 1982, OUTER ATMOSPHERES OF COOL STARS. XII. A SURVEY OF IUE ULTRAVIOLET EMISSION LINE SPECTRA OF COOL DWARF STARS, *ApJ*, **260**, 670

Lippincott, S. L. 1952, SEARCH FOR FLARES OF DM STARS ON THE SPROUL ASTROMETRIC PROGRAM, *ApJ*, **115**, 582

Magee, H. R. M., Güdel, M., Audard, M., & Mewe, R. 2003, AN XMM-NEWTON OBSERVATION OF THE FLARE STAR AU MIC, *Adv. Space Res.*, **32**, 1149

Maggio, A. & Ness, J.-U. 2005, SPECTRAL INDICATIONS OF DENSITY VARIABILITY IN THE CORONA OF AD LEONIS, *ApJ*, **622**, L57

Mariska, J. T. 2005, OBSERVATIONS OF SOLAR FLARE DOPPLER SHIFT OSCILLATIONS WITH THE BRAGG CRISTAL SPECTROMETER ON *yohkoh*, *ApJL*, **620**, 67

Masciadri, E., Mundt, R., Henning, T., Alvarez, C., & y Navascués, D. B. 2005, A SEARCH FOR HOT MASSIVE EXTRASOLAR PLANETS AROUND NEARBY YOUNG STARS WITH THE ADAPTIVE OPTICS SYSTEM NACO, *ApJ*, **625**, 1004

Mason, K. O., Breeveld, A., Much, R., et al. 2001, THE XMM-NEWTON OPTICAL/UV MONITOR TELESCOPE, *A&A*, **365**, L36

Mathioudakis, M. & Doyle, J. G. 1989, FLUX-FLUX RELATION: MG II H AND K VERSUS X-RAYS IN DWARF M AND K STARS, *A&A*, **224**, 179

Mathioudakis, M., Fruscione, A., Drake, J. J., et al. 1995, ACTIVITY VERSUS ROTATION IN THE EXTREME ULTRAVIOLET, *A&A*, **300**, 775

Mathioudakis, M., Seiradakis, J. H., Williams, D. R., et al. 2003, WHITE-LIGHT OSCILLATIONS DURING A FLARE ON II PEG:, *A&A*, **403**, 1101

Matranga, M., Mathioudakis, M., Kay, H. R. M., & Keenan, F. P. 2005, FLARE X-RAY OBSERVATIONS OF AB DORADUS: EVIDENCE OF STELLAR CORONAL OPACITY, *ApJ*, **261**

Matthews, S. A., van Driel-Gesztelyi, L., Hudson, H. S., & Nitta, N. V. 2003, A CATALOGUE OF WHITE-LIGHT FLARES OBSERVED BY YOKHOH, *A&A*, **409**, 1107

McKenzie, D. E. & Mullan, D. J. 1997, PERIODIC MODULATION OF X-RAY INTENSITY FROM CORONAL LOOPS - HEATING BY RESONANT ABSORPTION?, *Solar Phys.*, **176**, 127

Mewe, R., Gronenschild, E. H. B. M., & van den Oord, G. H. J. 1985, CALCULATED X-RADIATION FROM OPTICALLY THIN PLASMAS. V, *A&AS*, **62**, 197

Mitra-Kraev, U. & Benz, A. O. 2001, A NANOFLARE HEATING MODEL FOR THE QUIET SOLAR CORONA, *A&A*, **373**, 318

Mitra-Kraev, U., Harra, L. K., Güdel, M., et al. 2005a, RELATIONSHIP BETWEEN X-RAY AND ULTRAVIOLET EMISSION OF FLARES FROM dME STARS OBSERVED BY XMM-NEWTON, *A&A*, **431**, 679

Mitra-Kraev, U., Harra, L. K., Williams, D. R., & Kraev, E. 2005b, THE FIRST OBSERVED STELLAR X-RAY FLARE OSCILLATION: CONSTRAINTS ON THE FLARE LOOP LENGTH AND THE MAGNETIC FIELD, *A&A*, **436**, 1041

Mullan, D. J. & Fleming, T. A. 1996, CORONAL HEATING IN dME AND dM STARS: CLUES FROM THE X-RAY SURFACE FLUXES, *ApJ*, **464**, 890

Mullan, D. J., Herr, R. B., & Bhattacharyya, S. 1992, TRANSIENT PERIODICITIES IN X-RAY-ACTIVE RED DWARFS: FIRST RESULTS FROM MOUNT CUBA AND INTERPRETATION WITH AN OSCILLATING LOOP MODEL, *ApJ*, **391**, 265

Mullan, D. J. & Johnson, M. 1995, CORONAL HEATING IN FLARE STARS: RESONANT MHD ABSORPTION?, *ApJ*, **444**, 350

Nakariakov, V. M., Foullon, C., Verwichte, E., & Young, N. P. 2006, QUASI-PERIODIC MODULATION OF SOLAR AND STELLAR FLARING EMISSION BY MAGNETOHYDRODYNAMIC OSCILLATIONS IN A NEARBY LOOP, *A&A*, **452**, 343

Nakariakov, V. M., Melnikov, V. F., & Reznikova, V. E. 2003, GLOBAL SAUSAGE MODES OF CORONAL LOOPS, *A&A*, **412**

Nakariakov, V. M. & Ofman, L. 2001, DETERMINATION OF THE CORONAL MAGNETIC FIELD BY CORONAL LOOP OSCILLATIONS, *A&A*, **372**, L53

Nakariakov, V. M., Tsiklauri, D., Kelly, A., Arber, T. D., & Aschwanden, M. J. 2004, ACOUSTIC OSCILLATIONS IN SOLAR AND STELLAR FLARING LOOPS, *A&A*, **414**, L25

Ness, J.-U., Mewe, R., Schmitt, J. H. M. M., et al. 2001, HELIUM-LIKE TRIPLET

DENSITY DIAGNOSTICS. APPLICATIONS TO CHANDRA-LETGS X-RAY OBSERVATIONS OF CAPELLA AND PROCYON, *A&A*, **367**, 282

Ness, J.-U., Schmitt, J. H. M. M., Audard, M., Güdel, M., & Mewe, R. 2003, ARE STELLAR CORONAE OPTICALLY THIN IN X-RAYS?, *A&A*, **407**, 347

Ness, J.-U., Schmitt, J. H. M. M., Burwitz, V., et al. 2002, CORONAL DENSITY DIAGNOSTICS WITH HELIUM-LIKE TRIPLETS: CHANDRA-LETGS OBSERVATIONS OF ALGOL, CAPELLA, PROCYON, EPSILON ERI, ALPHA CEN A&B, UX ARI, AD LEO, YY GEM, AND HR 1099, *A&A*, **394**, 911

Neupert, W. M. 1968, COMPARISON OF SOLAR X-RAY LINE EMISSION WITH MICROWAVE EMISSION DURING FLARES, *ApJ*, **153**, L59

Noyes, R. W., Hartmann, L. W., Baliunas, S. L., Duncan, D. K., & Vaughan, A. H. 1984, ROTATION, CONVECTION, AND MAGNETIC ACTIVITY IN LOWER MAIN-SEQUENCE STARS, *ApJ*, **279**, 763

Ofman, L. & Wang, T. 2002, HOT CORONAL LOOP OSCILLATIONS OBSERVED BY SUMER: SLOW MAGNETOSONIC WAVE DAMPING BY THERMAL CONDUCTION, *ApJ*, **580**, L85

Osten, R. A., Hawley, S. L., Allred, J. C., Johns-Krull, C. M., & Roark, C. 2005, FROM RADIO TO X-RAY: FLARES ON THE DME FLARE STAR EV LACERTAE, *ApJ*, **621**, 398

Pallavicini, R., Tagliaferri, G., & Stella, L. 1990, X-RAY EMISSION FROM SOLAR NEIGHBOURHOOD FLARE STARS - A COMPREHENSIVE SURVEY OF EXOSAT RESULTS, *A&A*, **228**, 403

Parker, E. N. 1975, THE GENERATION OF MAGNETIC FIELDS IN ASTROPHYSICAL BODIES. X - MAGNETIC BUOYANCY AND THE SOLAR DYNAMO, *ApJ*, **198**, 205

Parnell, C. E. & Jupp, P. E. 2000, STATISTICAL ANALYSIS OF THE ENERGY DISTRIBUTION OF NANOFLARES IN THE QUIET SUN, *ApJ*, **529**, 554

Perryman, M. A. C., Lindegren, L., Kovalevsky, J., et al. 1997, THE HIPPARCOS CATALOGUE, *A&A*, **323**, L49

Pettersen, B. R. 1980, PHYSICAL PARAMETERS OF SOLAR NEIGHBOURHOOD FLARE STARS, *A&A*, **82**, 53

Pettersen, B. R. 1989, A REVIEW OF STELLAR FLARES AND THEIR CHARACTERISTICS, *Solar Phys.*, **121**, 299

Pettersen, B. R., Kern, G. A., & Evans, D. S. 1983, STARSPOTS AND STELLAR FLARES ON EV LAC AND YZ CMI, *A&A*, **123**, 184

Porquet, D., Mewe, R., Dubau, J., Raassen, A. J. J., & Kaastra, J. S. 2001, LINE RATIOS FOR HELIUM-LIKE IONS: APPLICATIONS TO COLLISION-DOMINATED PLASMAS, *A&A*, **376**, 1113

Pradhan, A. K. 1985, RECOMBINATIN-CASCADE X-RAY SPECTRA OF HIGHLY CHARGED HELIUM-LIKE IONS, *ApJ*, **288**, 824

Raassen, A. J. J., Mewe, R., Audard, M., & Güdel, M. 2003, THE X-RAY SPECTRA OF THE FLAREING AND QUIESCENT STATES OF AT MICROSCOPII OBSERVED BY XMM-NEWTON, *A&A*, **411**, 509

Roberts, B. 2000, WAVES AND OSCILLATIONS IN THE CORONA, *Sol. Phys.*, **193**, 139

Roberts, B., Edwin, P. M., & Benz, A. O. 1984, ON CORONAL OSCILLATIONS, *ApJ*, **279**, 857

Rodonò, M. 1974, SHORT-LIVED FLARE ACTIVITY OF THE HYADES FLARE STAR H II 2411, *A&A*, **32**, 337

Schrijver, C. J., Dobson, A. K., & Radick, R. R. 1992, NEARLY SIMULTANEOUS OBSERVATIONS OF CHROMOSPHERIC AND CORONAL RADIATIVE LOSSES OF COOL STARS, *A&A*, **258**, 432

Ségransan, D., Kervella, P., Forveille, T., & Queloz, D. 2003, FIRST RADIUS MEASUREMENTS OF VERY LOW MASS STARS WITH THE VLTI, *A&A*, **397**, L5

Shibata, K. & Yokoyama, T. 2002, A HERTZSPRUNG-RUSSELL-LIKE DIAGRAM FOR SOLAR/STELLAR FLARES AND CORONA: EMISSION MEASURE VERSUS TEMPERATURE DIAGRAM, *ApJ*, **577**, 422

Smith, K., Güdel, M., & Audard, M. 2005, FLARES OBSERVED WITH XMM-NEWTON AND THE VLA, *A&A*, **436**, 241

Stelzer, B., Schmitt, J. H. M. M., Micela, G., & Liefke, C. 2006, SIMULTANEOUS OPTICAL AND X-RAY OBSERVATIONS OF A GIANT FLARE ON THE ULTRACOOL DWARF LP 412-31, *A&A*, **460**, L35

Stepanov, A. V., Urpo, S., & Zaĭtsev, V. 1992, DIAGNOSTICS OF SOLAR FLARE AND EVAPORATED PLASMA USING MM-WAVE EMISSION, *Sol. Phys.*, **140**, 139

Strüder, L., Briel, U., Dennerl, K., et al. 2001, THE EUROPEAN PHOTON IMAGING CAMERA ON XMM-NEWTON: THE PN-CCD CAMERA, *A&A*, **365**, L18

Terekhov, O. V., Shevchenko, A. V., Kuz'min, A. G., et al. 2002, OBSERVATION OF QUASI-PERIODIC PULSATIONS IN THE SOLAR FLARE SF 900610, *Astron. Lett.*, **28**. 397

Testa, P., Drake, J. J., & Peres, G. 2004a, THE DENSITY OF CORONAL PLASMA IN ACTIVE STELLAR CORONAE, *ApJ*, **617**, 508

Testa, P., Drake, J. J., Peres, G., & DeLuca, E. E. 2004b, DETECTION OF X-RAY RESONANCE SCATTERING IN ACTIVE STELLAR CORONAE, *ApJ*, **609**, 79

Thackeray, A. D. 1950, FIVE SOUTHERN STARS WITH EMISSION-LINE SPECTRA, *MNRAS*, **110**, 45

Torrence, C. & Compo, G. P. 1998, A PRACTICAL GUIDE TO WAVELET ANALYSIS, *Bull. Amer. Meteor. Soc.*, **79**, 61

Turner, M. J. L., Abbey, A., Arnaud, M., et al. 2001, THE EUROPEAN PHOTON IMAGING CAMERA ON XMM-NEWTON: THE MOS CAMERAS, *A&A*, **365**, L27

van den Besselaar, E. J. M., Raassen, A. J. J., Mewe, R., et al. 2003, AD LEONIS: FLARES OBSERVED BY XMM-NEWTON AND CHANDRA, *A&A*, **411**, 587

van Maanen, A. 1940, THE PHOTOGRAPHIC DETERMINATION OF STELLAR PARALLAXES WITH THE 60- AND 100-INCH REFLECTORS. SEVENTEENTH SERIES., *ApJ*, **91**, 503

Verwichte, E., Nakariakov, V. M., Ofman, L., & DeLuca, E. E. 2004, CHARACTERISTICS OF TRANSVERSE OSCILLATIONS IN A CORONAL LOOP ARCADE, *Sol. Phys.*, **223**, 77

Vilhu, O. 1984, THE NATURE OF MAGNETIC ACTIVITY IN LOWER MAIN SEQUENCE STARS, *A&A*, **133**, 117

Švestka, Z. 1989, SOLAR FLARES - THE GRADUAL PHASE, *Sol. Phys.*, **121**, 399

Švestka, Z. 1994, SLOW-MODE OSCILLATIONS OF LARGE-SCALE CORONAL LOOPS, *Sol. Phys.*, **152**, 505

Wood, B. E., Mller, H.-R., Zank, G. P., Linsky, J. L., & Redfield, S. 2005, NEW MASS-LOSS MEASUREMENTS FROM ASTROSPHERIC LYα ABSORPTION, *ApJ*, **628**, L143

Wood, B. E., Müller, H.-R., Zank, G. P., Gary, P., & Linsky, J. L. 2002, MEASURED MASS-LOSS RATES OF SOLAR-LIKE STARS AS A FUNCTION OF AGE AND ACTIVITY, *ApJ*, **574**, 412

Zaĭtsev, V. V. & Stepanov, A. V. 1989, ELEMENTARY FLARE BURSTS AND PROPERTIES OF ERUPTIVE SOLAR PLASMA, *Sov. Astron. Lett.*, **15**, 66

Zhilyaev, B. E., Romanyuk, Y. O., Verlyuk, I. A., et al. 2000, DETECTION OF HIGH-FREQUENCY OPTICAL OSCILLATIONS ON THE FLARE STAR EV LACERTAE, *A&A*, **364**, 641